

A NUMERICAL STUDY OF STEADY-STATE VORTEX CONFIGURATIONS
AND VORTEX PINNING IN TYPE-II SUPERCONDUCTORS

A Dissertation
by
SANGBUM KIM

Submitted to the Office of Graduate Studies of
Texas A&M University
in partial fulfillment of the requirements for the degree of
DOCTOR OF PHILOSOPHY

December 2004

Major Subject: Materials Science and Engineering

A NUMERICAL STUDY OF STEADY-STATE VORTEX CONFIGURATIONS
AND VORTEX PINNING IN TYPE-II SUPERCONDUCTORS

A Dissertation

by

SANGBUM KIM

Submitted to Texas A&M University
in partial fulfillment of the requirements
for the degree of

DOCTOR OF PHILOSOPHY

Approved as to style and content by:

Malcolm J. Andrews
(Co-Chair of Committee)

Chia-Ren Hu
(Co-Chair of Committee)

Ali Beskok
(Member)

John C. Slattery
(Member)

Dennis L. O'Neal
(Head of Department)

December 2004

Major Subject: Materials Science and Engineering

ABSTRACT

A Numerical Study of Steady-State Vortex Configurations

and Vortex Pinning in Type-II Superconductors. (December 2004)

Sangbum Kim, B.S., M.S., Pohang University of Science and Technology

Co-Chairs of Advisory Committee: Dr. Malcolm J. Andrews
Dr. Chia-Ren Hu

In part I, a numerical study of the mixed states in a mesoscopic type-II superconducting cylinder is described. Steady-state configurations and transient behavior of the magnetic vortices for various values of the applied magnetic field H are presented. Transitions between different multi-vortex states as H is changed is demonstrated by abrupt changes in vortex configurations and jumps in the B vs H plot. An efficient scheme to determine the equilibrium vortex configuration in a mesoscopic system at any given applied field, not limited to the symmetry of the system, is devised and demonstrated.

In part II, a superconducting thin film is subject to a non-uniform magnetic field from a vertical magnetic dipole, consisting of two magnetic monopoles of opposite charges. For a film with constant thickness and with no pins, it has been found that the film carries two pairs of vortex-antivortex in the steady state in the imposed flux range of $2.15 < \Phi^+ < 2.90$ (in units of flux quantum) and no vortex at all for $\Phi^+ \leq 2.15$. Transitions from a superconducting state with 3 pairs of vortex-antivortex to one with 2 pairs, where a pair of vortex-antivortex annihilates, have been observed in the pseudo-time sequence. With a perturbation with antidots (holes), vortex-antivortex pair has been created for lower magnetic fluxes down to $\Phi^+ = 1.3$.

In the sample of size $16\xi \times 16\xi$, the attraction force between the vortex and antivortex always dominates over the pinning force, so that they eventually come out

of pins, move toward each other, and annihilate each other. The annihilation rate, measured with time taken for the annihilation, is reduced noticeably by the increase of the distance between pins, or the increase in the pin size. A simulation of the magnetic vortex pinning in the sample of size $32\xi \times 32\xi$ suggests we are likely to achieve pinning of the vortex-antivortex pair with the sample size around this and vortex-antivortex separation of 22ξ . Using this sample as a template, the maximum density of pinned vortices achievable is calculated to be about 7.6×10^{14} vortices/ m^2 for $\xi \cong 1.6\text{\AA}$.

To my late Father, who loved books and God

ACKNOWLEDGMENTS

This dissertation concludes my long journey in Science and Engineering. Along the way I am indebted to so many people in many ways. Here I can list only the most outstanding of them.

The first place is always reserved for Dr. In Seok Kang in the Department of Chemical Engineering at Pohang University of Science and Technology in Korea. Without his inspiration and encouragement I would not have come to the U.S., nor would I have started Ph.D. study. Not only is he a brilliant mathematician but he is also the best teacher I have ever known. The mathematical skills I polished under him have been very helpful for my graduate study.

I appreciate my advisor Dr. Malcolm J. Andrews in the Department of Mechanical Engineering at Texas A&M University for all his help, motivation, financial support, encouragement, and leadership. His strong encouragement was the major force to drive my research forward and it let me graduate on time. Through working with him, I have learned that research is more than just studying books. In fact, research is a comprehensive art ranging from selecting topics and audiences to managing time and resources. Despite a busy schedule, Dr. Andrews has always made time to accommodate his students.

I owe my gratitude to Dr. Chia-Ren Hu in the Department of Physics at Texas A&M University, who is also the co-Chair of my committee. His wealth of knowledge and insight into physics helped me make this research meet the basic requirement. My discussion with him in almost unlimited time in various topics of physics is certainly a privilege that not all students are granted. I thank Dr. Joseph Ross in the Department of Physics, who is also the head of the Materials Science and Engineering for attending my defense and granting me the doctoral degree in Materials Science

and Engineering.

I wish to thank my committee members, Dr. Ali Beskok in the Department of Mechanical Engineering and Dr. John Slattery in the Departments of Aerospace Engineering, Chemical Engineering, and Mathematics for their patience and time in going over the work and helping me in crucial junctures. I am grateful to Dr. Nagamangala Anand, who has helped me greatly in my hard times in my early years at TAMU. I appreciate the staff of the Texas A&M supercomputing facility for their help, particularly in optimizing my code.

I thank Arindam Banerjee, Nicholas Mueschke, Wayne Kraft, Gopinath Subramanian, Nader Berchane for being good friends. Particulary I appreciate their proofreading of my dissertation carefully and patiently. I list the names of the people who I owe my gratitude: Dr. Kyoungjin Kim, Dr. Dongsik Kim, Dr. Michael Crawford and Dr. Marc Compere. Last, but not the least, I wish to thank my family and God for giving all the good things which I certainly do not deserve.

TABLE OF CONTENTS

CHAPTER		Page
I	INTRODUCTION	1
II	CHARACTERISTICS OF SUPERCONDUCTING PHENOM- ENA	6
	II.1. Two hallmarks of superconductivity	6
	II.2. London's model for the electrodynamics of super- conductivity	9
	II.3. Two types of superconductors	10
III	MICROSCOPIC THEORY	14
	III.1. Quasi-particles in quantum liquids	15
	III.2. Superfluidity	16
	III.2.1. Wave function of the Bose superfluid	17
	III.3. Superfluidity of a Fermi gas	20
	III.3.1. Wave function of the superfluid Fermi gas	23
IV	GINZBURG-LANDAU THEORY	26
	IV.1. Second-order phase transitions and critical phenomena	26
	IV.2. Landau's theory of second-order phase transition	28
	IV.3. The Ginzburg-Landau equations	30
	IV.3.1. Flux quantization	34
	IV.3.2. Gauge symmetry	35
	IV.4. Time-dependent Ginzburg-Landau equations (TDGL)	37

CHAPTER		Page
V	INTRODUCTION TO PART I: STEADY-STATE AND EQUILIBRIUM VORTEX CONFIGURATIONS, TRANSITIONS, AND EVOLUTION IN A MESOSCOPIC SUPERCONDUCTING CYLINDER	40
	V.1. Abrikosov vortex theory	43
VI	THE SIMPLIFIED TIME-DEPENDENT GINZBURG-LANDAU EQUATION	45
	VI.1. Discretization and calculation procedure	48
	VI.2. Stability of the numerical scheme	52
	VI.2.1. Matrix method	53
	VI.2.2. Von Neumann's method	56
VII	MAGNETIC PENETRATION UNDER SYMMETRY	60
	VII.1. Steady States under zero-field cooling in a perfectly square sample at low temperatures	60
	VII.2. Pseudo-time sequence showing vortex entry dynamics	68
VIII	EQUILIBRIUM STATE	70
	VIII.1. Steady states with reduced symmetry and the equilibrium state	70
	VIII.2. Grid independence	79
IX	INTRODUCTION TO PART II: OPTIMAL PINNING CONFIGURATION TO TRAP A VORTEX-ANTIVORTEX PAIR IN A SUPERCONDUCTING FILM UNDER THE NON-UNIFORM MAGNETIC FIELD OF A MAGNETIC DIPOLE	81
	IX.1. Pearl vortex theory	85
	IX.2. Antidots in a bulk superconductor	88
X	GINZBURG-LANDAU EQUATION FOR THIN FILM	92

CHAPTER	Page
X.1.	Induced magnetic field by supercurrents 94
X.2.	Magnetic dipole field 96
XI	SOLUTION METHOD 100
XI.1.	Discretization of Ginzburg-Landau equation 100
XI.2.	Discretized solutions for magnetic potential \mathbf{A} 101
XI.3.	Two-dimensional fast Fourier transform in parallel computers 101
XII	SIMULATION RESULTS 104
XII.1.	Magnetic penetration in a film of constant thickness . 104
XII.2.	Magnetic penetration in a film with pins 109
XII.2.1.	The effect of artificial vortex method 114
XII.3.	Magnetic relaxation in a film with pins 117
XIII	CONCLUSIONS 128
XIII.1.	Summary and conclusion to Part I 128
XIII.2.	Conclusion to Part II 130
REFERENCES 132
APPENDIX A 139
APPENDIX B 142
APPENDIX C 144
VITA 146

TABLE	LIST OF TABLES	Page
I	The resultant number of vortices n_∞ and the induced magnetic field B for the applied magnetic field H	66
II	The steady-state total Gibbs free energy \bar{G} and % error in \bar{G} for changing grid size for artificial vortex initial condition ($H = 0.84$) and uniformly superconducting initial condition ($H = 1.733$).	80

FIGURE	LIST OF FIGURES	Page
1	The expected behavior if a superconductor is a perfect conductor. (a) The specimen in the normal state is brought into a magnetic field and then cooled below its critical temperature. The penetrated magnetic field in the specimen does not change. (b) The specimen in the normal state is first cooled below its critical temperature and then brought into a magnetic field. The magnetic field does not penetrate the specimen.	8
2	Meissner effect of a superconductor: The specimen in the normal state is brought into a magnetic field and then cooled below its critical temperature. The penetrated magnetic field is pushed out. . .	9
3	Phase diagram of superconductors	11
4	Ginzburg-Landau free energy function for $\alpha > 0$ ($T > T_c$) and for $\alpha < 0$ ($T < T_c$). Heavy dots indicate equilibrium positions.	37
5	The staggered grid arrangement for cell nodes P,E,W,N,S and faces e,w,n,s.	49
6	Plots of $ \Psi ^2$ and $h = \nabla \times \mathbf{A}$ for various applied field H [$ \Psi ^2$ is shown on the left in (a) to (k), and h on the right in (a) to (k)]. These final steady-state solutions are obtained by a relaxation method from a uniform superconducting state.	61
7	The effect of an applied magnetic field H on the induced average magnetic field B	67
8	Pseudo-time sequence of vortex dynamics showing vortex-entry for $H = 1.145$. Note that the initial state is the uniform superconducting state.	69

FIGURE	Page
9	The initial, random vortex configurations, and the corresponding steady-state vortex configurations they evolve to [The initial vortex configurations is shown on the left in (a) to (o), and the steady-state vortex configurations on the right in (a) to (o)]. Most of these final steady-state solutions are metastable states with a given number of trapped vortices in a field-cooled situation. The one with the lowest Gibbs energy among them may be identified as the true equilibrium state at the chosen field value, see Fig.10. 73
10	The steady-state total Gibbs free energy per unit area \bar{G} and the corresponding final number of vortices, n_∞ 78
11	Examples of the steady-state vortex configurations for larger grid size (64×64). (a) artificial vortex initial condition under $H = 0.84$, and (b) uniformly superconducting initial condition under $H = 1.733$ 80
12	A superconducting film under a magnetic dipole. Stray field lines penetrating the film creates vortex-antivortex pair(s). They may be pinned at pinning centers such as holes (antidots) made in the film in a proper configuration, shown here in the distance ε apart. 82
13	A superconducting film under a magnetic dipole. Stray field lines penetrating the film creates vortex-antivortex pair(s). Since $d_{film} = 0.1\xi$, the film is virtually transparent to magnetic penetration in the thickness direction, and “soaked” in the applied magnetic field. In the superconducting film, the induced magnetic fields by the supercurrents incur only negligible change in the applied magnetic field. 82
14	Superconducting film carrying a pair of vortex-antivortex. There is an attractive interaction force between the vortex and antivortex. The effective penetration depth λ_{eff} increases as the film thickness d decreases. Hence for a thin film ($d \ll 1$) the interaction force between the vortex-antivortex pair has a much longer range than the penetration depth λ 87
15	Free energy of the system F in the direction of the coordinate ρ_0 90
16	A periodic sample spanned by the lattice vectors \mathbf{b}_1 and \mathbf{b}_2 93

FIGURE	Page
17	A periodic array of the systems. In each system, a magnetic dipole is located above the center of each block of the sample, which is in a periodic array by itself. 99
18	The magnetic penetration into a film with no pins in it, under the external field from a magnetic dipole. (a) The evolution of the superelectron density. (b) The corresponding evolution of phase of the order parameter. The film size is $L_x \times L_y = 16\xi \times 16\xi$, and thickness $d_f = 0.1\xi$. Here $\Phi^+ = 2.90$ and the film carries three vortex-antivortex pairs in the steady state. 105
19	The steady-states of magnetic penetration into the film with no pins under the external field from a magnetic dipole. Top row is the evolution of the superelectron density, bottom row the corresponding evolution of phase of the order parameter. The film is of the same size and thickness as in Fig. 18. Here $\Phi^+ = 2.15$ for (a) and (d), $\Phi^+ = 2.50$ for (b) and (e), and $\Phi^+ = 2.90$ for (c) and (f). It is found that in the interval $2.15 < \Phi^+ < 2.90$ the film carries two vortex-antivortex pairs in the steady state. 107
20	A magnetic penetration into the film with no pins under the external field from a magnetic dipole. (a) The evolution of the superelectron density. (b) The corresponding evolution of the phase of the order parameter. The film is of the same size and thickness as in Fig. 18. Here $\Phi^+ = 2.49$ is in the interval $2.15 < \Phi^+ < 2.90$ discussed in Fig. 19. three vortex-antivortex pairs initially appear in the film early ($t=3000$), then one pair annihilates itself ($t=6000$ and 7000). This process is more discernible in the phase plot. Finally the film carries two vortex-antivortex pairs in the steady state. 108

FIGURE	Page	
21	<p>The magnetic penetration into the film with two pins under the external field from a magnetic dipole. The dipole provides the magnetic flux $\Phi^+ = 1.90$. (a) The evolution of the superelectron density. (b) The corresponding evolution of the phase of the order parameter. The film is of the same size and thickness as in Fig. 18. The film center is at the node (32,32). There are two antidots of an approximate diameter 2ξ, centered at the nodes (29,29) and (45,45) respectively. In the steady state there is a pair of vortex-antivortex caught at the pins.</p>	111
22	<p>The magnetic penetration into the film with two larger pins under the external field from a magnetic dipole. (a) The evolution of the superelectron density. (b) The corresponding evolution of the phase of the order parameter. The two antidots have an approximate diameter 2.5ξ and the other parameters are the same as Fig. 21. In the steady state there is a pair of vortex-antivortex caught at the pins.</p>	112
23	<p>The steady-states of magnetic penetrations into the film with two pins, under the external field from a magnetic dipole. The film is of the same size and thickness as Fig.21. Here again $\Phi^+ = 1.90$. In (a) and (b) there are two antidots of an approximate diameter 2ξ, centered at the nodes (28,28) and (45,45). In the steady state the antivortex stays on the edge of the pin at (28,28) without being pulled further into the pin. In (c) and (d), where the antidots are at nodes (29,29) and (46,46), both vortices are pulled well into the pins. In (e) and (f), pins of bigger size (approximate diameter 2.5ξ) are located at (28,28) and (44,44). It is clear the antivortex is not fully pulled into the pin at (28,28).</p>	113
24	<p>A magnetic relaxation process <i>with the external magnetic field removed (turned off)</i> from an initial vortex state with a pair of vortex-antivortex inside the pins. The film thickness is $d_f = 0.1$. There are two antidots of an approximate diameter 2.5ξ, centered at nodes (29,29) and (45,45). The vortex and antivortex are found to come out of the pins and annihilate each other quickly.</p>	115

FIGURE	Page	
25	<p>Pseudo-time sequences of two cases of magnetic penetration into a film with thickness $d_f = 0.1$ with two antidots of an approximate diameter 2.5ξ, centered at nodes (29,29) and (44,44), and $\Phi^+ = 1.90$. (a) The magnetic penetration starting with the Meissner state results in a steady state with a pair of vortex-antivortex caught at the pins. (b) The magnetic penetration starts with a pair of artificial vortex and antivortex inside the pins instead of the Meissner state as in (a). The result is the same steady state with a pair of vortex-antivortex caught at the pins, which is achieved in a faster time.</p>	116
26	<p>Steady-states of a magnetic relaxation in a film with thickness $d_f = 0.1$. There are two antidots of an approximate diameter of 2ξ, centered at nodes (16,16) and (48,48) each. Here a pair of artificial vortex and antivortex attract each other under no external magnetic field. They eventually move out of the pins and annihilate each other.</p>	118
27	<p>The initial pin and vortex-antivortex arrangements of the simulation cases in which a pair of vortex and antivortex evolve with the external magnetic field removed. In the first case (shown in the upper left corner) the pins are located at $(i_{p_1}, j_{p_1}) = (16, 16)$ and $(i_{p_2}, j_{p_2}) = (48, 48)$. In the next case (to the right of the first sample), $(i_{p_1}, j_{p_1}) = (17, 17)$ and $(i_{p_2}, j_{p_2}) = (47, 47)$. In this way, the pins are put closer to each other by one node for the cases we consider one after another. In the last case, $(i_{p_1}, j_{p_1}) = (28, 28)$ and $(i_{p_2}, j_{p_2}) = (36, 36)$. At $t=0$, the artificial vortex-antivortex pair is located further outward by two nodes than the center of the pins. This is intended to prevent that any initial “overshoot” of the numerical simulation, instead of the actual attraction force, drives the vortices out of the pins.</p>	119
28	<p>Total time for the process where a pair of artificial vortex and antivortex attract, move out of the pins, and annihilate each other. It is a magnetic relaxation in a film with thickness $d_f = 0.1$ under no external dipole magnetic field. The abscissa is the distance in which the centers of the antidots of an approximate diameter of 2ξ are separated.</p>	120

FIGURE	Page
29	Defining the “escape time” of the vortex-antivortex pair for the $16\xi \times 16\xi$ sample. (a) and (b) are the density plots produced in a given time interval. (c) and (d) give the enlarged view of the lower left pin. At $t=1550$ the $ \Psi ^2 = 0.3$ contour lies inside the pin surface. At $t=1600$ there is a small triangular contour of $ \Psi ^2 = 0.3$ having just emerged outside the pin. Thus $ \Psi ^2 = 0.3$ contour “escaped” from the pin between $t=1550$ and 1600 . We set $t=1550$ the “escape time” 122
30	Pseudo-time measure for how long a vortex would take to escape from the pins as defined in Fig. 29. It is chosen as the time the density contour of level 0.3 emerges from the pin. This “time” can give a time scale for the vortex core to emerge from the pin. The states are obtained in magnetic relaxations in a film with thickness $d_f = 0.1$ under no external dipole magnetic field. The abscissa is the distance in which the centers of the antidots of an approximate diameter of 2ξ are separated. 123
31	Defining the “escape time” of the vortex-antivortex pair for the $32\xi \times 32\xi$ sample. (a) and (b) are the density plots produced in a given time interval. (c) and (d) give the enlarged view of the lower left pin. At $t=15900$ the $ \Psi ^2 = 0.3$ contour lies inside the pin surface. At $t=16000$ there is a small triangular contour of $ \Psi ^2 = 0.3$ having just emerged outside the pin. Thus $ \Psi ^2 = 0.3$ contour “escaped” from the pin between $t=15900$ and 16000 . We set $t=15900$ the “escape time” 124
32	(a) and (c) are the density plots produced in a given time interval. (b) and (d) give the enlarged view of the lower left pin. Comparing Figs. (b) and (d), the contour levels have no change between $t=25200$ and 42400 after passing the escape time $t=15900$. The pins are still holding the vortex-antivortex pair after a long time in the large sample. We conclude the pinning has been achieved. . . 126
33	A periodic sample spanned by the lattice vectors \mathbf{t}_1 and \mathbf{t}_2 139
34	Triangular-ish lattice of vortices in a square superconducting cylinder with periodic boundary conditions carrying 9 flux quanta. 141

FIGURE	Page
35 Vortex pinning and flux trapping in a film of variable thickness by a regular array of thin regions (pins). $H = 1$; $\kappa = 4$; film thickness = 1; pin thickness = 0.001; and pin neighbor thickness = 0.005.	143
36 Flow of vortices driven by the linearly varying magnetic field.	145

CHAPTER I

INTRODUCTION

Superconductivity is the superfluidity of electron liquid. At sufficiently low temperatures, lattice vibrations in the crystal induce interactions among the electrons such that the electrons “pair” (in momentum space) and form an electron liquid that no longer experiences friction when it flows. Such materials are known as “superconductors,” because they show no resistance to electrical current. Superconductivity and superfluidity are novel quantum phenomena. A branch of physics that studies of the collective behavior of a large number of atoms is called *Condensed-Matter Physics*. It gave birth to many wonders of modern technology such as transistor, integrated circuit, computer CPUs and memories, laser, and optical fibers, to name a few.

According to classical Physics, as temperature goes down the kinetic energies of all particles vanish, and the system of particles settles in the configuration of minimum potential energy. That is, it solidifies. Quantum mechanics says the most stable state of a system is not static equilibrium with the minimum potential energy, but rather a dynamic state with the lowest total (potential+kinetic) energy, where the particle motion is subject to the Heisenberg uncertainty principle. The dispersion Δq of the particle position q from its mean value \bar{q} , and the corresponding dispersion Δp of the momentum cannot vanish simultaneously: $\Delta q \Delta p \geq \hbar/2$.

At low enough temperatures the de Broglie wavelength $\lambda = 2\pi\hbar/p$, of the thermal motion of the atoms in a liquid, becomes comparable with interatomic distances. The resultant weak interaction between light particles can lead to coherent motion of the particles (small Δp) with little kinetic energy. In this case Δq can be large for small

This dissertation follows the style of the *Physical Review B*.

Δp by the uncertainty relation. This means a long-range order of the momentum vector. The particle momenta are locked to each other's. Clearly the long-range order is of a quantum mechanical origin. Therefore superconductivity and superfluidity are examples of *quantum mechanics in action in a macroscopic scale*. [1]

Superconductors have been a field of great interest since their discovery both for their theoretical importance, and for the important technological applications they have in superconducting magnets, sensors based on superconducting quantum interference devices (SQUIDs), and a wide variety of electromagnetic equipments (e.g. motors, power transmission cables, etc.). The discovery of High Temperature Superconductors (HTSC's) in 1980's [2] opened a floodgate of renewed interests and a variety of research areas worldwide. Their manufacturing, measurement, and control, provide researchers with a grand challenge. Since their properties are not yet completely understood, a quantitative modeling itself is not a trivial task.

In this study we consider the behaviors of type-II superconductors under external magnetic fields. We consider two kinds of samples, a square cylinder of mesoscopic size with free boundary conditions and a thin square film with periodic boundary conditions. The numerical simulations of vortex arrangements in the former, and vortex pinning in the latter are the main content of this dissertation.

In chapter II, we present the macroscopic characteristics of superconductors such as perfect conductivity and perfect diamagnetism. The peculiar electromagnetic behavior of superconductors is presented and a phenomenological model for the electrodynamics, called the London model is reviewed. Finally the difference between type-I and type-II superconductors are explained and illustrated in a phase diagram in $H - T$ coordinates.

Chapter III presents a microscopic theory that gives the precise definition of superconductivity, shows the existence of macroscopically large pool (condensate)

of superconducting electron pairs (Cooper pairs), and derives the *macroscopic* wave function of this condensate. A ground-breaking model for superconducting electron gas, called the BCS model is introduced. Yet no microscopic model can fully account for the motion of electron liquid in superconductors, since the strong interaction between particles in a liquid is hard to solve. Thus a phenomenological but powerful model will be briefly reviewed in chapter IV.

Chapter IV opens with introducing new concepts such as a second-order phase transition and critical phenomena, which in some sense can be regarded as looking at superconductivity from a different angle. While chapter II focused on the electromagnetic characteristics of superconductors, in chapter IV superconductivity is characterized in terms of internal symmetry of matter. (In short, superconductivity corresponds to a state of “broken symmetry” to be explained later.) Landau’s theory of second-order phase transition is introduced, and uses the condensate wave function derived in chapter III as an order parameter required by Landau theory, to derive the celebrated Ginzburg-Landau equations. A brief discussion on the time-dependent Ginzburg-Landau equations follows, concluding the chapter by outlining how to simplify the TDGL for computational simulation in the following chapters.

Chapter V is an introductory chapter to part I, “Steady-state and equilibrium vortex configurations, transitions, and evolution in a mesoscopic superconducting cylinder.” Here we consider a mesoscopic square cylinder with free boundary conditions. The magnetization process of this type-II superconductor subject to a magnetic field parallel to its axis, is simulated. Section V.1 presents the epoch-making theory of magnetic vortices by Abrikosov.

Chapter VI presents the derivation of the simplified TDGL and, discretization and calculation procedure. The stability and convergence issues are discussed.

Chapter VII presents the magnetic penetration under the symmetry conditions.

A magnetization curve and a table are provided. A time sequence of pictures giving qualitative information on the continuous transition to arrive at a steady state is presented.

Chapter VIII presents a systematic study to find an equilibrium state, by breaking the geometric symmetry binding the system at the metastable states. Final equilibrium state is determined by plotting and comparing the Gibbs free energies of the steady states of different vortex number and configurations. This part has been published in Physical Review B. [3]

Simulations under different conditions, under a field gradient and a periodic boundary condition, were presented in Appendices A, B, and C.

Chapters IX to XIII corresponds to Part II, “Optimal Pinning Configuration to Trap a Vortex-Antivortex Pair in a Superconducting Film Under the Non-Uniform Magnetic Field of a Magnetic Dipole.” A quest for pinning of a vortex-antivortex pair created in a thin film, is presented.

Chapter IX gives a description of the system and the survey of literature. In turn, it presents the theory of vortices in thin films by J. Pearl and a mathematical model for vortex pinning by a cavity in a bulk superconductor by Mkrtchyan and Shmidt.

Chapters X presents the mathematical model of the problem. Ginzburg-Landau equations are nondimensionalized with different scales from the those in Part I. The mathematical model for the dipole field is presented. The supercurrent is modeled as a current sheet at the film plane, and then the vector potential is solved analytically by Green’s function method.

Chapters XI presents the solution method. All the equations from chapter X are discretized on the staggered grid, and discrete relaxation equation for the order parameter is derived. Finally two-dimensional fast Fourier transform technique in

parallel computers is employed to update the vector potential at each iteration step.

Chapter XII presents the simulations for magnetic penetration process into the film, with and without pins. The number of vortex-antivortex pairs created in the film is constant in a range of the imposed magnetic flux by the magnetic dipole. Introduction of the pins into the film creates vortex-antivortex pair at lower values of the imposed magnetic flux. Next, the method of artificial vortex-antivortex pair is employed for the magnetic relaxation process, and the results of the numerical experiments using the method are presented. From the obtained pinning configuration, the density of pinned vortices achieved is estimated to be about $4.7 \text{ GB}/\text{cm}^2$.

Chapter XIII carries the conclusions to Part I and II.

CHAPTER II

CHARACTERISTICS OF SUPERCONDUCTING PHENOMENA

In this chapter we describe macroscopic characteristics of superconductivity, in particular, perfect conductivity and perfect diamagnetism. An earlier phenomenological model of superconductivity by F. London and H. London is introduced in this context. [4] The London model gives a good description of the electrodynamic behavior of superconductors, and is still widely used. The last section introduces type-II superconductors, which will be the focus of subsequent study.

II.1. Two hallmarks of superconductivity

The liquefaction of helium in 1908 by H. Kamerlingh Onnes paved the way to the discovery of superconductors. After this major accomplishment in low temperature physics, Onnes began using liquid helium as a cryogenic fluid to obtain low temperatures to study material properties below temperature $T = 4.2K$, which is the normal boiling point of liquid helium.

In 1911 it was found during the measurement of the electrical resistance of a rod of solid mercury that the voltage fell rapidly to zero below $T = 4.15K$. After observing that the voltage reappeared at higher temperature, Onnes concluded that the mercury entered a new state that has zero resistance to electrical current. [5] In other words, a superconductor is a perfect conductor.

Another fundamental macroscopic property of superconductors was discovered by Walter Meissner and Robert Ochsenfeld in 1933. [6] They observed that magnetic fields do not penetrate into a material in a superconducting state below a temperature (the critical temperature). Furthermore, if a superconductor placed in a magnetic field is cooled through the critical temperature, the magnetic field is expelled from

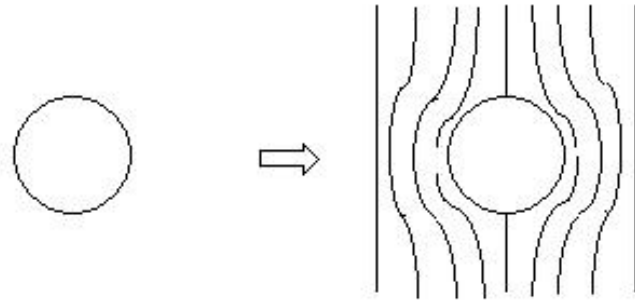
inside the material as it changes from the normal to the superconducting state. This expulsion of a magnetic field is now called the *Meissner effect*, and it demonstrates the second characteristic of a superconductor, *perfect diamagnetism*.

The Meissner effect cannot be explained in terms of perfect conductivity, which is illustrated in Fig. 1 and Fig. 2:

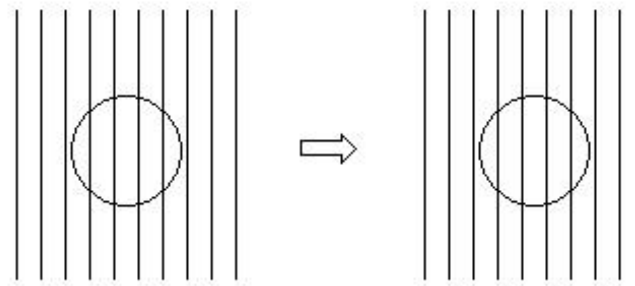
The perfect conductor model implies that electric field $\mathbf{E} = 0$ required for an infinite conductivity ($\sigma = \infty$) in order for a non-zero current density $\mathbf{j} = \sigma\mathbf{E}$. From the Maxwell equation $\text{curl } \mathbf{E} = \dot{B}/c$, a magnetic state cannot change in time ($\dot{B} = 0$) in a perfect conductor. Fig. 1 is the expected behavior of a superconductor if it were merely a perfect conductor when it is brought into a magnetic field.

Assume a material becomes a perfect conductor below a critical temperature. In Fig. 1 (a), a normal conductor is placed in a magnetic field B_0 , thus the magnetic field inside the specimen is $B = B_0$, too. As we cool the specimen, it enters a perfect conducting state and the magnetic field cannot change ($B = B_0$). In Fig. 1 (b), a normal conductor is cooled down without any external magnetic field ($B = 0$). After it enters a perfect conducting state, the magnetic state in the system must remain the same ($B = 0$). Thus an applied magnetic field cannot penetrate the specimen. This perfect conducting behavior is troublesome, since the final state is obviously path-dependent.

On the other hand, in Fig. 2 an initial magnetic field $B = B_0$ inside the specimen is pushed out of it as it is cooled below its critical temperature. Thus magnetic fields are expelled from the superconductor regardless of the path it takes to arrive at the superconducting state ($B = 0$). The Meissner effect proves that the superconducting state is a thermodynamic equilibrium state.



(a)



(b)

Fig. 1. The expected behavior if a superconductor is a perfect conductor. (a) The specimen in the normal state is brought into a magnetic field and then cooled below its critical temperature. The penetrated magnetic field in the specimen does not change. (b) The specimen in the normal state is first cooled below its critical temperature and then brought into a magnetic field. The magnetic field does not penetrate the specimen.

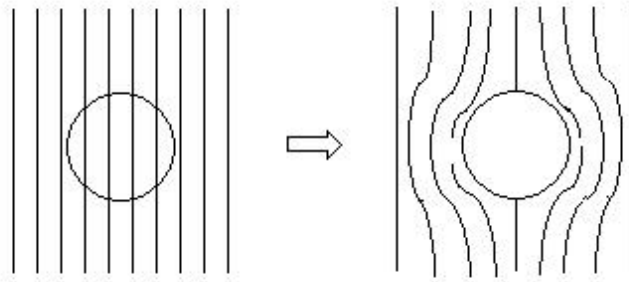


Fig. 2. Meissner effect of a superconductor: The specimen in the normal state is brought into a magnetic field and then cooled below its critical temperature. The penetrated magnetic field is pushed out.

II.2. London's model for the electrodynamics of superconductivity

The discovery of the Meissner effect has inspired H. London and F. London to develop a new model of the electrodynamics of superconductivity in 1934. The vanishing electric field inside a perfect conductor sustains a non-zero diamagnetic current $\mathbf{j} = \sigma \mathbf{E}$ (Fig. 1(b)) due to the infinitely large conductivity. The Meissner effect suggests that there should be an electric current sustained by the vanishing magnetic field inside a superconductor. Based on the argument that there seems to be no reason for assuming that the diamagnetic currents for Meissner effect should be different from the diamagnetic currents induced in the perfect conductor, the Londons suggested a model of supercurrents sustained by magnetic field. [1, 4]

$$\nabla \times (\Lambda \mathbf{j}_s) = -\frac{1}{c} \mathbf{H} \quad (2.1)$$

$$\frac{\partial}{\partial t} (\Lambda \mathbf{j}_s) = \mathbf{E} \quad (2.2)$$

where \mathbf{j}_s is the supercurrent density, \mathbf{E} is the electric field and \mathbf{H} is the magnetic field, c is the speed of light, t is time, σ is electric conductivity and $\Lambda \equiv \frac{4\pi\lambda^2}{c^2}$ is a phenomenological parameter of a superconductor. The equations (2.1) and (2.2) are known as the London equations.

The equation (2.1) together with the Maxwell equation $\text{curl } \mathbf{H} = \frac{4\pi}{c}\mathbf{j}$ can be combined to obtain

$$\nabla^2\mathbf{H} = \frac{1}{\lambda^2}\mathbf{H}. \quad (2.3)$$

In one-dimensional space, this becomes $d^2\mathbf{H}/dx^2 = \mathbf{H}/\lambda^2$, and for a boundary condition $\mathbf{H}(x=0) = \mathbf{H}_0$, it gives

$$\mathbf{H}(x) = \mathbf{H}_0 e^{-x/\lambda}. \quad (2.4)$$

Thus there is a thin layer of thickness λ , known as the *London penetration depth*, where the magnetic field penetrates the superconductor. The derivation above requires $\nabla \cdot \mathbf{H} = 0$. From the defining relation of the vector potential \mathbf{A} ($\mathbf{H} = \nabla \times \mathbf{A}$), the vector potential is required to be in the class of functions satisfying $\nabla \cdot \mathbf{A} = 0$ to satisfy a similar equation. This class of vector potential fields is called *London gauge*.

II.3. Two types of superconductors

The superconductors discussed so far are called type-I, and have two separate states, superconducting or normal state. Superconductivity is destroyed as the magnetic field H reaches some critical level H_c . This critical magnetic field depends on temperature T . Thus, superconducting state exists only in a particular region in a phase diagram in H-T plane (Fig. 3). In the phase diagram in H-T plane, type-I superconductors are superconducting below an $H_c(T)$ curve (dashed line), normal above the curve. The sample is either superconducting or normal as a whole, except the surface layer

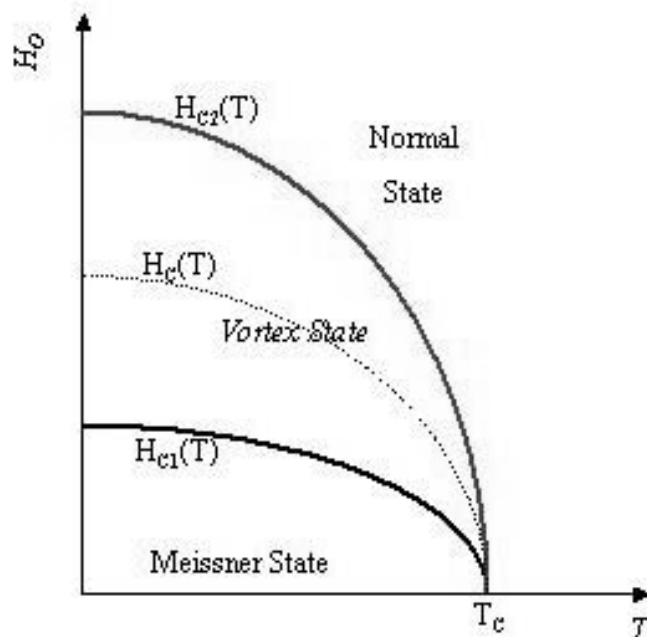


Fig. 3. Phase diagram of superconductors

of the penetration depth λ .¹ In the phase diagram there are two other critical fields H_{c1} and H_{c2} , and they border the regions corresponding to different superconducting states, which will be explained below.

In 1957, a Russian physicist A. A. Abrikosov discovered from his solution to the Ginzburg-Landau equations² a new kind of superconducting state in which magnetic

¹There is a metastable state called the *intermediate state* in which the superconducting phase coexists with the normal phase below H_c in a finite sample, as it typically happens in the first-order phase transitions.

²Ginzburg-Landau theory (1950) [7] was suggested before the BCS theory (1957) [8].

flux penetrates the superconductor in a form of vortex filaments. This new state is called appropriately the *mixed state* since the two states are mixed. Abrikosov has found that the new state occurs depending only on a single property of superconductors called the Ginzburg-Landau parameter κ . The mixed state occurs for $\kappa > 1/\sqrt{2}$. So the superconductors with $\kappa > 1/\sqrt{2}$ are called type-II, while the ones with $\kappa < 1/\sqrt{2}$ are called type-I. [9]

The mixed state in type-II superconductors exists between the lower critical field H_{c1} and the upper critical field H_{c2} curves in the phase diagram. When $H_{c1} < H < H_{c2}$, the magnetic flux can penetrate the material but not completely or uniformly, rather in the form of discrete flux lines, which are also super-current vortex lines. Around the center of each vortex line, a neighborhood with the radius of order ξ (called the coherence length) remains in the normal state. Around this vortex core, superconducting electrons move in circular paths like vortex flows in fluid dynamics. These supercurrents induce a magnetic field persisting over a distance on the order of the penetration depth λ . In the region between the vortices, the material is in the superconducting state. The material returns to its normal state when $H > H_{c2}$. In this case, superconductivity is completely destroyed being saturated with vortices.

It is remarkable that A. A. Abrikosov has found a new superconducting state and created a currently very active field of research by solving the Ginzburg-Landau equations. He was awarded the Nobel prize in Physics in 2003, with V. L. Ginzburg and A. J. Leggett. [10, 11]

D. Saint-James and P. G. Gennes [12, 13] have shown (again by solving the Ginzburg-Landau equations!) that at a metal-insulator interface, superconductivity can nucleate in a surface layer of thickness $\sim \xi$ in a magnetic field parallel to the surface. The corresponding critical magnetic field H_{c3} is about 70 percent higher than H_{c2} , at which nucleation occurs in the entire volume of the material. This

$H_{c3}(T) = 1.695H_{c2}(T)$ may be represented in another curve on the phase diagram.

One of the consequences of this *surface conductivity* is that a sample can carry a surface supercurrent over a wide range of fields in which no volume superconductivity could be measured. This surface sheath of supercurrent in a finite sample is sometimes called a giant vortex. [14, 15, 16, 17, 18] This giant vortex state regained research interests recently, e.g. [19].

CHAPTER III

MICROSCOPIC THEORY

Many introductory textbooks on superconductivity start with a chapter about the Ginzburg-Landau equations typically with a statement such as, Landau's theory of second-order transition applied to a "postulated" free energy produces the Ginzburg-Landau equations. Although correct, the statement is nevertheless closer to the end rather than the beginning of a long chain of reasonings. Landau's theory of second-order transition is a refined theory elucidating the relation between crystal symmetry and phase transitions. By applying the paradigm taken from the Landau theory to superconductors, the Ginzburg-Landau theory nicely weaves the microscopic theory of quasi-particles around the atomic lattice and a macroscopic description for the evolution of a superconducting phase in a material. In that sense, the Ginzburg-Landau theory penetrates to a deeper level than other phenomenological models. The microscopic theory presented in this chapter is at the foundation of Ginzburg-Landau theory and also reveals its beauty. At the same time, this fundamental understanding is valuable for those who study superconductivity at a research level. Ultimately this chapter is aimed at showing the existence of a macroscopically large pool of the carriers of superfluid motion in superfluids (called the Bose-Einstein condensate), and an analogous condensate of paired electrons (Cooper pairs) in superconductors. The wave functions of these condensates (not of individual particles) provide the link between the microscopic and macroscopic descriptions. The contents of this chapter are mostly from Refs. [20, 21, 22, 23, 24, 25] and the papers quoted therein.

III.1. Quasi-particles in quantum liquids

The calculation of thermodynamic quantities for a *macroscopic* body starts with its partition function, which requires the knowledge of the energy spectrum of the system, i.e. energy levels E_{nN} . In a liquid (*i.e.* systems of strongly interacting particles) we cannot refer to states of the individual atoms, but only to quantum-mechanical stationary states of the whole liquid.

At sufficiently low temperatures, we consider only the weakly excited levels of the liquid, that lie close to the ground state. According to the quantum-mechanical correspondence principle, these elementary excitations behave like quasi-particles moving in the volume occupied by the body and possessing definite energies ε and momenta \mathbf{p} .

An elementary excitation is not a single stationary state of the system, but a superposition of a large number of stationary states within a narrow range of energy (packet). There is a finite probability of transition between the constituent states in the packet, leading to the broadening of the energy spectrum. This is prescribed as the diffusion of a packet (or in other words, damping of the excitation). This damping process can be viewed as the result of “decomposition” and “scattering” of quasi-particles as they interact between one another. The process of decomposition of one excitation into several others occurs only for fairly large energies, while the scattering of excitations occurs for fairly high density of quasi-particles. Since neither is important at low temperatures, an ideal gas model of quasi-particles can be employed. [23] So it is assumed that any energy level can be written as the sum of the energies of a certain number of quasi-particles, as in the case of ideal gases. That is, the role of gas particles is taken by elementary excitations (quasi-particles) of the same number as atoms and obey statistics that corresponds to the nature of

particles.¹

III.2. Superfluidity

Below 2.19 K, liquid He⁴ (called helium II in this region) shows several extraordinary properties, one of which is that it flows through narrow capillaries or slits without exhibiting viscosity. This remarkable property is called *superfluidity*.²

Consider a liquid flowing along a capillary at a constant velocity \mathbf{v} . (We call this coordinate system K .) In a coordinate system moving with the liquid, the walls of the capillary move with velocity $-\mathbf{v}$, and the liquid is at rest, initially. (We call this coordinate system K_0 .) With no viscosity, nothing can happen further. With viscosity, however, as time passes, the liquid at rest must also begin to move. Gradually elementary excitations begin to appear in the liquid.

The energy E_0 and momentum \mathbf{P}_0 of the liquid in K_0 is related to those in K as³

$$E = E_0 + \mathbf{P}_0 \cdot \mathbf{v} + \frac{1}{2}Mv^2, \quad \mathbf{P} = \mathbf{P}_0 + M\mathbf{v}, \quad (3.1)$$

where M is the mass of the liquid. A single elementary excitation with momentum \mathbf{p} and energy $\varepsilon(p)$ appears in the liquid, $E_0 = \varepsilon$ and $\mathbf{P}_0 = \mathbf{p}$, since the rest of the liquid is quiescent. Then $E = \varepsilon + \mathbf{p} \cdot \mathbf{v} + \frac{1}{2}Mv^2$ and $\mathbf{P} = \mathbf{p} + M\mathbf{v}$.

¹In nature the wave function of a system of N identical particles is either totally symmetrical or totally antisymmetrical under the interchange of any pair. If it is symmetrical, the wave function remains the same when two particles are exchanged in the system. Such particles are called *bosons* and satisfy Bose-Einstein statistics. In the other case, the wave function changes sign under exchange of two particles. The particles are called *fermions* and satisfy Fermi-Dirac statistics. That is to say, the state of the system of *identical* Fermi particles is *not* the same after a pair of identical fermions in it are exchanged. The *spin statistics theorem* asserts that integer spin particles are bosons and half-integer spin particles are fermions.

²He³ also becomes superfluid, but at $\sim 10^{-3}$ K. [22]

³This is a consequence of Galileo's relativity principle.

The expression $\varepsilon + \mathbf{p} \cdot \mathbf{v}$ in E is the change in energy due to the appearance of the excitation and $\frac{1}{2}Mv^2$ is the kinetic energy of the liquid. If the excitation is to appear, the change $\varepsilon + \mathbf{p} \cdot \mathbf{v}$ must be negative, since the energy of the moving liquid cannot increase. That is, $\varepsilon + \mathbf{p} \cdot \mathbf{v} < 0$. This leads to $v > \varepsilon/p$, since $-pv \leq \mathbf{p} \cdot \mathbf{v} \leq pv$, hence $\varepsilon - pv < \varepsilon + \mathbf{p} \cdot \mathbf{v} < 0$. Hence excitations cannot appear in the liquid for velocities less than ε/p . If $(\varepsilon/p)_{min}$ is finite, then a flow with velocity $v < (\varepsilon/p)_{min}$ cannot become slower, and the liquid exhibits superfluidity. Thus we have the *superfluidity condition*

$$v < \varepsilon/p. \tag{3.2}$$

Note the superfluidity condition (3.2) depends on the shape of the energy spectrum $\varepsilon(p)$ of the excitations appearing in the liquid. Geometrically, the ratio ε/p is the slope of a line drawn from the origin to a point on the curve $\varepsilon(p)$, in the $p - \varepsilon$ plane. The superfluidity condition (3.2) says the curve $\varepsilon(p)$ should not touch or pass the origin except at $p = 0$. For example, when there is an energy gap in the spectrum between the excited states and the ground state, the liquid is a superfluid.

III.2.1. Wave function of the Bose superfluid

In a Bose superfluid, a macroscopically large number of particles have exactly zero momentum.⁴ These particles form the *Bose-Einstein condensate in momentum space*. In an ideal Bose gas at $T = 0$, all its particles are in the condensate. In a general Bose liquid, only small portion of particles are in the condensate even at $T = 0$.

We use the method of second quantization [21] which defines the quantum-mechanical operators to create (or annihilate) a particle with an appropriate wave function. Considering an ideal Bose gas (a system of non-interacting bosons, not

⁴This does *not* mean that the particles are at rest. They have zero momentum under the Heisenberg uncertainty principle as was discussed in the chapter I.

quasi-particles), the Heisenberg field operator $\hat{\Psi}(\mathbf{r}, t)$ is written in the expansion of the plane wave function

$$\hat{\Psi}(r, t) = \frac{1}{\sqrt{V}} \sum_{\mathbf{p}} \hat{a}_{\mathbf{p}} \psi(r, t) = \frac{1}{\sqrt{V}} \sum_{\mathbf{p}} \hat{a}_{\mathbf{p}} \exp \left\{ \frac{i}{\hbar} \mathbf{p} \cdot \mathbf{r} - \frac{i}{\hbar} \frac{p^2}{2m} t \right\}. \quad (3.3)$$

where $\hat{a}_{\mathbf{p}}$ is the annihilation operator for a particle. The particle creation operator $\hat{a}_{\mathbf{p}}^+$ follows from the commutation rule

$$\hat{a}_{\mathbf{p}} \hat{a}_{\mathbf{p}}^+ - \hat{b}_{\mathbf{p}}^+ \hat{b}_{\mathbf{p}} = 1. \quad (3.4)$$

The creation field operator $\hat{\Psi}^+(r, t)$ is defined as a similar sum of $\hat{a}_{\mathbf{p}}^+ \psi^*(r, t)$. Note the term with $\mathbf{p} = 0$ does not change in time. When an ideal Bose gas is in the ground state ($\mathbf{p}=0$), all the particles are in the condensate and their number is called an occupation number, N_0 . It can be shown the creation and annihilation operators applied to the ground state results in $\hat{a}_0^+ \hat{a}_0 = N_0$ and $\hat{a}_0 \hat{a}_0^+ = N_0 + 1$. This non-commutativity ($\hat{a}_0 \hat{a}_0^+ - \hat{a}_0^+ \hat{a}_0 \neq 0$) of the operators \hat{a}_0 and \hat{a}_0^+ may be ignored if N_0 is very large. That is, changing the order of the operators \hat{a}_0 and \hat{a}_0^+ makes differences in the occupation number of the state by one, but for already large occupation number this is negligible. Putting $\hat{a}_0 \hat{a}_0^+ - \hat{a}_0^+ \hat{a}_0 \approx 0$ enables us to regard the operators as classical quantities, i.e. numbers, and it immediately follows $\hat{a}_0 = \hat{a}_0^+ = \sqrt{N_0}$. We give the operator $\hat{\Psi}(r, t)_{\mathbf{p}=0}$ a special symbol $\hat{\Xi}$. That is,

$$\hat{\Xi} = \hat{a}_0 / \sqrt{V}. \quad (3.5)$$

For a condensate with a macroscopically large number of particles, this operator can be regarded as an ordinary number that does not change in time.

In the general case of an arbitrary *Bose liquid*, we note that changing the number of particles in the condensate by 1 does not essentially affect the state of the system because the number of particles in the condensate is still large. That is, adding (or

removing) one particle in the condensate converts a state of a system of N particles into essentially the “same” state of a system of $N \pm 1$ particles.⁵ In particular, the ground state remains the ground state. These operations of addition and removal expressed with the creation and annihilation operators above, lead to defining $\hat{\Xi}$ and $\hat{\Xi}^+$, the part of the $\hat{\Psi}$ operators that changes the number of particles in the condensate by 1. $\hat{\Xi}$ and $\hat{\Xi}^+$ are defined as

$$\hat{\Xi}|m, N + 1 \rangle = \Xi|m, N \rangle \quad (3.6)$$

and

$$\hat{\Xi}^+|m, N \rangle = \Xi^*|m, N + 1 \rangle \quad (3.7)$$

where the symbols $|m, N \rangle$ and $|m, N + 1 \rangle$ denote two “like” states, differing only as regards the number of particles in the system, m denotes the level in the energy spectrum in the condensate, and Ξ is a complex number.⁶ It can be shown there exists a limiting expected value for this Ξ as $N \rightarrow \infty$. That is,

$$\begin{aligned} \lim_{N \rightarrow \infty} \langle m, N | \hat{\Xi} | m, N + 1 \rangle &= \lim_{N \rightarrow \infty} \langle m, N | \Xi | m, N \rangle = \Xi \\ \lim_{N \rightarrow \infty} \langle m, N + 1 | \hat{\Xi}^+ | m, N \rangle &= \lim_{N \rightarrow \infty} \langle m, N + 1 | \Xi^* | m, N + 1 \rangle = \Xi^* \end{aligned} \quad (3.8)$$

The the difference between the states $|m, N \rangle$ and $|m, N + 1 \rangle$ disappears as $N \rightarrow \infty$ and Ξ becomes the mean value of that state. [20] Ξ is related to the population of the condensate as shown below.

In a homogeneous liquid at rest, Ξ is independent of the coordinates and is simply

$$\Xi = \sqrt{n_0}, \quad (3.9)$$

⁵The addition or removal of the particle is to occur in an infinitely slow process.

⁶ Ξ is the eigenvalue of the operator $\hat{\Xi}$ applied to the eigenket $|m, N \rangle$.

where $n_0 = N_0/V$ is the number of condensate particles per unit volume of the liquid. That is, we have N_0 particles in the state of $p = 0$ in a volume V of the liquid. If the liquid is in a superfluid motion, (or in non-uniform and non-stationary external conditions) the Bose-Einstein condensation again occurs, but not in the state with $p = 0$. The quantity Ξ is now a function of coordinates and time, representing the wave function of particles in the condensate state. Normalized by the condition $|\Xi|^2 = n_0$, Ξ can be expressed as

$$\Xi(\mathbf{r}, t) = \sqrt{n_0(\mathbf{r}, t)} e^{-i\phi(\mathbf{r}, t)}. \quad (3.10)$$

Because of the macroscopically large number of particles in the condensate state, the wave function of this state becomes a classical macroscopic quantity. From this wave function, for example, the macroscopic current density of condensate particles can be calculated

$$\mathbf{j} = \frac{i\hbar}{2m} (\Xi \nabla \Xi^* - \Xi^* \nabla \Xi) = \frac{\hbar}{m} n_0 \nabla \phi \quad (3.11)$$

One can see the large population in the Bose-Einstein condensate provides with the macroscopic appearance of superfluidity.

III.3. Superfluidity of a Fermi gas

In this section we consider a degenerate almost ideal Fermi gas with attraction between the particles, known as *BCS model*. (BCS stands for Bardeen-Cooper-Schrieffer.) The attractive interaction between identical particles is unusual and should result in a different kind of energy spectrum. Normally one would assume repulsive interactions between the fermions, such as electrons.

Cooper [26] showed that the ground state of the system (Fermi sea) is unstable with respect to the formation of bound states of pairs of particles, when the net inter-

action between the particles is attractive. The physical consequence of this instability is an “avalanche” of the particles that form bound states lying near the Fermi surface in \mathbf{p} -space and having equal and opposite momenta and antiparallel spins - the *Cooper effect*. Here we show briefly the nature of superfluidity of the gas of Cooper pairs.

The electron pairing precludes the use of operators $\hat{a}_{\mathbf{p}\alpha}$ and $\hat{a}_{\mathbf{p}\alpha}^+$, defined for free state of individual particles of the gas. A different set of operators needs to be defined, the simplest will be the linear combinations of the operators of particles with opposite momenta and spins; the suffixes + and - refer to the two values of the spin components.

$$\hat{b}_{\mathbf{p}-} = u_{\mathbf{p}}\hat{a}_{\mathbf{p}-} + v_{\mathbf{p}}\hat{a}_{-\mathbf{p}+}^+ \quad (3.12)$$

$$\hat{b}_{\mathbf{p}+} = u_{\mathbf{p}}\hat{a}_{\mathbf{p}+} - v_{\mathbf{p}}\hat{a}_{-\mathbf{p}-}^+ \quad (3.13)$$

The creation operators $\hat{b}_{\mathbf{p}\alpha}^+$ come from the commutation rule

$$\hat{b}_{\mathbf{p}\alpha}\hat{b}_{\mathbf{p}\alpha}^+ + \hat{b}_{\mathbf{p}\alpha}^+\hat{b}_{\mathbf{p}\alpha} = 1. \quad (3.14)$$

The operators $\hat{b}_{\mathbf{p}\alpha}^+$ create quasi-particles that are mutually orthogonal and also orthogonal to the ground state. [24] The quasi-particle occupation number $n_{\mathbf{p}\alpha}$ is defined with these new operators

$$\hat{b}_{\mathbf{p}\alpha}^+\hat{b}_{\mathbf{p}\alpha} = n_{\mathbf{p}\alpha}, \quad (3.15)$$

$$\hat{b}_{\mathbf{p}\alpha}\hat{b}_{\mathbf{p}\alpha}^+ = 1 - n_{\mathbf{p}\alpha}. \quad (3.16)$$

The coefficients $u_{\mathbf{p}}$ and $v_{\mathbf{p}}$ are the wave functions in the method of second quantization (c.f. eq.(3.3)), of the particles in the bound states. After some tedious

calculation ⁷ $u_{\mathbf{p}}$ and $v_{\mathbf{p}}$ are given by

$$u_{\mathbf{p}}^2 = \frac{1}{2} \left(1 + \frac{\eta_p}{\sqrt{\Delta^2 + \eta_p^2}} \right), \quad (3.18)$$

$$v_{\mathbf{p}}^2 = \frac{1}{2} \left(1 - \frac{\eta_p}{\sqrt{\Delta^2 + \eta_p^2}} \right). \quad (3.19)$$

where $\eta_p = p^2/2m - \mu$ (kinetic energy minus chemical potential), the *energy gap* $\Delta = g/V \sum_{\mathbf{p}} u_{\mathbf{p}} v_{\mathbf{p}} (1 - n_{\mathbf{p}+} - n_{\mathbf{p}-})$, and g is the coupling constant. Noting $n_{\mathbf{p}+} = n_{\mathbf{p}-} \equiv n_{\mathbf{p}}$ for pairing, the Fermi distribution function for occupation numbers $n_{\mathbf{p}} = [e^{\varepsilon/T} + 1]^{-1}$ in equilibrium leads to the energy spectrum ⁸

$$\varepsilon(p) = \sqrt{\Delta^2 + \eta_p^2}. \quad (3.20)$$

It is clear the quasi-particle energy cannot be less than the value Δ at $\eta_p = 0$. (When $\eta_p = 0$, $\mu = \varepsilon_F = p_F^2/2m$ hence $p = p_F$ on Fermi surface.) This energy spectrum satisfies the superfluidity condition since the minimum value of ε/p is not zero. Thus a Fermi gas with attraction between the particles must have the property of superfluidity for $v < \varepsilon/p$. The excited states of the system are separated from the ground state by this energy gap. The quasi-particles (i.e. the elementary excitations), due to half-integral spin, must appear in pairs. In this sense the gap may be said to be 2Δ . This quantity 2Δ may be interpreted as the binding energy of the Cooper pair. Since only the interaction between pairs of particles in the singlet s-state (spherically

⁷A Hamiltonian for negative interaction needs to be defined with coupling constant V , then the energy of the system

$$E = 2 \sum_{\mathbf{p}} \eta_{\mathbf{p}} v_{\mathbf{p}}^2 + \sum_{\mathbf{p}} \eta_{\mathbf{p}} (u_{\mathbf{p}}^2 - v_{\mathbf{p}}^2) (n_{\mathbf{p}+} + n_{\mathbf{p}-}) - \frac{g}{V} \left[\sum_{\mathbf{p}} u_{\mathbf{p}} v_{\mathbf{p}} (1 - n_{\mathbf{p}+} - n_{\mathbf{p}-}) \right]^2 \quad (3.17)$$

is minimized to obtain u_p and v_p by variational method, such as $\delta E/\delta u_p = 0$.

⁸Here again variational method is used to obtain $\varepsilon = (\delta E/\delta n_{\mathbf{p}\alpha})_{u_p, v_p}$. Again $\varepsilon_{\mathbf{p}+} = \varepsilon_{\mathbf{p}-} \equiv \varepsilon_{\mathbf{p}}$.

symmetric) were considered, the pairs have zero total spin. Thus they behave like Bose particles and may accumulate in any numbers at the level with the total momentum zero. In this sense, the phenomenon is analogous to the Bose-Einstein condensation in a Bose gas; in this case the condensate is the ensemble of Cooper pairs.

III.3.1. Wave function of the superfluid Fermi gas

Previously, the existence of a Bose-Einstein condensate in a Bose system was translated as a statement that the removal or addition of one condensate particle does not change the state of a macroscopic system. The same must be true for the condensate of Cooper pairs in a superfluid Fermi system. The state of the system cannot be altered when the number of pairs in the condensate increases or decreases by unity.

This is expressed mathematically by the presence of non-zero limiting values ($N \rightarrow \infty$) of the matrix elements for the operator products $\hat{\Psi}_\beta(X_2)\hat{\Psi}_\alpha(X_1)$ and $\hat{\Psi}_\alpha^+(X_1)\hat{\Psi}_\beta^+(X_2)$.⁹ The former is the pair annihilation operator and the latter the pair creation operator, which is also the Hermitian conjugate of the former. These matrix elements relate the “like” states of systems, differing only by the removal or addition of one pair of particles. The the difference between the states $|m, N \rangle$ and $|m, N + 2 \rangle$ disappears as $N \rightarrow \infty$ if

$$\begin{aligned} & \lim_{N \rightarrow \infty} \langle m, N | \hat{\Psi}_\beta(X_2)\hat{\Psi}_\alpha(X_1) | m, N + 2 \rangle \\ &= \lim_{N \rightarrow \infty} \langle m, N + 2 | \hat{\Psi}_\alpha^+(X_1)\hat{\Psi}_\beta^+(X_2) | m, N \rangle^* \neq 0. \end{aligned} \quad (3.21)$$

This is the mathematical statement of the existence of the condensate and the expected values converge to a mean value.

In general, Green’s functions need to be defined to treat the interactions of the

⁹The symbols X_1, X_2 represent the space-time coordinates (\mathbf{r}_1, t_1) and (\mathbf{r}_2, t_2) .

particles in the system in the space-time (\mathbf{r}, t) . This leads to the celebrated *Feynmann diagram technique*. We do not go in that direction, rather we only pay attention to the “anomalous” Green functions defined by ¹⁰

$$\begin{aligned} iF_{\alpha\beta}(X_1, X_2) &= \langle N | T \hat{\Psi}_\alpha(X_1) \hat{\Psi}_\beta(X_2) | N + 2 \rangle \\ iF_{\alpha\beta}^+(X_1, X_2) &= \langle N + 2 | T \hat{\Psi}_\alpha^+(X_1) \hat{\Psi}_\beta^+(X_2) | N \rangle. \end{aligned} \quad (3.23)$$

where the symbol T denotes the *chronological product*. The operators following the symbol T have to be arranged from right to left in order of increasing times t_1, t_2 . These functions contain the operator products defining the condensate of Cooper pairs in eq. (3.21) and express the interaction of particles in space-time. Recalling the spherical symmetry of the state of Cooper pair, we can isolate the spin dependence of the Green function for a non-ferromagnetic system by a unit antisymmetric spinor $g_{\alpha\beta}$ (which is not of interest here):

$$F_{\alpha\beta} = g_{\alpha\beta} F(X_1, X_2), \quad F_{\alpha\beta}^+ = g_{\alpha\beta} F^+(X_1, X_2). \quad (3.24)$$

Just as the function $\Xi(X)$ in Bose liquids had the sense of a wave function for particles in the condensate, so the function $iF(X_1, X_2)$ may be regarded as the wave function of Cooper pairs in the condensate. Then the function

$$\Xi(X) \equiv iF(X, X) \quad (3.25)$$

will be the wave function for the motion of these pairs as a whole. The other function F^+ is related to Ξ by the relation $F^+(X, X) = i\Xi^*(X)$. Interested readers are referred

¹⁰The ordinary Green functions are defined as

$$iG_{\alpha\beta}(X_1, X_2) = \langle N | T \hat{\Psi}_\alpha(X_1) \hat{\Psi}_\beta^+(X_2) | N \rangle. \quad (3.22)$$

to references for more details. [20, 23]

CHAPTER IV

GINZBURG-LANDAU THEORY

The existence of crystal lattice makes superconductors more complicated system to study than superfluids. Modeling the interactions between electrons and ions makes the mathematics involved with the process laborious and thus hard to apply to a system of macroscopic size.

In this chapter we introduce a phenomenological but powerful model proposed by V. L. Ginzburg and L. D. Landau. [7] The basic concepts such as second-order phase transition, critical phenomena, and order parameter are introduced in connection with Landau's theory of second-order phase transition. Applying Landau's theory of second-order transition to the normal-superconductor transition phenomena, the Ginzburg-Landau equation is derived in terms of the order parameter.

The Ginzburg-Landau equation is a governing equation for the order parameter. However, an order parameter is not exactly a physical quantity, nor a reserved term solely for superconductors. The order parameter is defined in any critical phenomena. That is the reason why we visit basic terms in this chapter, although only the nominal number of necessary terms. The contents of this chapter are mostly from Refs. [27, 28, 20, 24, 29, 25] and the papers quoted therein.

IV.1. Second-order phase transitions and critical phenomena

Ordinary phase transitions like the phase change associated with freezing or boiling of water is termed as a first-order transition. In the phase diagram of water in the $P - v$ plane, the transitions between liquid-solid or liquid-vapor occur across the phase equilibrium curve, when it is below critical point. The difference in molar entropies of each phase incurs the heats of phase change, which is known as latent

heats. Since the two states between which a first-order transition occurs are distinct, they occur at separate regions in the thermodynamic configuration space. When the system is going through a first-order transition from one phase to the other, there occurs a coexistence of different phases such as liquid-solid (e.g. ice forming inside the water) corresponding to the linear combination of the two minimum energies corresponding to each of the pure phases. The point at which all the three phases (solid, liquid, and vapor) coexist is called the triple point.

As the critical point is approached, the phases lose their distinctive identities, and finally disappears beyond critical point into a single phase called the fluid. This transition to the new phase right across the critical point is defined as a second-order transition. Since the coexistence of distinctive phases is no longer possible, entropy is continuous and heat of transition is absent. One other noteworthy point is that the thermodynamic fluctuations show divergent growth as critical point is approached. Enormous fluctuations, in such a quantity as density (reported as the “critical opalescence”) is observed and “generalized susceptibilities” such as heat capacity and compressibility diverge at the critical point.

These characteristics of critical phenomena discussed above are observed in many systems. For example, the magnetic susceptibility in a ferromagnetic system diverges near the critical transition, and the magnetic moment shows divergent fluctuation. Similar transition happens in a ferroelectric system with electric dipole moment. [27, 5] One may notice that, fluctuations that are suppressed and averaged out in stable thermodynamic systems below the critical point, would have a dominant role in the physical processes beyond it.

IV.2. Landau's theory of second-order phase transition

The quantitative theory of second-order phase transitions is due to L. D. Landau, who first showed the general relation between the phase transitions and the change in symmetry of the body. The state of a body changes when it goes through the transition between phases of different symmetry, such as between crystal and liquid or between different crystal structures. However, in any state the body has only one symmetry.

The transition between different crystal structures usually takes place with a sudden rearrangement of the crystal lattice and thus the state of the body changes discontinuously. This results in the discontinuous changes in the thermodynamic properties, i.e. first-order phase transition. However, there are transitions such that the change in the state is continuous while a change in symmetry occurs. For example, BaTiO_3 changes instantly from cubic to tetragonal lattice with no discontinuous change in the state of the body at the transition temperature. The reason is that an arbitrarily small displacement of the atoms from their original lattice sites is sufficient to change the symmetry of the lattice to the other in this crystal. The crystal symmetry changes instantly and abruptly, even though the positions (and arrangement) of atoms in the crystal make infinitesimally small changes. The resulting transition from one crystal structure to another is called a phase transition of the second-order. Thus a second-order phase transition is continuous in the change of the state of the body and discontinuous in the change of the symmetry. The body, however, belongs to only one of the two phases of symmetry at any instant. Whereas two phases of different states are in equilibrium at a phase transition point of first-order, the two phases have the same state at a transition point of second-order.

BaTiO_3 is an example of a change in crystal symmetry by atomic displacements.

The change in symmetry in a second-order transition may occur from a change in the *ordering* of the crystal. The concept of ordering arises when there are more lattice points to be occupied than atoms available to occupy. Since we cannot actually count the number of lattice sites or atoms, the probabilities of occupation at the lattice sites are evaluated. If these probabilities become uniform, this means a new configuration of invariance (symmetry) has appeared. The symmetry of the lattice is increased and the crystal is said to be *disordered*. That is, if symmetry increases, order decreases.

A second-order transition can be induced by a change in symmetry of some other property instead of the atomic configuration. For example, at the Curie points¹ there is a change in symmetry of the arrangement of the elementary magnetic moments in a ferromagnetic or antiferromagnetic substance, at which the currents \mathbf{j} in the body disappears. Other examples are the transition of a metal to the superconducting state and that of liquid helium to the superfluid state.

Since the states of the two phases are the same at a transition point of the second-order, the symmetry of the body at the transition point itself must contain all the symmetry elements (rotations, reflections and translational periods, etc.) of both phases. On the other hand, the symmetry of the state at the transition point is the symmetry of only one of the two phases as discussed above. Thus they cannot be two totally different kinds of symmetries, one symmetry must be higher than the other. The phase of the higher symmetry includes all the symmetry elements of that of the lower symmetry and all the other additional symmetry elements. Therefore, we can define a quantity η , called the *order-parameter*, that is zero in the symmetrical phase and non-zero otherwise.² The continuity of the change of state in a phase transition

¹Phase transition points of the second-order are also called *Curie points*, especially for magnetic materials.

²For brevity we shall arbitrarily call the more symmetrical phase simply the *sym-*

of second-order is expressed mathematically by the fact that the quantity η takes arbitrarily small values near the transition point. Since the thermodynamic functions of the state of the body (its entropy, energy, volume, etc.) vary continuously as the transition point of the second-order is passed, we expand the Helmholtz free energy $\mathcal{F}(\mathcal{P}, \mathcal{T}, \eta)$ in powers of η :

$$\mathcal{F}(P, T, \eta) = \mathcal{F}_0 + \alpha\eta + A\eta^2 + C\eta^3 + B\eta^4 + \dots, \quad (4.1)$$

where the coefficients α, A, B, C, \dots are functions of P and T . Further analysis and simplification of this expression varies depending on each application.

IV.3. The Ginzburg-Landau equations

In the Landau theory of phase transitions of the second-order, an order parameter was defined to describe quantitatively the change between the “unsymmetrical” and “symmetrical” phase. For a superconductor, the natural choice for the order parameter is the condensate wave function, $\Xi(\mathbf{r}, t) = \sqrt{n_0(\mathbf{r}, t)}e^{i\phi(\mathbf{r}, t)}$, where n_0 is the number of Cooper pairs per unit volume in the condensate. In our Fermi liquid we define a quantity Ψ that is proportional to Ξ but is normalized such that $|\Psi|^2 = n_s$, where n_s can be taken as the number density of superconducting electrons.³ Once we define the wave function

$$\Psi = \sqrt{n_s}e^{i\phi}, \quad (4.2)$$

metrical one, and the less symmetrical phase the *unsymmetrical* one.

³To simplify derivation, a cubic symmetry (isotropy) is assumed. This has two consequences. First, the superconducting state is characterized by n_s , the superelectron density. Next, the supercurrent is seen to be simply proportional to the gradient of the phase of the condensate wave function, with no need of second-order tensor coefficient depending on anisotropy.

the supercurrent density is expressed as

$$\mathbf{j}_s = \frac{e_s \hbar}{m_s} |\Psi|^2 \nabla \phi = -\frac{ie_s \hbar}{2m_s} (\Psi^* \nabla \Psi - \Psi \nabla \Psi^*), \quad (4.3)$$

where e_s is the charge of a Cooper pair and m_s is the mass of a Cooper pair. Note that the definition of supercurrent density depends on the existence of the condensate wave function only, prior to the definition of the order parameter.

Following the general idea of the Landau theory, we start with the free energy being expressed as a functional of $\Psi(\mathbf{r})$. Near the transition point, the free energy density is expanded in powers of the small order parameter Ψ and its derivatives with respect to the coordinates. The order parameter Ψ defined above is a quantity proportional to the Green's function $F(X, X) \equiv -i\Xi(X)$ (see eq.(3.25)). Since $F(X, X)$ is constructed from two field operators $\hat{\Psi}$ (see eq.(3.23)), an arbitrary change of phase of these operators by $\frac{\alpha}{2}$, *i.e.* $\hat{\Psi} \rightarrow \hat{\Psi} e^{i\alpha/2}$, introduces a change of phase of the function F by α . And this phase change appears in the order parameter: $\Psi \rightarrow \Psi e^{i\alpha}$. Since physical quantities must not change by this arbitrariness, this excludes odd powers of Ψ in the expansion of the free energy.

Now the Helmholtz free energy per unit volume in a superconducting body is written as an expansion of the non-relativistic form (in the absence of magnetic field)

$$f_s = f_n^0 + \alpha |\Psi|^2 + \frac{1}{2} \beta |\Psi|^4 + \frac{1}{2m_s} \left| \frac{\hbar}{i} \nabla \Psi \right|^2. \quad (4.4)$$

Here, the order parameter Ψ is assumed to be complex scalar-valued function of position, such that $|\Psi|^2$ represents the local Cooper pair density, f_n^0 is the free energy of the normal state in the absence of field, and m_s is the effective mass of the Cooper pair. The fact that the above free energy contains only the first derivative of Ψ means only sufficiently slow variation of Ψ in space is considered. In a homogeneous

superconductor, (4.4) reduces to

$$f_s = f_n^0 + \alpha|\Psi|^2 + \frac{1}{2}\beta|\Psi|^4, \quad (4.5)$$

where the temperature dependent quantities $\alpha(T)$ and $\beta(T)$ satisfy:

$$\alpha(T) = \alpha_0 (T - T_c), \quad \alpha_0 > 0, \quad \beta(T) > 0 \quad (4.6)$$

Minimizing (4.5) with respect to the real and imaginary parts of Ψ yields two equilibrium values; one of which is $\Psi = 0$ for $T > T_c$, which is a trivial solution for normal state. The other solution is

$$|\Psi|^2 = -\alpha/\beta \equiv \Psi_\infty^2, \quad (4.7)$$

for $T < T_c$, which characterizes a uniformly superconducting (Meissner) state. The critical field strength H_c , which is used as a fundamental scale for the magnetic field, is given by

$$H_c = (4\pi\alpha^2/\beta)^{1/2}. \quad (4.8)$$

The Ginzburg-Landau penetration depth is defined as,

$$\lambda(T) = \left(\frac{m_s \beta c^2}{4\pi|\alpha|e_s^2} \right)^{1/2}. \quad (4.9)$$

Finally, the Ginzburg-Landau coherence length, which is related to Pippard's coherence length, is given by

$$\xi(T) = \left(\frac{\hbar^2}{2m_s|\alpha(T)|} \right)^{1/2}. \quad (4.10)$$

Both penetration depth and coherence length are temperature dependent and behave like $(T - T_c)^{-1/2}$. The Ginzburg-Landau parameter

$$\kappa(T) = \frac{\lambda(T)}{\xi(T)} \quad (4.11)$$

is a slowly varying function of temperature.

When a magnetic field is present, (4.4) has to be modified in two ways. First, the magnetic energy density $\mathbf{h}^2/8\pi$ (where the magnetic field $\mathbf{h} = \nabla \times \mathbf{A}$) must be added. Secondly, the gradient term should be changed to satisfy the gauge invariance. This is done by replacing the phase gradient $\nabla\phi$ with $\nabla\phi - e_s\mathbf{A}/\hbar c$. This results in the substitution $\nabla\Psi \rightarrow \nabla\Psi - (ie_s/\hbar c)\mathbf{A}\Psi$. Thus the integrated energy is

$$F_s = F_n^0 + \int_{\Omega} \left[\alpha|\Psi|^2 + \frac{1}{2}\beta|\Psi|^4 + \frac{1}{2m_s} \left| \left(\frac{\hbar}{i}\nabla - \frac{e_s}{c}\mathbf{A} \right) \Psi \right|^2 + \frac{1}{8\pi} |\nabla \times \mathbf{A}|^2 \right] d\Omega. \quad (4.12)$$

Here, in addition to the parameters defined above, the vector potential \mathbf{A} is a three-dimensional vector-valued function of position, and $e_s = 2e$ is the effective charge of the Cooper pairs. (Strictly speaking, this free energy is actually the magnetic Gibbs' energy.)

The desired differential equations for Ψ and \mathbf{A} are now found by minimizing the free energy as a functional of the three independent functions Ψ , Ψ^* , and \mathbf{A} . (Since the complex function Ψ has two real components, Ψ and Ψ^* must be regarded as independent functions in the variation. However, due to the symmetry of F with respect to Ψ and Ψ^* , minimization with respect to Ψ does not produce a new equation.)

Varying the free energy integral with respect to Ψ^* results in

$$\delta F = \int_{\Omega} \left[\alpha\Psi + \beta|\Psi|^2\Psi + \frac{1}{2m_s} \left(\frac{\hbar}{i}\nabla - \frac{e_s}{c}\mathbf{A} \right)^2 \Psi \right] \delta\Psi^* d\Omega + \frac{1}{2m_s} \oint_S \left(\frac{\hbar}{i}\nabla - \frac{e_s}{c}\mathbf{A} \right) \Psi \delta\Psi^* dS. \quad (4.13)$$

Putting $\delta F = 0$, we obtain the Ginzburg-Landau equation

$$\frac{1}{2m_s} \left(\frac{\hbar}{i}\nabla - \frac{e_s}{c}\mathbf{A} \right)^2 \Psi + \alpha\Psi + \beta|\Psi|^2\Psi = 0. \quad (4.14)$$

Similarly, the variation with respect to \mathbf{A} gives Maxwell's equation

$$\nabla \times \nabla \times \mathbf{A} = \frac{4\pi}{c} \mathbf{j} \quad (4.15)$$

and the current density

$$\mathbf{j} = -\frac{ie_s\hbar}{2m_s}(\Psi^*\nabla\Psi - \Psi\nabla\Psi^*) - \frac{e_s^2}{m_sc}|\Psi|^2\mathbf{A} \quad (4.16)$$

or

$$\mathbf{j} = \frac{e_s\hbar}{m_s}|\Psi|^2\nabla\phi - \frac{e_s^2}{m_sc}|\Psi|^2\mathbf{A}. \quad (4.17)$$

The surface integral in (4.13) gives the boundary condition at free surfaces of the sample:

$$\mathbf{n} \cdot \left(\frac{\hbar}{i}\nabla - \frac{e_s}{c}\mathbf{A} \right) \Psi = 0 \quad (4.18)$$

IV.3.1. Flux quantization

Inside the body far enough from the surface layer of the penetration of the field, the current density $\mathbf{j} = 0$. The vector potential \mathbf{A} is not zero, but only the magnetic field $\mathbf{H} = \nabla \times \mathbf{A}$ is zero. For slow enough variations of the phase ϕ and the potential \mathbf{A} , the circulation of \mathbf{A} along an arbitrary contour C is equal to the flux Φ of the magnetic field through a surface S bounded by the contour, i.e.

$$\oint_C \mathbf{A} \cdot d\mathbf{l} = \int_S \nabla \times \mathbf{A} \cdot d\mathbf{f} = \Phi. \quad (4.19)$$

On the other hand, since $\mathbf{j} = \frac{e_s\hbar}{m_s}|\Psi|^2 \left(\nabla\phi - \frac{e_s}{\hbar c}|\Psi|^2\mathbf{A} \right) = 0$,

$$\oint_C \mathbf{A} \cdot d\mathbf{l} = \frac{\hbar c}{e_s} \oint_C \nabla\phi \cdot d\mathbf{l} = \frac{\hbar c}{e_s} \delta\phi \quad (4.20)$$

where $\delta\phi$ is the change of phase of the wave function on passing round the contour. Since this function must be single-valued, it follows that the phase change $\delta\phi$ can only be an integral multiple of 2π . Thus we have the result

$$\Phi = \frac{\hbar c}{e_s} 2\pi n = n\Phi_0. \quad (4.21)$$

Since $2\pi\hbar = h$ and $e_s = 2e$, the flux quantum Φ_0 is usually written as

$$\Phi_0 = hc/2e = 2 \times 10^{-7} G \cdot cm^2 \quad (4.22)$$

IV.3.2. Gauge symmetry

The free energy (4.12) shown above contains terms in the form of covariant derivative [30]

$$D_\mu \equiv \partial_\mu - iA_\mu q, \quad (4.23)$$

which is to ensure the gauge invariance required for all physical phenomena. The free energy does not change under a gauge transformation with an arbitrary scalar function χ ,

$$\mathbf{A} \rightarrow \mathbf{A} + \nabla\chi, \quad \Phi \rightarrow \Phi + \chi \quad (4.24)$$

and

$$\Psi(x) \rightarrow e^{ies\chi}\Psi(x), \quad (4.25)$$

which can be immediately observed by introducing the gauge transformation into the free energy (4.12).

There is another and more profound viewpoint regarding the gauge symmetry in terms of the quantum state of the system. When there are more than one quantum states corresponding to a single energy level, they are called degenerate. The non-degenerate ground state is invariant under the gauge transformation since it is unique. If the ground state is degenerate, these degenerate states transform into each other under the gauge transformation. However, if we choose one particular state of these equivalent states, this state is not invariant under the gauge transformation any more. It is then said that the symmetry (invariance) of the Hamiltonian is spontaneously

broken in this state.⁴ For a superconductor the Hamiltonian is invariant under global gauge transformations ($\chi = \text{const}$). In the ground state the phase of the condensate wave function (order parameter) is arbitrary since it can be changed arbitrarily by χ . It can be fixed if we choose a specific gauge, and then the symmetry is spontaneously broken. [31]

Above statements can be illustrated more clearly in terms of Gibbs free energy (4.4). It is invariant under a global gauge transformation, i.e. $\Psi(x) \rightarrow e^{ies\chi}\Psi(x)$ where $\chi = \text{const}$. To simplify further, we assume the gradient is zero (or the spatial variation is extremely slow), in the remaining free energy terms β must be positive in order to have a finite minimum. If $\alpha > 0$, the minimum energy occurs at $|\Psi| = 0$, which corresponds to the normal state. The symmetry of this state is the same as the free energy. On the other hand, if $\alpha < 0$, the minimum energy occurs for $|\Psi| = \sqrt{-\alpha/\beta} \equiv \Psi_\infty$. (See Figure 4). Thus the ground state is infinitely degenerate since any state with $|\Psi| = \Psi_\infty e^{ies\chi}$ describe the same minimum energy configuration in the global gauge transform. If we fix χ , e.g. $\chi = 0$, we have a state with spontaneously broken symmetry. In the case of the free energy in a magnetic field (4.12), the free energy satisfies local gauge symmetry, with $\chi = \chi(\mathbf{x})$. The local gauge symmetry is spontaneously broken in the same way as global gauge symmetry. Furthermore, we can choose a local gauge to remove the coupling of the gauge field $\mathbf{A}(\mathbf{x})$ to the order parameter $\Psi(\mathbf{x})$ introduced by the original local gauge.

Moriarty *et al.* has applied the covariant derivative to ensure their Hamiltonian

⁴This argument can be broadened further, since gauge symmetry is just one of many symmetries, and in particular electromagnetic gauge is the simplest gauge group. Landau's phase transition theory also hinges on watching the internal symmetry of matter. Symmetry in modern physics is not merely an invariance in observation but a character of space-time, deciding the nature of matter and force. The three main pillars of modern physics are relativity, quantization, and symmetry. [32] The author is by no means qualified to expound this vast amount of theories in detail.

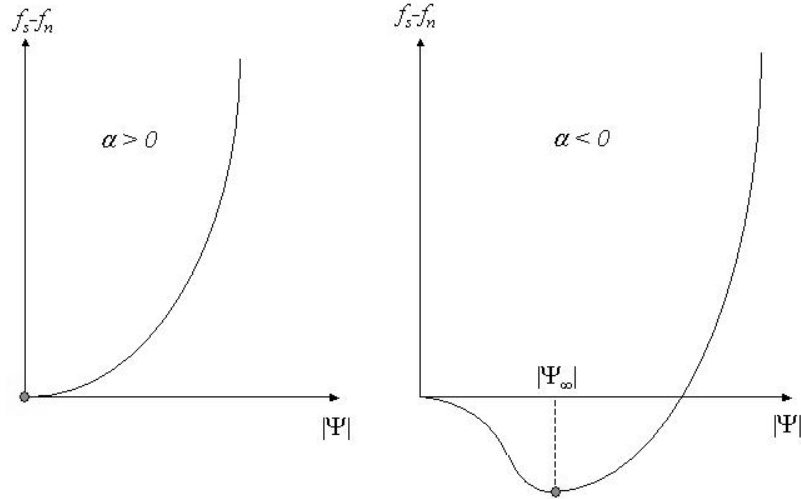


Fig. 4. Ginzburg-Landau free energy function for $\alpha > 0$ ($T > T_c$) and for $\alpha < 0$ ($T < T_c$). Heavy dots indicate equilibrium positions.

and action are symmetric over the sample and across the lattice sites in their extensive numerical simulation with Ginzburg-Landau equations. Since Ginzburg-Landau model for superconductors is identical with Abelian-Higgs model in cosmology, their simulation results can be interpreted both as the evolution of vortex filaments and that of cosmic strings. [33]

IV.4. Time-dependent Ginzburg-Landau equations (TDGL)

Gor'kov(1959,1960) [34, 35] has derived the static Ginzburg-Landau equation based on his Green function formulation of the BCS theory. A. Schmid [36] has derived a set of time-dependent Ginzburg-Landau equations semi-phenomenologically. However, the microscopic derivation of the time-dependent Ginzburg-Landau equations is more difficult, mainly due to the singularity in the density of states at the gap

edge. Paramagnetic impurities are known to be pair breakers destroying the pairing of electrons since they destroy the symmetry of the system under time reversal. At a sufficiently high concentration of those paramagnetic impurities the energy spectrum of the superconductor becomes gapless. Gor'kov and Eliashberg [37] have made the first breakthrough to obtain a rigorous microscopic derivation of this set of time-dependent Ginzburg-Landau equations in the gapless regime.

From the TDGL equations, Schmid also derived a dissipation theorem:

$$\frac{dF}{dt} = -W - \text{div } \mathbf{J}_E, \quad (4.26)$$

where

$$W = \sigma \left[\frac{1}{c} \frac{\partial}{\partial t} \mathbf{A} + \nabla \tilde{\Phi} \right]^2 + \frac{2\gamma}{\hbar} \left| \left(\hbar \frac{\partial}{\partial t} - 2ie\tilde{\Phi} \right) \Psi \right|^2, \quad (4.27)$$

and

$$\mathbf{J}_E = \mathbf{S} - \mu \mathbf{j}/e - Re \frac{1}{m} \left[\left(\hbar \nabla - \frac{2ie}{c} \mathbf{A} \right) \Psi^* \right] \left[\left(\hbar \frac{\partial}{\partial t} - 2ie\tilde{\Phi} \right) \Psi \right] \quad (4.28)$$

Here σ is the normal conductivity, γ a diffusion constant, and e the electron charge. The symbol μ denotes the chemical potential and $\tilde{\Phi} = \Phi - \mu/e$ is called the electrochemical potential (Φ is the electric potential). Finally, $\mathbf{S} = \frac{c}{4\pi} \mathbf{E} \times \mathbf{H}$ is the Poynting vector. While \mathbf{J}_E is the current of energy, the positive definite W is the power dissipated in the irreversible process. Thus in the physical process described by the time-dependent Ginzburg-Landau (TDGL) equations there are always irreversible dissipations.

Since we are mostly interested in the steady-state of the superconductors, we want to simplify TDGL into a numerically easier form to solve. In the following chapters we derive our simplified TDGL by a relaxation approach. Into the process we do not take account the terms involving the electric potential Φ (the electrochemical potential $\tilde{\Phi}$), hence ignore the ohmic dissipation due to normal current in the Schmid's

dissipation theorem.

CHAPTER V

INTRODUCTION TO PART I: STEADY-STATE AND EQUILIBRIUM VORTEX CONFIGURATIONS, TRANSITIONS, AND EVOLUTION IN A MESOSCOPIC SUPERCONDUCTING CYLINDER

In this opening chapter of Part I, we present the result of a numerical study about the magnetization process inside a superconducting square cylinder, with sub-micron lateral dimension in an external magnetic field. This part has been published in Physical Review B. [3] We have restricted the work to a square cross section of a linear size equal to 4.65 times λ (the magnetic penetration depth). Taking λ at 500 Å, then the cross-sectional area is $0.054 \mu m^2$.

Previous works on the magnetization of a mesoscopic superconductor without pinning centers have been reported by Peeters *et al.* [19, 38, 39, 40] and others, [41, 42] who presented extensive calculations on the superconducting state in mesoscopic, type-I, superconducting thin films. In most cases they found transitions between giant vortex states of different circulation quantum numbers L , with some multi-vortex states occasionally appearing as thermodynamically stable states, but mostly as metastable states. These predictions appear to have already received some level of experimental confirmation, although some discrepancies still exist. [43] (Ref. [42] mainly compared the energy of a “3-2” vortex-antivortex molecule state with that of a single off-centered vortex state at $L = 1$, as both evolve to the equilibrium state of a single vortex at the center.) Misko et al. [44] studied both type-I and type-II mesoscopic triangular cylinders, and have shown that a vortex-antivortex molecule appears only if the sample is type-I. They considered only one field value at which $L = 2$ is favored, and did not consider vortex configurational transitions as the field

changes.¹

Our aim is to simulate how vortices enter and settle in stable arrangements when a mesoscopic type-II superconductor of a given symmetry is first cooled below the critical temperature, and then an external magnetic field is applied. This is often termed zero field cooling (ZFC). We find that only vortex numbers and configurations consistent with the sample symmetry can appear in this case. It is known that global minimum-energy vortex configurations exist with reduced symmetry, with corresponding final equilibrium states at general values of the applied field. To find these equilibrium states we developed an efficient numerical scheme.

Our approach is to solve a set of simplified (and discretized) TDGL equations, in which the coupling to the electric field is neglected, and the superconducting order parameter and the magnetic field are assumed to relax with the same time scale. These assumptions are not physical, but are acceptable here, since we are only interested in obtaining the final steady-state vortex configurations, and the symmetry-related qualitative behavior of the transient configurations and their evolution. For a more physical set of TDGL equations see Tinkham. [25] For an example of the numerical solution of such a set of TDGL equations, see. [45]

Our numerical method may be understood to be a relaxation procedure with a pseudo time. [33, 46] Since the equations we have solved do not contain any thermal fluctuation terms, and the sample we considered has a perfect square symmetry, we find that when starting with the Meissner state and no field penetration, then the final steady-state vortex configurations we obtain all have perfect square symmetry, with vortex numbers also limited to only multiples of four (the symmetry number).

¹In this brief survey of literature, we have not included solutions of linearized GL equations to study the vortex configurations near the phase boundary, studies of vortex configurations in the presence of pinning center(s), and studies based on the London approximation.

These configurations would correspond to physical situations under zero-field cooling, if the physical sample has perfect symmetry, and the temperature is sufficiently low, so that thermal fluctuations are not able to overcome any energy barrier for vortex entry, expulsion, or rearrangement. If the sample surface has slight imperfection, or if the temperature is not sufficiently low, then these configurations are, in most cases, not in equilibrium at the given magnetic field strength. Even the vortex number may not be correct; however, if we insert terms to simulate thermal fluctuation into the equations, as in the method of simulated annealing, [47, 48] then the simulation computer program will take a much longer time to run, and may become impractical even with a supercomputer.

We have devised an efficient scheme to find the equilibrium vortex configurations: We solve the same set of relaxation equations without any thermal fluctuation terms, but instead of starting the solution with the Meissner state as the initial state, we devise artificial initial states with a given number of vortices in random positions. We present analytic expressions for such initial states in terms of a widely known approximate expression for a singly-quantized vortex in cylindrical coordinates. Then, for vortex numbers not too different from the equilibrium number, the final steady states obtained by solving our relaxation equations will, in most cases, have the number of vortices close to those of the initial states. By comparing the total Gibbs energies of these steady states with different vortex numbers we can find the state with the lowest total Gibbs energy, which we identify as the equilibrium state with the equilibrium vortex number. Sometimes we obtain more than one configuration for the same vortex number (when the vortex number exceeds four), then their Gibbs energies are also compared. We give an explicit demonstration of this scheme,² that might

²For a larger sample in a sufficiently large magnetic field, we can occasionally obtain configurations with a reduced symmetry when solving the equations starting

be very useful in view of the recent interest in nanoscience and nanotechnology.³ We note that in a bulk sample vortices like to form a triangular lattice. Thus, when the sample does not conform with this symmetry, and if the sample is sufficiently small so that the boundary effect on the equilibrium vortex configurations is important, then the system is frustrated,⁴ and the equilibrium vortex configurations can be quite intriguing and difficult to foresee.

V.1. Abrikosov vortex theory

Abrikosov [9] discovered that if the κ parameter, now known as the Ginzburg-Landau parameter, is larger than $1/\sqrt{2}$, then when a bulk superconductor is placed in a sufficiently large magnetic field, the magnetic field penetrates the superconductor in the form of singly-quantized vortices. Around each vortex flows a supercurrent, [9] confining a single quantum of magnetic flux within it.

Abrikosov's work which is of interest here is summarized with the order parameter function Ψ and a parameter β_A defined in terms of the order parameter shown in the following equations.

$$\Psi = \sum_{n=-\infty}^{\infty} C_n e^{ikny} \psi_n(x), \quad (5.1)$$

with the uniform superconducting state, but this is very rare, and very difficult to control. We think that this is because the numerical program does not observe the perfect square symmetry, but this violation of symmetry is a weak one. This way to get an asymmetric steady state is not reliable, so we do not recommend its use to find any asymmetric equilibrium state.

³As far as we know, previous approaches used random initial conditions with no control of L , so the magnetic field must be changed in very small steps to obtain speedy convergence. If so, the present scheme represents an important improvement, which allows direct implementation at any applied field. Note that the scheme also applies to the situation when a given distribution of pinning centers exist in the system or on its surface.

⁴Here "frustration" refers to the fact that the presence of the boundary frustrates the desire of the system to minimize its energy in the triangular lattice.

where

$$\psi_n(x) = \exp \left[-\frac{\kappa^2}{2} \left(x - \frac{kn}{\kappa^2} \right)^2 \right], \quad (5.2)$$

and

$$\beta_A \equiv \frac{|\overline{\Psi}|^4}{(|\overline{\Psi}|^2)^2}. \quad (5.3)$$

The order parameter function is a solution to linearized Ginzburg-Landau equation in the vicinity of the critical point (where $|\Psi| \ll 1$). In a bulk superconductor filling the space this must be a periodic array of vortices. In a bulk superconductor (a long cylinder) subject to an external magnetic field $H = \text{const} = H_0$ near H_{c2} , with a gauge $A = H_0 x$ chosen, Abrikosov showed that the Ginzburg-Landau equation reduces to an oscillator type of equation

$$d^2\Psi/dx^2 - \kappa^2(1 - H_0^2 x^2)\Psi(x) = 0, \quad (5.4)$$

which has the vortex solutions (5.1) and (5.3). It is observed from the this equation that the parameter β_A is a purely geometric parameter. Since the free energy takes its minimum at the lowest value of β_A , Abrikosov could determine the coefficients C_n for the minimum-energy solution by calculating β_A . For a triangular lattice ($iC_{2n+1} = C_{2n} = \text{const}$) $\beta_A = 1.16$, while $\beta_A = 1.18$ for a square lattice ($C_{n+1} = C_n = \text{const}$). Once β_A is determined, all the thermodynamic properties can be calculated subsequently. Therefore in a bulk superconductor there is a triangular lattice of vortices. Figure 34 in Appendix A is two-dimensional simulation of mesoscopic cylinder subject to periodic boundary condition. As the sample area gets sufficiently large for the vortices penetrated, the vortices arrange themselves in an arrangement close to triangular lattice.

CHAPTER VI

THE SIMPLIFIED TIME-DEPENDENT GINZBURG-LANDAU EQUATION

In an external magnetic field \mathbf{H} , the Gibbs free energy density g of a superconducting state is given by [25]:

$$g = f_n + \alpha|\Psi|^2 + \frac{\beta}{2}|\Psi|^4 + \frac{1}{2m_s} \left| \left(-i\hbar\nabla - \frac{e_s}{c}\mathbf{A} \right) \Psi \right|^2 + \frac{|\mathbf{h}|^2}{8\pi} - \frac{\mathbf{h} \cdot \mathbf{H}}{4\pi} \quad (6.1)$$

Here, f_n is the free energy density in the normal state in the absence of the magnetic field; Ψ is the complex-valued order parameter, with the superscript * denoting complex conjugation; \mathbf{A} the magnetic vector potential, $\mathbf{h} = \nabla \times \mathbf{A}$ the induced magnetic field, and \mathbf{H} the applied magnetic field. Then the supercurrent density is expressed as

$$\mathbf{j}_s = \frac{c}{4\pi} \nabla \times \nabla \times \mathbf{A} = \frac{e_s \hbar}{2im_s} (\Psi^* \nabla \Psi - \Psi \nabla \Psi^*) - \frac{e_s^2}{m_s c} |\Psi|^2 \mathbf{A}. \quad (6.2)$$

The physical parameters are as follows: e_s is the “effective charge” of a Cooper pair which is twice the charge of an electron, and m_s its “effective mass” which can be selected arbitrarily, but the conventional choice is twice the mass of an electron. Also, c is the speed of light, and $\hbar = h/2\pi$ where h is Planck’s constant.

Ginzburg-Landau theory postulates that the Gibbs free energy, G , of a superconducting sample Ω is at a minimum in the superconducting state. The celebrated Ginzburg-Landau equations are obtained by minimizing this functional with respect to Ψ and \mathbf{A} using the variational principle.

Since a constant term does not change the end result of the variational technique, an algebraic manipulation is made to subtract f_n and add $\mathbf{H} \cdot \mathbf{H}/8\pi$ to the g above,

giving: [49]

$$G(\Psi, \mathbf{A}) = \int_{\Omega} \left(\alpha |\Psi|^2 + \frac{\beta}{2} |\Psi|^4 + \frac{|\mathbf{h} - \mathbf{H}|^2}{8\pi} + \frac{1}{2m_s} \left| \left(-i\hbar\nabla - \frac{e_s}{c} \mathbf{A} \right) \Psi \right|^2 \right) d\Omega \quad (6.3)$$

We introduce dimensionless variables as follows:

$$x' = \frac{x}{\lambda}, \quad \mathbf{h}' = \frac{\mathbf{h}}{\sqrt{2}H_c}, \quad \Psi' = \frac{\Psi}{\Psi_0}. \quad (6.4)$$

The other variables are subsequently nondimensionalized as

$$\mathbf{H}' = \frac{\mathbf{H}}{\sqrt{2}H_c}, \quad \mathbf{j}' = \frac{2\sqrt{2}\pi\lambda}{cH_c} \mathbf{j}, \quad \mathbf{A}' = \frac{\mathbf{A}}{\sqrt{2}H_c\lambda}. \quad (6.5)$$

The characteristic scales are: $|\Psi_0| = \sqrt{-\alpha/\beta}$, which is the magnitude of Ψ that minimizes the free energy in the absence of a field; the thermodynamic critical field strength $H_c = \left(4\pi|\alpha||\Psi_0|^2\right)^{1/2}$, which divides the normal state and superconducting state regions in Type-I superconductor phase diagram; the London penetration depth $\lambda = \left(\frac{m_s c^2}{4\pi|\Psi_0|^2 e_s^2}\right)^{1/2}$; the coherence length $\xi = \left(\frac{\hbar^2}{2m_s|\alpha|}\right)^{1/2}$; and, the Ginzburg-Landau parameter $\kappa = \lambda/\xi$.

We obtain the dimensionless gauge-invariant free energy functional, omitting primes for convenience.

$$G(\Psi, \mathbf{A}) = \int_{\Omega} \left(-|\Psi|^2 + \frac{1}{2} |\Psi|^4 + |\nabla \times \mathbf{A} - \mathbf{H}|^2 + \left| \left(\frac{\nabla}{\kappa} - i\mathbf{A} \right) \Psi \right|^2 \right) d\Omega \quad (6.6)$$

The simplified TDGL model we employ to find solutions of the static GL equations may be viewed as a gradient flow of the energy functional. That is, the variation of (Ψ, \mathbf{A}) w.r.t. time should be in the opposite direction of the gradient of the energy functional, $\frac{\partial \Psi}{\partial t} = -\frac{\delta G}{\delta \Psi^*}$, $\frac{\partial \mathbf{A}}{\partial t} = -\frac{1}{2} \frac{\delta G}{\delta \mathbf{A}}$ with time, t , in units of the only relaxation time

of the equations.

This corresponds to the so-called *Relaxation Method* to solve a partial differential equation of an elliptic type, or a boundary value problem (BVP). [47, 50] In this method a solution u to an equation of a form $\frac{\partial u}{\partial t} = \mathcal{L}u - \rho$ relaxes to an equilibrium solution u_∞ as $\frac{\partial u}{\partial t} \rightarrow 0$ as $t \rightarrow \infty$. u_∞ is a solution to an equation $\mathcal{L}u = \rho$, which is of our true interest. (Here \mathcal{L} is a symbolic notation for differential operators and ρ denotes a source term.) Usually a reasonably guessed initial condition leads to a solution.

The time-dependent Ginzburg-Landau equation describes a relaxation process to find the state of minimum energy, as can be seen in the various energy transfer terms in Schmid's dissipation theorem (4.26). We can reach the same steady-state by solving this simplified TDGL. The difference is, by eliminating the electric potential in the original TDGL, we are ignoring the electric fields and ohmic dissipation by normal currents in superconductors. By using relaxation method we do not have to worry about the initial condition too much, at the same time, the transient solutions from our simplified TDGL give qualitative information about the actual physical relaxation process.

The natural boundary conditions are given as follows.

$$(\nabla \times \mathbf{A}) \times \mathbf{n} = \mathbf{H} \times \mathbf{n}, \quad (6.7)$$

which is the continuity of the parallel component of the magnetic field across the boundary surface, and

$$\left(\frac{\nabla}{\kappa} - i\mathbf{A}\right) \Psi \cdot \mathbf{n} = 0, \quad (6.8)$$

which is the vanishing gauge-invariant normal derivative of Ψ with \mathbf{n} denoting the outward surface normal. [51]

VI.1. Discretization and calculation procedure

For long square cylindrical samples, we need only solve a 2-D problem. We take

$$\mathbf{A} = (A(x, y), B(x, y), 0) \text{ and } \mathbf{H} = (0, 0, H) \text{ where } H = (\nabla \times \mathbf{A})_z = \frac{\partial B}{\partial x} - \frac{\partial A}{\partial y}.$$

Defining the link variables ¹ as

$$W(x, y) = \exp\left(i\kappa \int^x A(\zeta, y) d\zeta\right), \quad (6.9)$$

and

$$V(x, y) = \exp\left(i\kappa \int^y B(x, \eta) d\eta\right), \quad (6.10)$$

the gauge invariance is preserved in discretizing the Gibbs free energy and the consequent simplified-TDGL equations. Noting that

$$|\partial_x (W^* \Psi)| = |(\partial_x - i\kappa A) \Psi|, \quad (6.11)$$

and

$$|\partial_y (V^* \Psi)| = |(\partial_y - i\kappa B) \Psi|, \quad (6.12)$$

we have

$$\begin{aligned} G(\Psi, \mathbf{A}) = & \int_{\Omega} \left(-|\Psi|^2 + \frac{1}{2}|\Psi|^4 + |\nabla \times \mathbf{A} - \mathbf{H}|^2 \right. \\ & \left. + \left| \frac{1}{\kappa} \partial_x (W^* \Psi) \right|^2 + \left| \frac{1}{\kappa} \partial_y (V^* \Psi) \right|^2 \right) d\Omega. \end{aligned} \quad (6.13)$$

We discretize the free energy functional on a staggered grid over Ω shown in Fig.5. [46, 52] This gives us a second-order approximation in h_x and h_y to the con-

¹The path-ordered product of these link variables (via the path-ordered integral of the continuum gauge field \mathbf{A} along the lattice) can be interpreted as the “parallel transporter” along the link. That is, $e^{i\kappa \int_x^{x+\mu} A(\zeta, y) d\zeta}$, for example, transports vectors under gauge group at x to vectors at $x + \mu$ along the link from x to $x + \mu$. It is also known that this link variable method leads to smaller discretization errors in the action integral. [30]

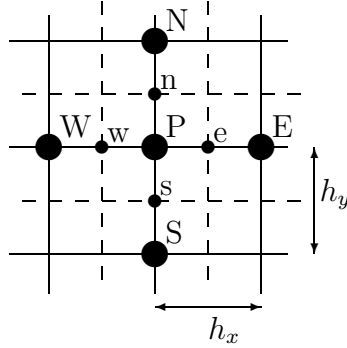


Fig. 5. The staggered grid arrangement for cell nodes P,E,W,N,S and faces e,w,n,s.

tinuous energy functional, where the h_x and h_y are the spatial increments in the x- and y-direction. The staggered grid also leads to a satisfactory way of discretizing the natural boundary conditions. [53] For a rectangular grid, the first component of the vector potential is constant in time on one pair of the edges of the boundary, and the second component is constant in time on the other pair, which is derived below.

In this paper, we assume that the cylindrical superconductor has a square cross-section and is subject to an applied field along the central axis. The applied field is assumed to be constant in time. We further assume the order parameter Ψ varies in the cross-sectional plane of the square cylindrical sample, and the vector potential \mathbf{A} has only two nonzero components (A, B) , which also lie in this plane. We also assume that the superconductor has no pinning sites. Then at steady-state conditions, the vortices settle at maximal distances due to mutual repulsion. This requirement leads to a triangular lattice of vortices in an infinitely large domain. [25]

In the staggered grid the lattice evaluation points for Ψ , A , and B are all different, with Ψ evaluated at the node center (i,j) , A evaluated at the east cell face $(i+1/2, j)$, and B evaluated at the north cell face $(i,j+1/2)$. According to Refs. [52, 46], this

formulation keeps second order accuracy in the derivative evaluations as they appear in each of the discretized equations.

The discrete equations are obtained by minimizing the discrete energy functional G_d with respect to the variation in Ψ and \mathbf{A} as:

$$\frac{\partial \Psi_P}{\partial t} = \frac{h_x h_y}{\kappa^2} \left(\frac{e^{\iota A_w \kappa h_x} \Psi_W - 2\Psi_P + e^{-\iota A_e \kappa h_x} \Psi_E}{h_x^2} + \frac{e^{\iota B_s \kappa h_y} \Psi_S - 2\Psi_P + e^{-\iota B_n \kappa h_y} \Psi_N}{h_y^2} \right) + h_x h_y N_1(\Psi_P) \quad (6.14)$$

$$(6.15)$$

$$\frac{\partial A_e}{\partial t} = -h_x \left(\frac{B_{nE} - B_n + B_s - B_{sE}}{h_x} - \frac{A_{Ne} - 2A_e + A_{Se}}{h_y} \right) + \frac{h_y}{\kappa} N_2(A_e, \Psi_P, \Psi_E) \quad (6.16)$$

$$(6.17)$$

$$\frac{\partial B_n}{\partial t} = -h_y \left(\frac{A_w - A_e + A_{Ne} - A_{Nw}}{h_y} - \frac{B_{nE} - 2B_n + B_{nW}}{h_x} \right) + \frac{h_x}{\kappa} N_3(B_n, \Psi_P, \Psi_N) \quad (6.18)$$

with

$$N_1(\Psi_P) = (1 - |\Psi_P|^2) \Psi_P \quad (6.19)$$

$$N_2(A_e, \Psi_P, \Psi_E) = (\Phi_P \Theta_E - \Theta_P \Phi_E) \cos(A_e \kappa h_x) - (\Phi_P \Phi_E + \Theta_P \Theta_E) \sin(A_e \kappa h_x) \quad (6.20)$$

$$N_3(B_n, \Psi_P, \Psi_N) = (\Phi_P \Theta_N - \Theta_P \Phi_N) \cos(B_n \kappa h_y) - (\Phi_P \Phi_N + \Theta_P \Theta_N) \sin(B_n \kappa h_y) \quad (6.21)$$

where Θ and Φ are the real and imaginary parts of Ψ , i.e. $\Psi = \Phi + i\Theta$. The boundary conditions for Ψ are obtained by integrating (6.8) at the boundary in the normal direction:

$$\Psi_P = \Psi_S e^{\iota \kappa h_y B_s}, \quad \text{on } \Omega_T \quad (6.22)$$

$$\Psi_P = \Psi_N e^{-\iota \kappa h_y B_n}, \quad \text{on } \Omega_B \quad (6.23)$$

$$\Psi_P = \Psi_E e^{-i\kappa h_x A_e}, \quad \text{on } \Omega_L \quad (6.24)$$

$$\Psi_P = \Psi_W e^{i\kappa h_x A_w}, \quad \text{on } \Omega_R \quad (6.25)$$

Here T , B , L , and R denote top, bottom, left, and right of the computational domain Ω , respectively. The boundary condition (6.7) can be written on the staggered grid as:

$$A_e = A_{Se} - \left(H - \frac{B_{nE} - B_n}{h_x} \right) h_y \quad \text{on } \Omega_T \quad (6.26)$$

$$A_e = A_{Ne} + \left(H - \frac{B_{nE} - B_n}{h_x} \right) h_y \quad \text{on } \Omega_B \quad (6.27)$$

$$B_n = B_{nE} - \left(H + \frac{A_{Ne} - A_e}{h_y} \right) h_x \quad \text{on } \Omega_L \quad (6.28)$$

$$B_n = B_{nW} + \left(H + \frac{A_{Ne} - A_e}{h_y} \right) h_x \quad \text{on } \Omega_R \quad (6.29)$$

Here we derive an additional set of boundary conditions for \mathbf{A} . From (6.25) we have

$$\Phi_P = \Phi_E \cos(A_e \kappa h_x) + \Theta_E \sin(A_e \kappa h_x) \quad (6.30)$$

$$\Theta_P = \Theta_E \cos(A_e \kappa h_x) - \Phi_E \sin(A_e \kappa h_x) \quad (6.31)$$

Using the results we can derive

$$\Phi_P \Theta_E - \Theta_P \Phi_E = (\Phi_E^2 + \Theta_E^2) \sin(A_e \kappa h_x) \quad (6.32)$$

$$\Phi_P \Phi_E + \Theta_P \Theta_E = (\Phi_E^2 + \Theta_E^2) \cos(A_e \kappa h_x) \quad (6.33)$$

This makes $N_2(A_e, \Psi_P, \Psi_E) = 0$ on Ω_L . On the other hand, looking at the boundary conditions (6.27)-(6.29), we have $H = \partial B / \partial x - \partial A / \partial y = \text{const}$ on boundaries. Therefore the equation (6.17) becomes $\partial A_e / \partial t = 0$ on Ω_L . Thus we have $A_e(t) = A_e(0)$ for all $t > 0$ on Ω_L , which gives us a supplementary boundary condition. The other supplementary boundary conditions, $A_e(t) = A_e(0)$ for all $t > 0$ on Ω_R and

$B_n(t) = B_n(0)$ for all $t > 0$ on Ω_B and Ω_T are derived similarly. [51]

The finite difference equations are solved by the Forward Euler method with $h_x = h_y = 0.15$ and $\Delta t = 0.05$, and taking $\kappa = 4$. In the numerical computations that follow, the all details are kept the same except for the strength of the applied magnetic field and/or the initial conditions.

VI.2. Stability of the numerical scheme

In this section we will derive necessary and sufficient conditions under which the numerical solution to the Ginzburg-Landau equation converge to the exact solution as the mesh is refined. [54] The problem of convergence is reduced to that of consistency and stability by Lax equivalence theorem.

A system of algebraic equations generated by the discretization process is called finite difference equations (FDEs). A finite difference equation is said to be *consistent* with the original partial differential equation (PDE) if the difference between the PDE and its FDE vanishes as the mesh is refined, i.e. $\lim_{\Delta t, \Delta x, \Delta y \rightarrow 0} (PDE - FDE) = 0$. The forward Euler method applied to TDGL yields the truncation error (TE)

$$TE(i, j, k) \equiv TE(ih_x, jh_y, k\Delta t) = O(\Delta t) + O(\Delta x^2, \Delta y^2). \quad (6.34)$$

Therefore, $\lim_{\Delta t, \Delta x, \Delta y \rightarrow 0} (TE) = 0$ and Forward Euler is consistent with TDGL.

A numerical scheme is said to be *stable* if errors from any source (round-off, truncation, mistakes) do not grow, but decay or remain negligible as the calculation proceeds.

The theorem due to Lax [55] is repeated here without proof.

Lax Equivalence Theorem: Given a properly posed initial-value problem and a finite-difference approximation to it that satisfies the consistency condition, stability

is a necessary and sufficient condition for convergence.

There is no general method of analysis for the stability of nonlinear problems. A common approach is to linearize the nonlinear problem and assume that the stability of linear problems applies locally. However, here we take a little different approach. We give the linear part of TDGL a rigorous analysis and treat the nonlinear term as perturbation. In the analysis in the following sections we need the following theorem by Kreiss. [55]

Theorem. If the difference scheme

$$U^{(n+1)} = C(\Delta t)U^{(n)} \quad (6.35)$$

is stable, and $Q(\Delta t)$ is a bounded family of operators, then the difference system

$$U^{(n+1)} = [C(\Delta t) + \Delta t Q(\Delta t)]U^{(n)} \quad (6.36)$$

is also stable.

Above theorem states that the stability is not destroyed by a small perturbation. Also the well-known theorem of Gerschgorin [56] will be frequently used:

Gerschgorin's Circle Theorem: Every eigenvalue of a matrix $A = [a_{ij}]$ lies in at least one of the circles C_1, \dots, C_n , where C_i has its center at the diagonal entry a_{ii} and its radius $r_i = \sum_{j \neq i} |a_{ij}|$ equal to the absolute sum along the rest of the row.

VI.2.1. Matrix method

From eqs. (6.19) - (6.21) we define an operator $N : C \times R^2 \rightarrow C \times R^2$ for $U = (\Psi, A, B)$

$$N(U) = [N_1(\Psi), N_2(A, \Psi), N_3(B, \Psi)]^T \quad (6.37)$$

with the norm

$$\|N(U)\| = \|N_1(\Psi)\|_2 + \|N_2(A, \Psi)\|_2 + \|N_3(B, \Psi)\|_2. \quad (6.38)$$

Then it is easy to show that there exists a nonnegative constant c such that

$$\|N(U(t))\| < c \text{ for all } t \geq 0. \quad (6.39)$$

The Forward Euler applied to TDGL yields the following difference scheme (see eq. (6.15) - 6.18)

$$U^{(n+1)} = [1 + \Delta t(L + N)]U^{(n)} = [C + \Delta tN]U^{(n)} \quad (6.40)$$

By the Kreiss theorem we can reduce the stability problem for a nonlinear FDE (6.40) to that of a linear FDE,

$$\tilde{U}^{(n+1)} = C\tilde{U}^{(n)} = (1 + \Delta tL)\tilde{U}^{(n)} \quad (6.41)$$

For convenience we drop the tilde signs in (6.41). Then the first equation in (6.41) can be written as

$$\begin{aligned} \Psi_P^{(n+1)} &= \left(1 - \frac{2\Delta t}{\kappa^2} \left(\frac{h_y}{h_x} + \frac{h_x}{h_y}\right)\right) \Psi_P^{(n)} \\ &+ \frac{\Delta t}{\kappa^2} \frac{h_y}{h_x} (W_w \Psi_W + W_e^* \Psi_E)^{(n)} + \frac{\Delta t}{\kappa^2} \frac{h_x}{h_y} (V_s \Psi_S + V_n^* \Psi_N)^{(n)} \\ &= C(\Delta t, A, B) \Psi^{(n)}, \end{aligned} \quad (6.42)$$

where the matrix $C(\Delta t, A, B)$ can be written as

$$C(\Delta t, A, B) = \begin{pmatrix} D_1 & F_1 & & & \\ E_1 & D_2 & F_2 & & \\ & \cdot & \cdot & \cdot & \\ & & E_{N_x-2} & D_{N_x-1} & F_{N_x-1} \\ & & & E_{N_x-1} & D_{N_x} \end{pmatrix} \quad (6.43)$$

where the block matrices of the dimension $N_x \times N_y$ have the following form

$$D_i = \begin{pmatrix} d & \overline{W}_{ij}^* & & & \\ \overline{W}_{i-1,j} & d & & & \\ & & \cdot & \cdot & \cdot \\ & & & \overline{W}_{i+N_x-2,j+N_y-2} & d \end{pmatrix} \quad (6.44)$$

$$E_i(\Delta t, V) = \begin{pmatrix} \overline{V}_{i,j-1} & & & & \\ & \ddots & & & \\ & & & & \\ & & & \overline{V}_{i+N_x-1,j+N_y-2} & \end{pmatrix} \quad (6.45)$$

and

$$F_i(\Delta t, V) = \begin{pmatrix} \overline{V}_{i,j}^* & & & & \\ & \ddots & & & \\ & & & & \\ & & & \overline{V}_{i+N_x-1,j+N_y-1}^* & \end{pmatrix} \quad (6.46)$$

where,

$$d = 1 - \frac{2\Delta t}{\kappa^2} \left(\frac{h_y}{h_x} + \frac{h_x}{h_y} \right), \quad (6.47)$$

$$\overline{W}_{ij} = \frac{\Delta t}{\kappa^2} \frac{h_y}{h_x} W_{ij}, \quad (6.48)$$

$$\overline{V}_{ij} = \frac{\Delta t}{\kappa^2} \frac{h_x}{h_y} V_{ij}. \quad (6.49)$$

Then by Gerschgorin's theorem, the eigenvalues λ_i of $C(\Delta t, A, B)$ will satisfy the

inequality

$$|\lambda_i - d| \leq r_i \quad (6.50)$$

where

$$r_i = \frac{\Delta t}{\kappa^2} \begin{cases} \frac{h_y}{h_x} + \frac{h_x}{h_y}, \text{ if } i = 1, i = N_x, i = (N_x - 1) \times N_y + 1, i = N_x \times N_y \\ 2\frac{h_y}{h_x} + \frac{h_x}{h_y}, \text{ if } i = 2, \dots, N_x - 1; i = (N_x - 1) \times N_y + 2, \dots, N_x \times N_y - 1 \\ \frac{h_y}{h_x} + 2\frac{h_x}{h_y}, \text{ if } i = mN_x + 1, i = mN_x + N_x, i = 1, \dots, N_x - 2 \\ 2\left(\frac{h_y}{h_x} + \frac{h_x}{h_y}\right), \text{ if } i = mN_x + 2, i = mN_x + N_x - 1, i = 1, \dots, N_x - 2 \end{cases}$$

Then we have

$$|\lambda_i| \leq |d| + r_{max}, \quad 1 \leq i \leq N_x \times N_y \quad (6.51)$$

where

$$r_{max} = \max r_i, \quad i = 1, \dots, N_x \times N_y \quad (6.52)$$

For stability, we require that

$$|\lambda_i| \leq |d| + r_{max} \leq 1, \quad \forall i \quad (6.53)$$

The inequality above will hold if

$$d = 1 - \frac{2\Delta t}{\kappa^2} \left(\frac{h_y}{h_x} + \frac{h_x}{h_y} \right) \geq 0 \quad (6.54)$$

i.e., the difference scheme (6.41) is stable provided that

$$\Delta t \leq \frac{\kappa^2}{2\left(\frac{h_y}{h_x} + \frac{h_x}{h_y}\right)}. \quad (6.55)$$

VI.2.2. Von Neumann's method

Since the equations for the vector potential form a linear system with constant coefficients, it is appropriate to apply von Neumann method. The equations (6.17) and

(6.18) can be written as

$$\frac{A_e^{(n+1)} - A_e^{(n)}}{\Delta t} = \left[(B_n - B_{nE} + B_{sE} - B_s) + \frac{h_x}{h_y} (A_{eN} - 2A_e + A_{eS}) \right]^{(n)} \quad (6.56)$$

$$\frac{B_n^{(n+1)} - B_n^{(n)}}{\Delta t} = \left[(A_e - A_w + A_{wN} - A_{eN}) + \frac{h_y}{h_x} (B_{nE} - 2B_n + B_{nW}) \right]^{(n)} \quad (6.57)$$

We now consider the following basis for the $N_x \times N_y$ dimensional space to which the error at any fixed time belongs

$$\mathcal{B} = \left\{ e^{I lx_i + I m y_j}, i = 0, \dots, N_x, j = 0, \dots, N_y \right\} \quad (6.58)$$

for $l = 1, \dots, N_x, m = 1, \dots, N_y$ where $I = \sqrt{-1}$.

Let the exact solution of the *finite difference equations* above as S_e . This the solution of the FDEs to be obtained using a computer with infinite accuracy. If we denote by S_n the numerical solution of the FDEs with a real computer with finite accuracy, the round-off error can be defined as $S_n = S_e + \varepsilon$ [57]. The error at (x_i, y_j, t_n) , where $t_n = n\Delta t$, can be expanded as a linear combination of the basis vectors:

$$\varepsilon_A(x_i, y_j, t_n) = \sum_{m=0}^{N_y} \sum_{l=0}^{N_x} a_{ml}(t_n) e^{I(lx_i + my_j)} \quad (6.59)$$

$$\varepsilon_B(x_i, y_j, t_n) = \sum_{m=0}^{N_y} \sum_{l=0}^{N_x} b_{ml}(t_n) e^{I(lx_i + my_j)} \quad (6.60)$$

Noting that $FDE = PDE - TE$, and we expand the truncation errors as

$$TE_A(x_i, y_j, t_n) = \sum_{m=0}^{N_y} \sum_{l=0}^{N_x} T_{ml}^A(t_n) e^{I(lx_i + my_j)} \quad (6.61)$$

$$TE_B(x_i, y_j, t_n) = \sum_{m=0}^{N_y} \sum_{l=0}^{N_x} T_{ml}^B(t_n) e^{I(lx_i + my_j)} \quad (6.62)$$

Combining all these yields the following system for the Fourier coefficients

$$\frac{a_{ml}(t_{n+1}) - a_{ml}(t_n)}{\Delta t} = (-1 + e^{-Imh_y}) (-1 + e^{Ilh_x}) b_{ml}(t_n)$$

$$+ \frac{h_x}{h_y} \left(-2 + e^{Imh_y} + e^{-Imh_y} \right) a_{ml}(t_n) - T_{ml}^A(t_n) \quad (6.63)$$

$$\begin{aligned} \frac{b_{ml}(t_{n+1}) - b_{ml}(t_n)}{\Delta t} &= \left(-1 + e^{-Ilh_x} \right) \left(-1 + e^{Imh_y} \right) a_{ml}(t_n) \\ &+ \frac{h_y}{h_x} \left(-2 + e^{Ilh_x} + e^{-Ilh_x} \right) b_{ml}(t_n) - T_{ml}^B(t_n) \end{aligned} \quad (6.64)$$

$$(6.65)$$

or in matrix form

$$E_{n+1} = G(\Delta t)E_n + C_n \quad (6.66)$$

where

$$E_n = \begin{pmatrix} a_{ml}(t_n) \\ b_{ml}(t_n) \end{pmatrix}, \quad (6.67)$$

and

$$G(\Delta t) = \begin{pmatrix} 1 - 4\Delta t \frac{h_x}{h_y} \sin^2 \left(\frac{1}{2} m h_y \right) & \Delta t \left(1 - e^{-Imh_y} \right) \left(1 - e^{Ilh_x} \right) \\ \Delta t \left(1 - e^{-Ilh_x} \right) \left(1 - e^{Imh_y} \right) & 1 - 4\Delta t \frac{h_y}{h_x} \sin^2 \left(\frac{1}{2} l h_x \right) \end{pmatrix} \quad (6.68)$$

and

$$C_n = - \begin{pmatrix} \Delta t T_{ml}^A(t_n) \\ \Delta t T_{ml}^B(t_n) \end{pmatrix}. \quad (6.69)$$

By means of the recursive relation (6.66), we have

$$E_{n+1} = GE_n + C_n$$

$$E_{n+1} = G[GE_{n-1} + C_{n-1}] + C_n = G^2E_{n-1} + GE_{n-1} + C_n$$

\vdots

$$E_{n+1} = G^{n+1}E_0 + G^n C_1 + G^{n-1} C_2 + \dots + C_n$$

thus we have

$$\|E_{n+1}\|_\infty \leq [\|G^n\|_\infty + \|G^{n-1}\|_\infty + \dots + \|I\|_\infty] \max[\|C_1\|_\infty, \dots, \|C_n\|_\infty],$$

where $E_0 = 0$, i.e. there is no error initially.

We seek conditions under which the powers of G are uniformly bounded. Since G

is a normal matrix, the necessary and sufficient condition for this would be to require that $\rho(G) < 1$. By Gerschgorin's theorem, the eigenvalues of G satisfy

$$|\lambda - g_{11}| \leq r_1, \quad (6.70)$$

or

$$|\lambda - g_{22}| \leq r_2, \quad (6.71)$$

where

$$r_1 = \left| \Delta t \left(1 - e^{-Imh_y} \right) \left(1 - e^{Ilh_x} \right) \right| \leq 4\Delta t \quad (6.72)$$

$$r_1 = \left| \Delta t \left(1 - e^{-Ilh_x} \right) \left(1 - e^{Imh_y} \right) \right| \leq 4\Delta t \quad (6.73)$$

By (6.70)

$$\left| \lambda - \left\{ 1 - 4\Delta t \frac{h_x}{h_y} \sin^2 \left(\frac{1}{2} m h_y \right) \right\} \right| \leq 4\Delta t \quad (6.74)$$

which implies that

$$\Delta t \leq \frac{1}{2 \left(1 + \frac{h_x}{h_y} \right)} \quad (6.75)$$

Similarly, from (6.71) we get

$$\Delta t \leq \frac{1}{2 \left(1 + \frac{h_y}{h_x} \right)} \quad (6.76)$$

These conditions satisfy

$$\|E_{n+1}\|_\infty \leq \text{Constant} \times \max[\|C_1\|_\infty, \dots, \|C_n\|_\infty]. \quad (6.77)$$

CHAPTER VII

MAGNETIC PENETRATION UNDER SYMMETRY

VII.1. Steady States under zero-field cooling in a perfectly square sample at low temperatures

We first solve the above set of equations assuming that the initial state is the perfect Meissner state with no field penetration. As explained in the introduction, this corresponds to applying a magnetic field after zero-field cooling. Fig. 6 shows plots of $|\Psi|^2$ (the left figure in (a) through (k)) and $h = \nabla \times \mathbf{A}$ (the right figure in (a) through (k)) for the final steady states reached for a sequence of increasing H values. In the left figures $|\Psi|^2$, which is interpreted physically as the density of Cooper pairs, runs from 0 to 1, with level 1 corresponding to the full superconducting state. Each isolated group of contours is called a “vortex,” representing the supercurrent \mathbf{J} circling around the vortex core, with $\Psi = 0$ at the vortex core. In the 3-D plots of Fig. 6 (b), it is clear that the vortices reach close to $|\Psi|^2 = 0$ at the core.

We note that the number of vortices increases in multiples of 4. This is a consequence of the fact that the vortices are symmetrically created at the mid-points of the sample edges. Perfect symmetry in the sample geometry dictates that each side creates an equal number of vortices. For sample sizes less than λ , it is to be expected that simultaneous penetration of four vortices is energetically unfavorable compared with a single vortex penetration. However, a single vortex entry is still prohibited if symmetry is strictly preserved. The magnetic field will simply penetrate the sample without entry of vortices in that case. When symmetry is not strictly preserved, and if the sample size is much smaller than λ , then no vortex will enter the sample since the magnetic field already penetrates the sample. If the sample size is of the

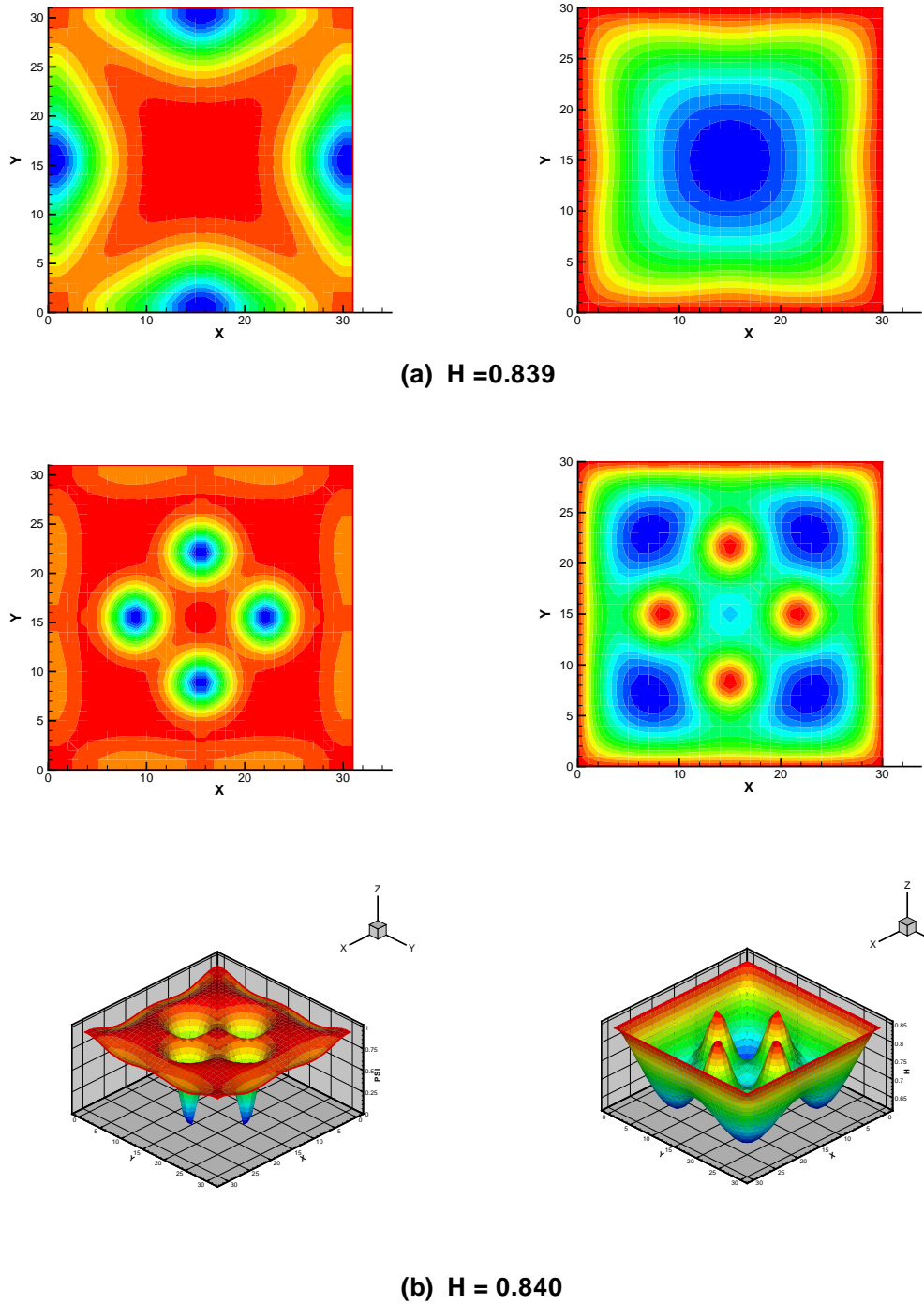
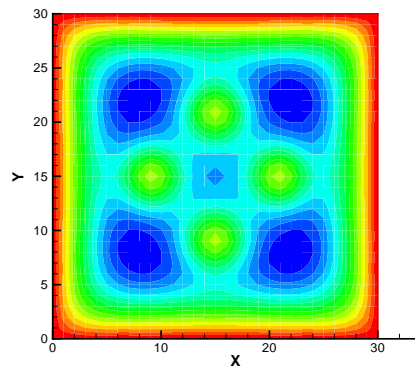
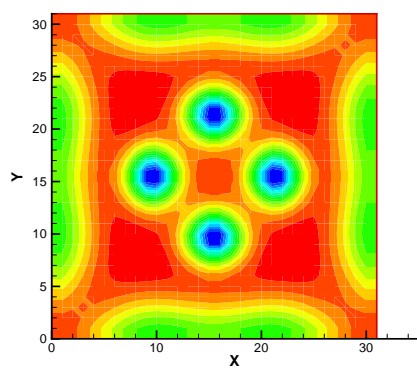
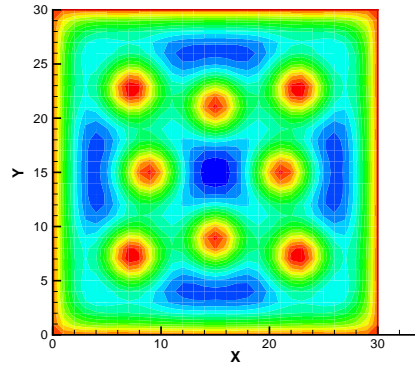
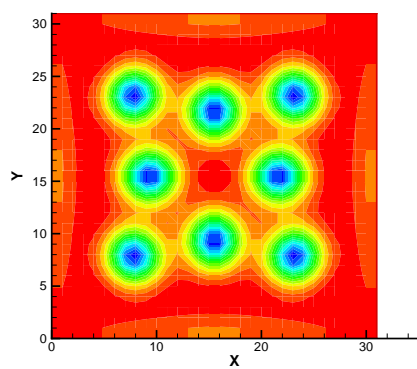


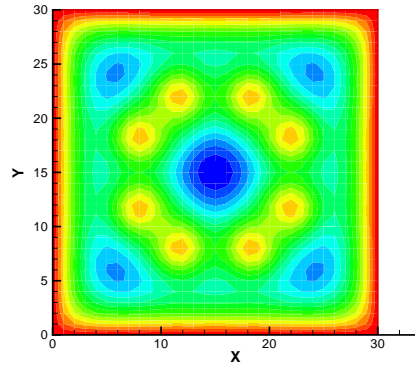
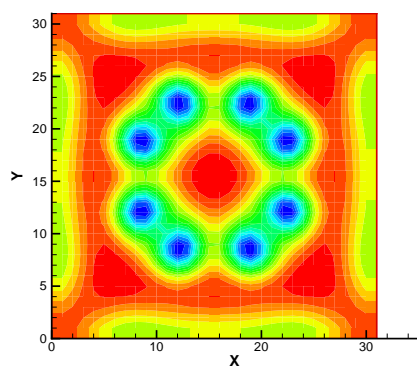
Fig. 6. Plots of $|\Psi|^2$ and $h = \nabla \times \mathbf{A}$ for various applied field H [$|\Psi|^2$ is shown on the left in (a) to (k), and h on the right in (a) to (k)]. These final steady-state solutions are obtained by a relaxation method from a uniform superconducting state.



(c) $H = 1.144$

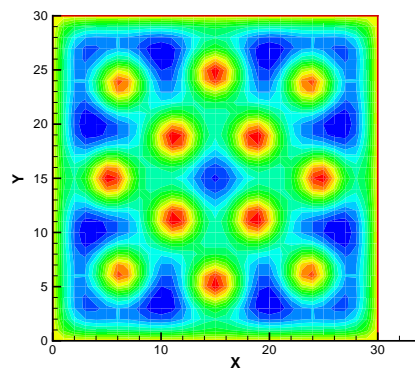
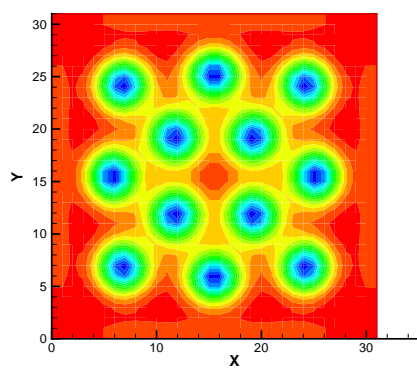


(d) $H = 1.145$

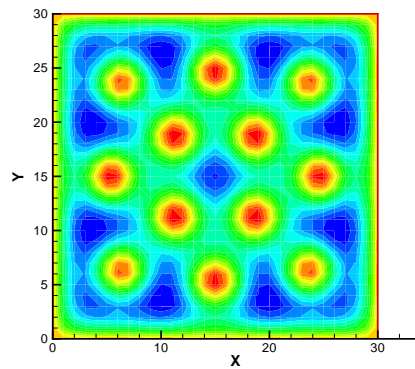
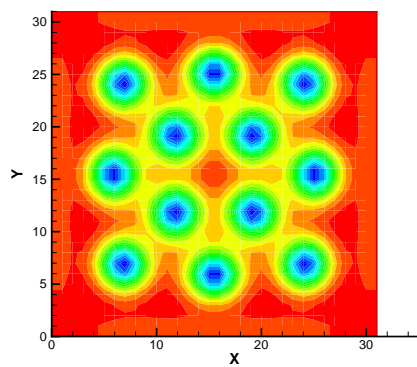


(e) $H = 1.429$

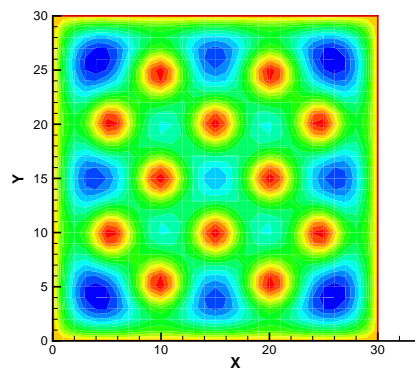
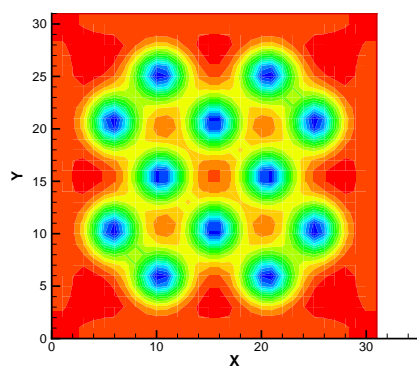
Fig. 6 (*cont.*)



(f) $H = 1.430$

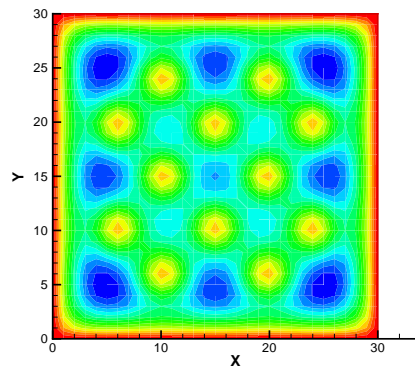
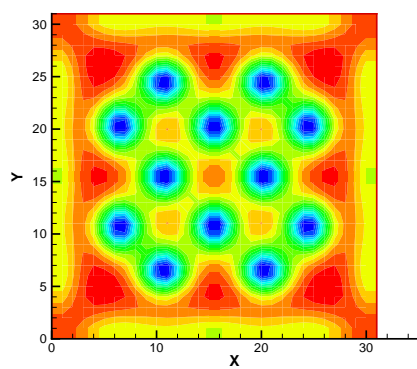


(g) $H = 1.454$

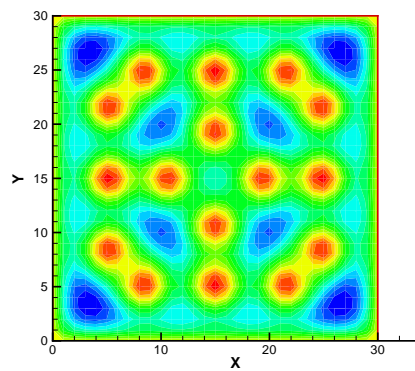
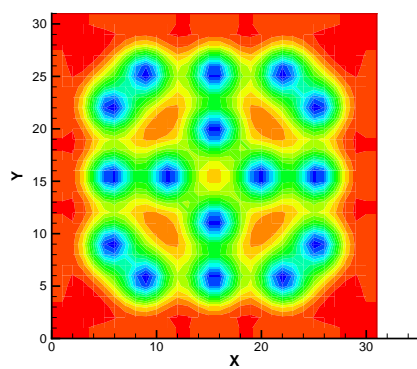


(h) $H = 1.455$

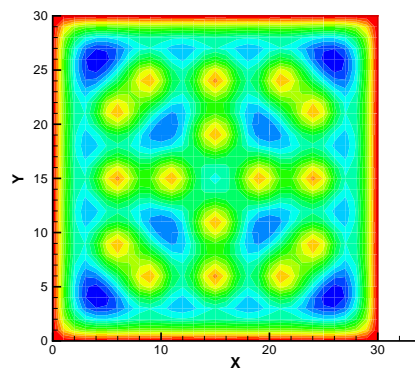
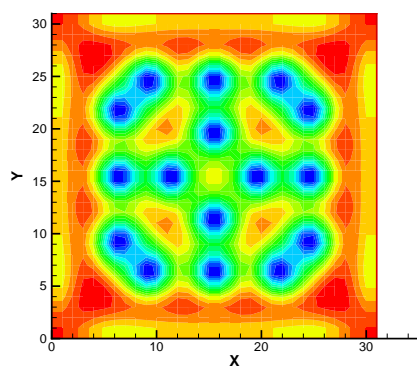
Fig. 6 (*cont.*)



(i) $H = 1.732$



(j) $H = 1.733$



(k) $H = 2.058$

Fig. 6 (*cont.*)

order of λ , then one vortex will enter and move to its center. In these calculations, symmetry is closely preserved, and in which case, vortices enter in multiples of 4 for a square cross-section. For a hexagonal cross-section, it should be a multiple of six. For a large circular cylinder, vortices of the usual kind (with line singularities) cannot enter. Rather, “cylindrical vortex sheets,” with phase-winding quantum number, n , about the axis, change from n at radial coordinate $\rho - \epsilon$, to $n + 1$ at $\rho + \epsilon$, and must be created at the boundary and then move radially inward. This is true only if symmetry is strictly preserved. However, this can only happen in an actual sample if the sample strictly obeys the symmetry, and the temperature is very close to absolute zero. Otherwise, vortices will enter one at a time via defect sites at the surface, or through thermal fluctuations to destroy the symmetry. Then it will not be a multiple of four for a square cross-section, or a multiple of six for a hexagonal cross-section, and the relationship between sample size and number of vortices becomes a less significant concern.

The symmetry here manifests itself in this geometry-dominated problem, and vortices arrange themselves in the square-symmetric configurations. The resultant steady states are mostly not true equilibrium states, since the vortex arrangements do not reflect the intrinsic tendency of vortices to form a triangular lattice known to appear in bulk samples. The natural next step is to add a thermal fluctuation term to find the true equilibrium states which may or may not conform with this symmetry. Such an approach would then be like simulated annealing. [47, 48] We believe it would not be practical to perfect this approach since it will likely be difficult to determine the appropriate rate of cooling and the starting temperature. In addition the runtime of the computer program might also be expected to be much longer than we have found here, so we have devised a different approach which we believe is much more efficient at finding the equilibrium states. This is given in a later section. We shall

Table I. The resultant number of vortices n_∞ and the induced magnetic field B for the applied magnetic field H .

n_∞	0	4	4	8	8	12	12	16	16
H	0.839	0.84	1.144	1.145	1.429	1.43	1.732	1.733	2.058
B	0.6163	0.7331	0.9779	1.0694	1.3022	1.3790	1.6288	1.6986	1.9719

see that even the cases with a low number of vortices are not the true equilibrium. Also of interest is the fact that for various H , the vortex configuration requires much longer run-times to get to a steady state. Geometry controls the settling time more than the energy in these cases.

Our results are summarized in Table I, which lists the range of H for each resultant number of vortices, and the corresponding induced magnetic field $B = \frac{1}{|\Omega|} \int_{\Omega} h d\Omega$. The table shows that the final number of vortices does not change within various bands of the applied magnetic field H . The H 's listed correspond to the threshold values (upper and lower limits) for each band. They were found on a trial-and-error basis, and can be refined to any desired accuracy. The table and Fig. 6 show that, below $H = 0.839$, there is no vortex. Between $H = 0.84$ and 1.144 , the vortex number $n_\infty = 4$, and so on.

The B vs H plot shown in Fig. 7, reveals that B is much lower than H when the number of vortices is small, but as the vortices increase, the curve approaches the $B = H$ curve asymptotically. The figure also shows an abrupt increase in B between the regions of different number of vortices. For example, when H changes from 1.144 to 1.145 , B changes from 0.9779 to 1.0694 . If the limit $\Delta H \rightarrow 0$ is

taken, we expect a sudden configurational phase transition increasing the number of vortices, as is apparent in Figs. 6 (c) and (d). Such mini-first-order transitions are known [19, 38, 39, 40, 41] to occur in a mesoscopic superconductor as H is changed, but the details are quite different, because different parameter (κ) regimes and sample geometries (cylinder vs. film) were studied.

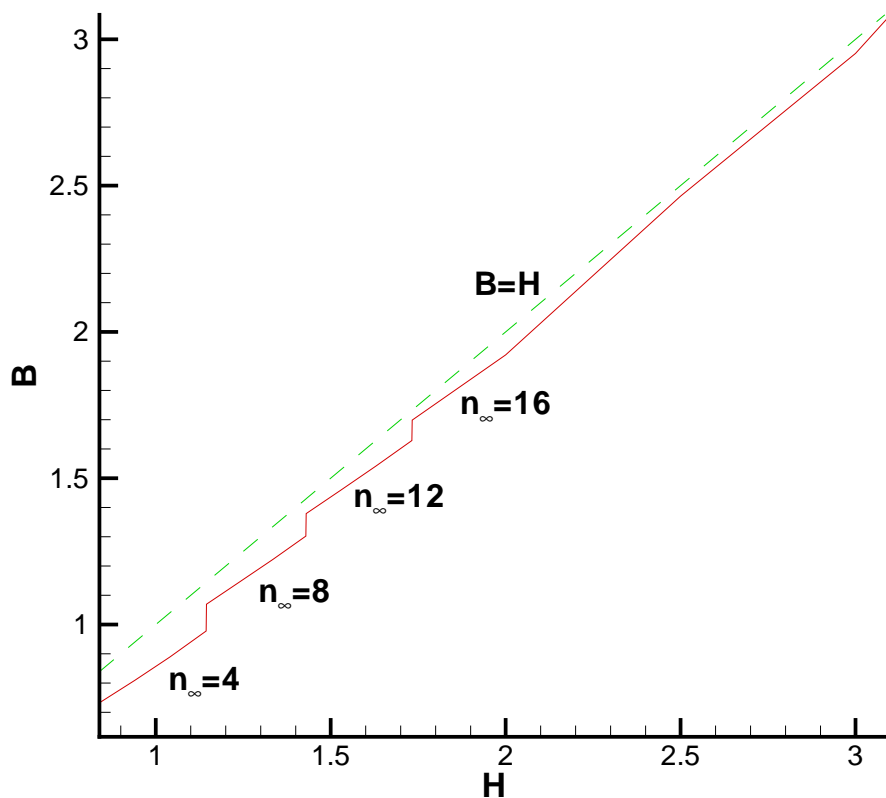


Fig. 7. The effect of an applied magnetic field H on the induced average magnetic field B .

Comparison of Fig. 6 (g) with 6 (h) reveals a phase transition is also evident for the $n_\infty = 12$ case, where the vortex configuration shows a sudden change in arrangement, even with the same number of vortices, for a slight increase of the applied field from $H = 1.454$ to $H = 1.455$.

VII.2. Pseudo-time sequence showing vortex entry dynamics

Figure 8 shows the transient development of Cooper pair density for $H = 1.145$ and there are eight vortices. The perfect symmetry in the sample geometry dominates the transient process, but in the middle of the process the whole configuration makes a rotation to rearrange itself into a new configuration. (Note that time advances from 3000 to 17500 between the 8th and 9th frames.) The final result is still a square-symmetric configuration. We note that during the rotation process, the vortex configuration loses some mirror symmetries of the sample, but it still preserves the 90° rotation symmetry. These transient states need not possess the full symmetry of the sample. We think this is possible because our numerical method has very weakly broken the sample symmetry. That is, the state just before the rotation is metastable only within the subspace of configurations preserving the full symmetry of the sample. Thus, in a physical situation, where the sample has perfect symmetry and the temperature is sufficiently low, this rotation may take a long time to take place. For samples with imperfect symmetry this relaxation time may be shorter. Since this is a symmetry-induced qualitative property of the vortex-entry dynamics in a mesoscopic superconductor, we believe its general validity is independent of the fact that we have obtained it by solving a simplified set of TDGL equations which are not truly physical.

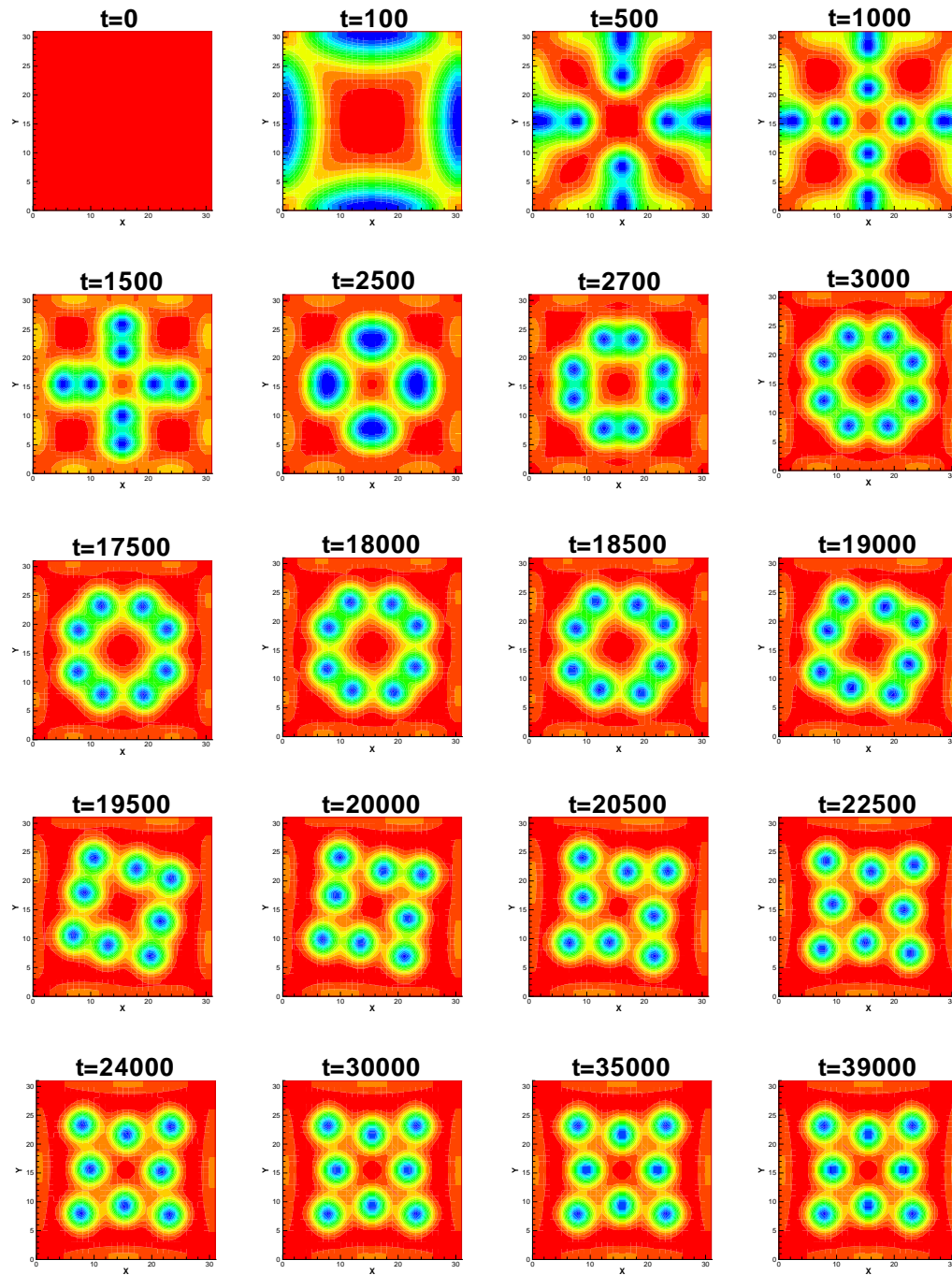


Fig. 8. Pseudo-time sequence of vortex dynamics showing vortex-entry for $H = 1.145$. Note that the initial state is the uniform superconducting state.

CHAPTER VIII

EQUILIBRIUM STATE

VIII.1. Steady states with reduced symmetry and the equilibrium state

The previous sections present solutions for a mesoscopic type-II superconducting square cylinder with initially no vortex inside the system. The validity of such solutions requires a perfectly square sample without any defect at the boundary, and temperature sufficiently low so that thermal fluctuations are too weak to help the system find lower-energy configurations of reduced symmetry. This is an ideal condition, producing only solutions consistent with the sample symmetry. Even during the transient, the system is bound to this symmetry (except in rare cases when the transient solutions can keep only fourfold rotation symmetry but not mirror symmetries — See Fig. 8). In principle, one can reproduce this ideal system in a laboratory with special care.

In real situations, there likely exists some small defects or perturbations at the boundary, then vortices can enter the system asymmetrically to produce steady-state configurations with reduced symmetry of lower total Gibbs energy than any symmetric solution. A strong enough thermal fluctuation could also change the vortex number and rearrange the vortices to such a configuration. Previous work has taken into account these perturbations by adding a random fluctuation term to the governing equation. [58] This term breaks the symmetry governing the equations by energizing the system to jump out of the local minima in energy and over the energy barrier, [25] but this increases the computing time greatly. (This method is essentially “simulated annealing” [47, 48].)

As an alternative approach, we employ perturbed initial conditions (similar to

Peeters et al., [19, 39]) instead of the perfectly superconducting initial condition as used in Figs. 6 and 8. In addition, we introduce a new idea to make the numerical scheme much more efficient. We have first used randomly perturbed initial conditions. This can lead to final steady-state solutions with reduced symmetry and lower energies, but we find this way is very inefficient for finding the equilibrium state at any given H . We also tried to use a lower-symmetry configuration from such a calculation as the initial condition for a new H value, but we found that the vortex number can often be trapped in an uncontrollable non-equilibrium value due to the existence of surface energy barriers against vortex entry or exit. This method of adopting an existing solution as the initial condition can not be reliably used to find the true equilibrium state in a given system and field. (Peeters et al. changes the field in small steps to avoid this difficulty, [59] but such a procedure is tedious.)

To obtain the true equilibrium vortex configuration at any given magnetic field without employing a simulated annealing method, we have devised a systematic approach to generate initial states with given numbers of vortices at random distributions. We start with an analytic expression as follows: for one vortex at the origin in circular coordinates (r, θ) , we use the widely-known approximate expression [36, 60, 61]

$$\Psi(r, \theta) = \frac{r e^{i\theta}}{\sqrt{r^2 + \kappa^{-2}}}. \quad (8.1)$$

By converting it to Cartesian coordinates, we can move the center of the vortex to any arbitrary position (x', y') by simply replacing (x, y) by $(x - x', y - y')$. Denoting this expression as $\Psi_{x', y'}(x, y)$, an n -vortex expression can be simply constructed as:

$$\Psi(x, y) = \Psi_{x_1, y_1}(x, y) \Psi_{x_2, y_2}(x, y) \cdots \Psi_{x_n, y_n}(x, y). \quad (8.2)$$

This expression obeys the important topological condition that the phase of Ψ must

increase by 2π when any one vortex center is circumnavigated. The magnetic field inside the sample does not obey any topological condition, so it can be simply set equal to zero for the initial condition. The positions of vortices can be generated using random number generators, only if they are inside the sample. This is a straightforward idea, but it does not appear to have been employed before. We illustrate below various initial conditions used to obtain steady-state vortex configurations of any given numbers of vortices n_∞ . Comparing the total Gibbs free energy per unit area \bar{G} (obtained by integrating Eq. 4 and normalized by the sample size $N_x h_x \times N_y h_y$) of solutions with different n_∞ , we can then determine the equilibrium vortex number and configuration.

For illustrative purposes, we consider the case $H = 0.840$. Figure 9 shows the initial conditions for Ψ with 1 through 8 randomly-placed (artificial) vortices (the left figures in (a) through (o)), and the steady-state vortex configurations they evolve to (the right figures in (a) through (o)). Indeed in Figures 9 (i),(l),(m),(o), the initial number of vortices is not always the final number. This is because the energy of the initial state is high when vortices are initially very close to each other, in which case there is enough energy to overcome the surface barrier to eject excess vortices. In particular, comparison of the initial and final states in Fig. 9 (h) reveals that one vortex was expelled during the evolution. This is because the surface barrier was weakened, perhaps by one vortex in the initial state being close to the edge of the sample, and the total number of vortices being too high compared with the final equilibrium vortex number. The corresponding total Gibbs free energies, \bar{G} , of these steady states are plotted in Fig. 10 as a function of the final vortex number n_∞ . The minimum-energy configuration at $n_\infty = 5$ is seen to display the square-symmetry of a five-vortex configuration with a vortex in the center.

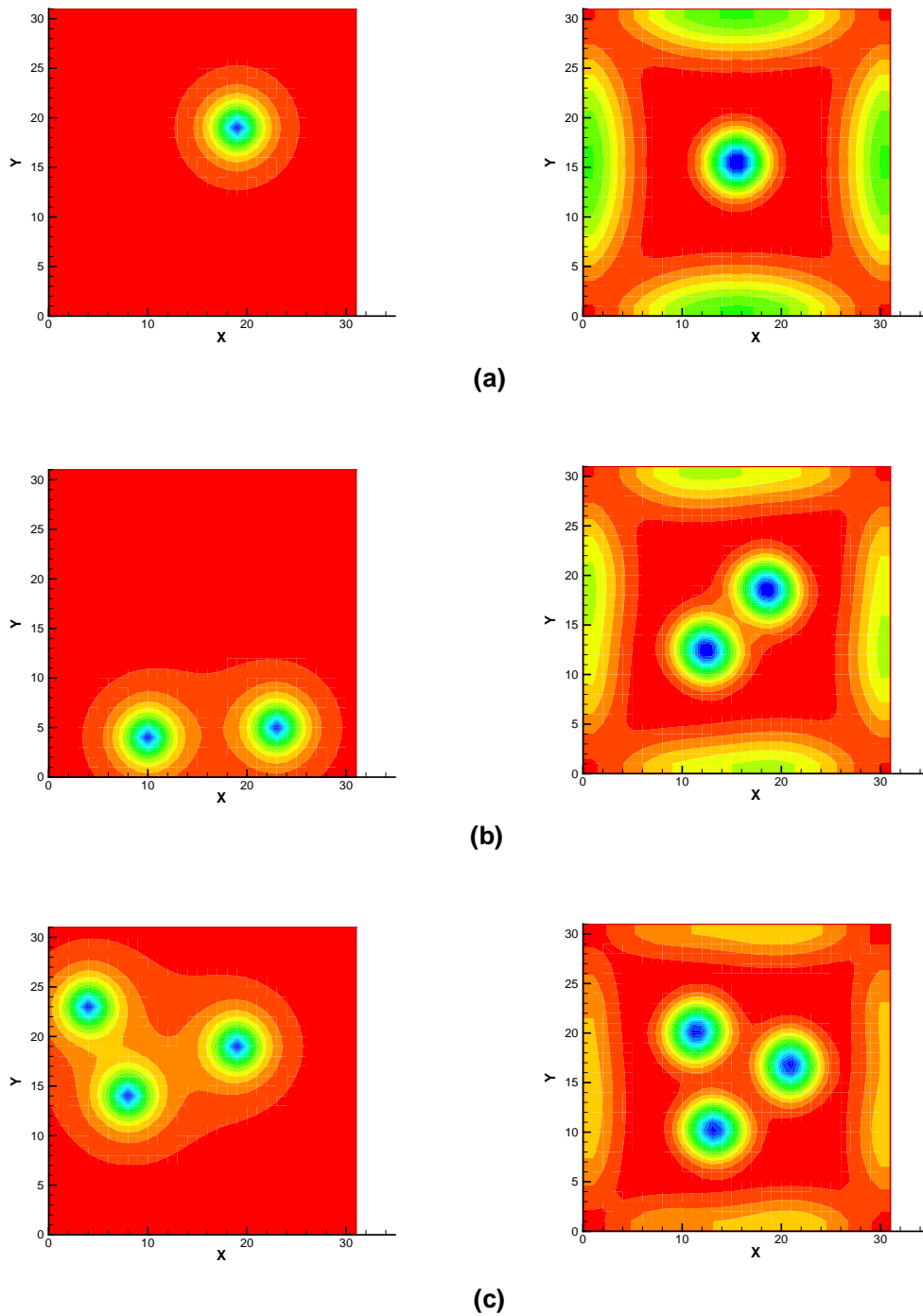
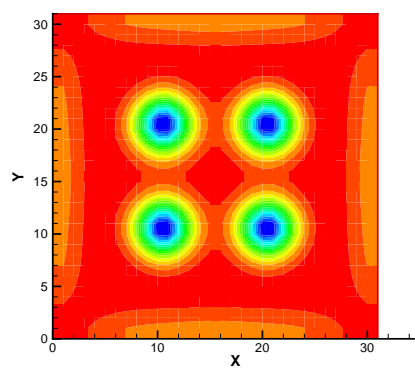
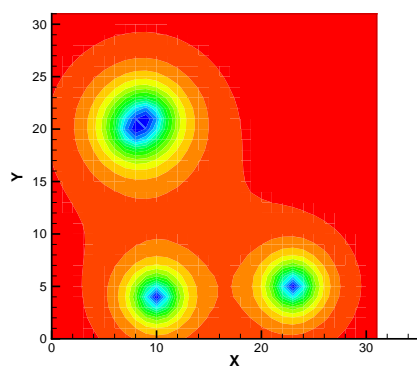
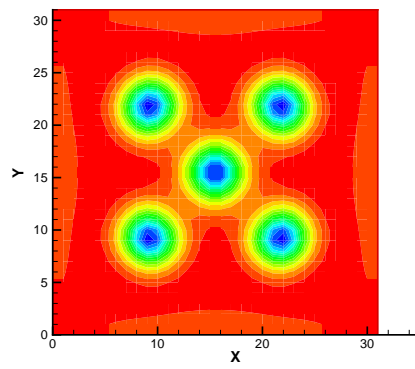
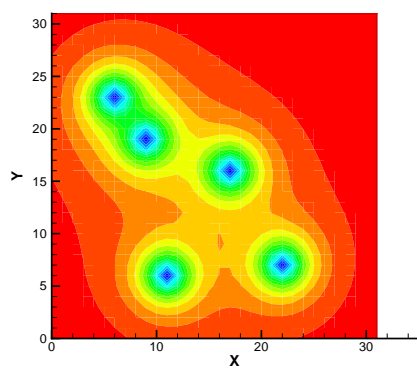


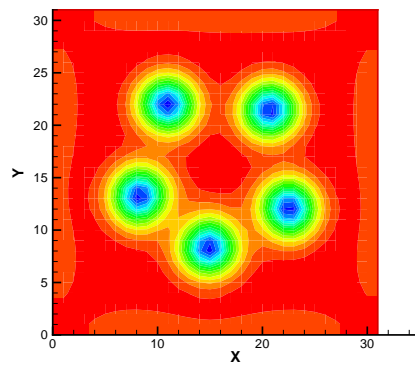
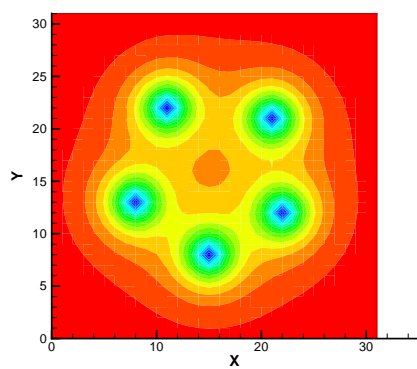
Fig. 9. The initial, random vortex configurations, and the corresponding steady-state vortex configurations they evolve to [The initial vortex configurations is shown on the left in (a) to (c), and the steady-state vortex configurations on the right in (a) to (c)]. Most of these final steady-state solutions are metastable states with a given number of trapped vortices in a field-cooled situation. The one with the lowest Gibbs energy among them may be identified as the true equilibrium state at the chosen field value, see Fig.10.



(d)

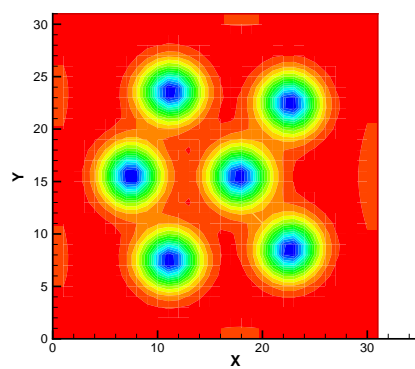
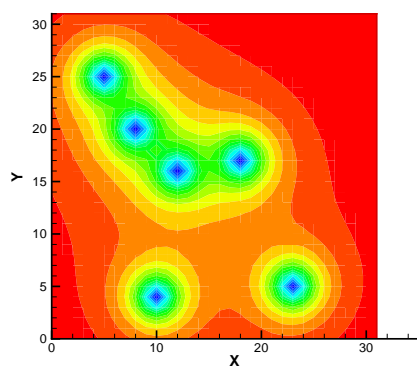


(e)

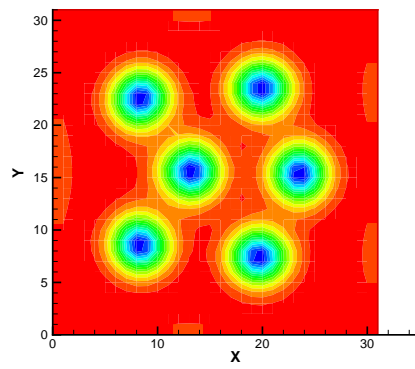
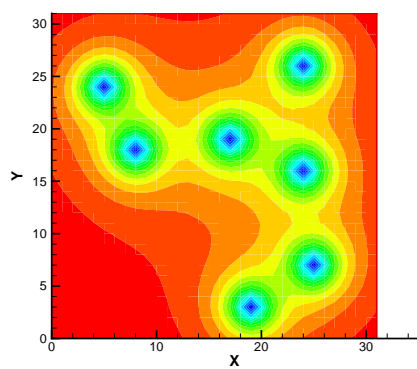


(f)

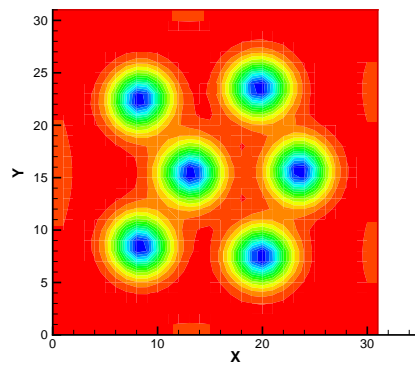
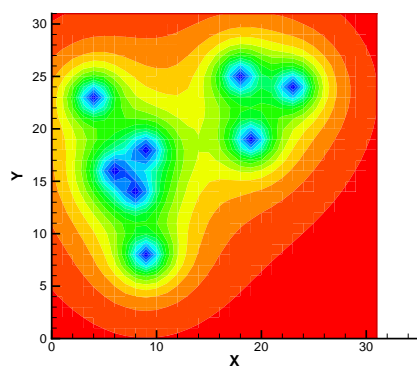
Fig. 9 (*cont.*)



(g)

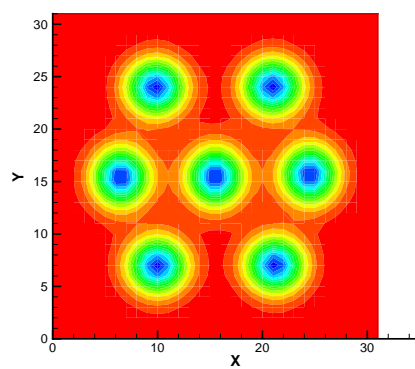
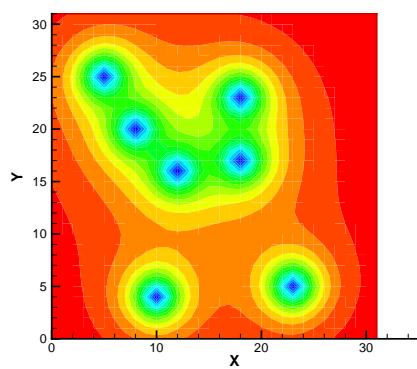


(h)

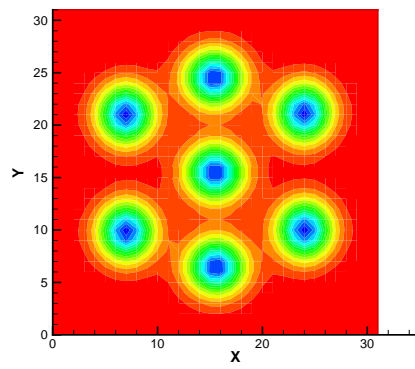
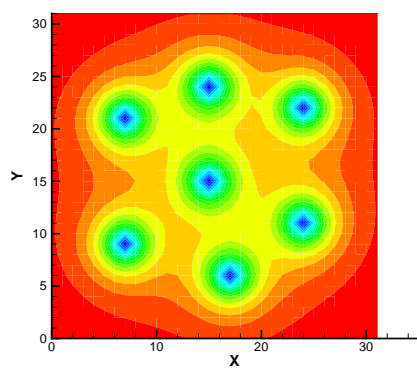


(i)

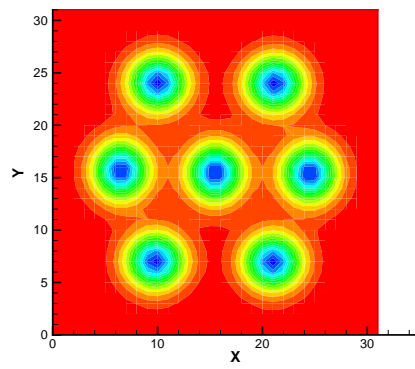
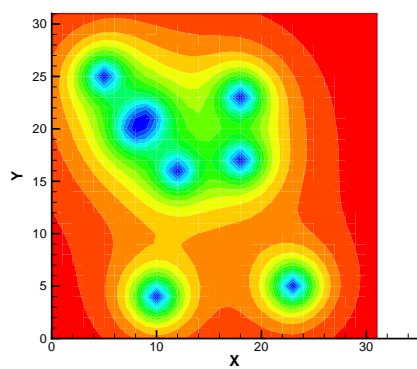
Fig. 9 (cont.)



(j)

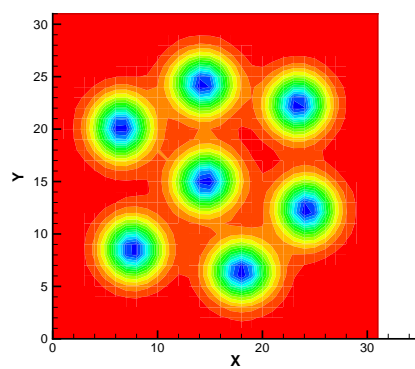
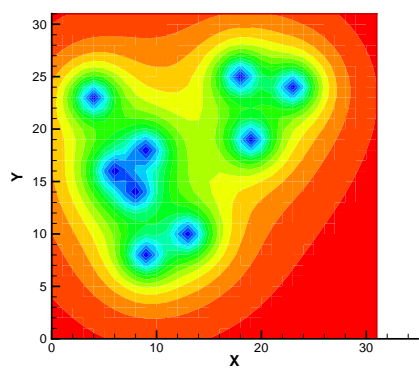


(k)

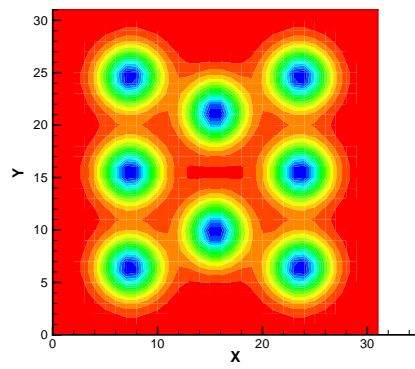
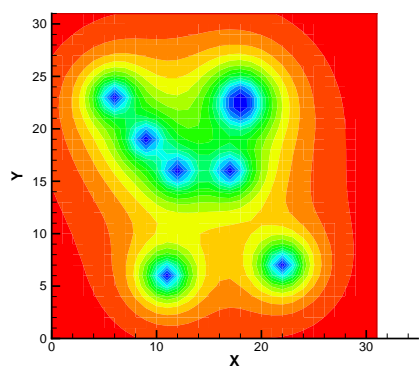


(l)

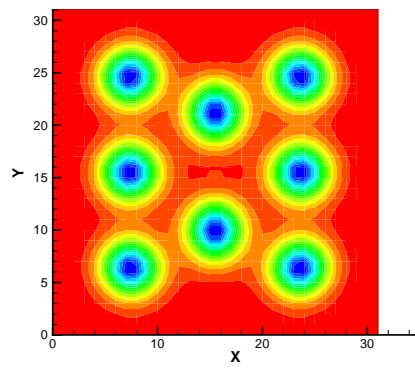
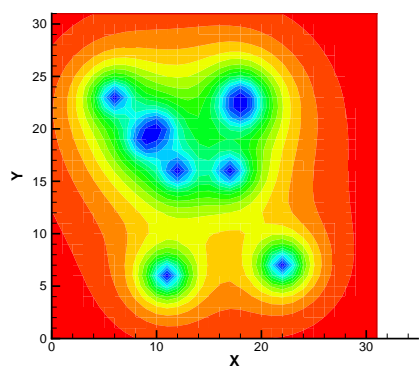
Fig. 9 (cont.)



(m)



(n)



(o)

Fig. 9 (cont.)

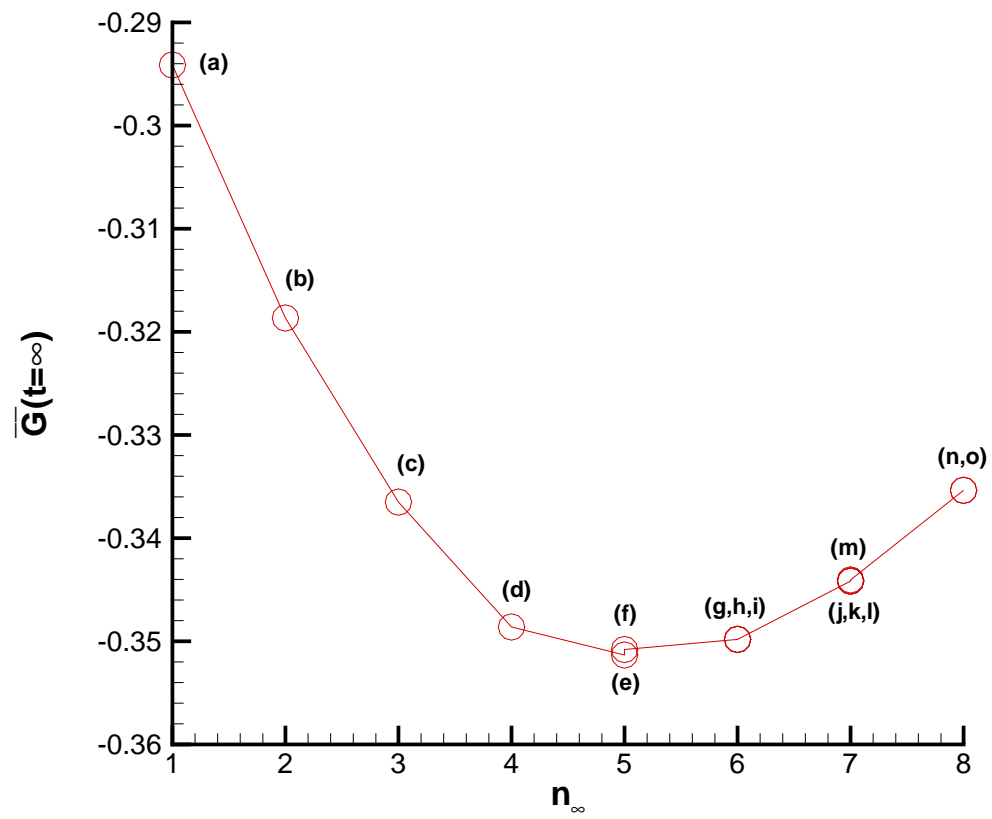


Fig. 10. The steady-state total Gibbs free energy per unit area \bar{G} and the corresponding final number of vortices, n_∞ .

VIII.2. Grid independence

Grid independence checks were performed, and Fig.11(a) shows this 5 vortex case using grids of 64×64 , and in Fig.11(b) a uniformly superconducting initial condition with $H = 1.733$ corresponding to Fig.6(j). Comparison of Fig.9(e) (32×32 grid) with Fig.11(a) (64×64 grid) reveals close agreement. Similarly comparison of Fig.6(j) and Fig.11(b) shows close agreement. A more stringent grid independence test was to consider the resultant total Gibbs free energy for each grid, and given in Table II. Inspection of the table reveals convergence to less than a 1% change when moving to different grids. The percent error was defined as:

$$\%error = |\bar{G}_{64 \times 64} - \bar{G}_{32 \times 32}| \times 100 / |\bar{G}_{32 \times 32}|, \quad (8.3)$$

and similarly for other cases. These grid independence results support our use of 32×32 grids for this study. The large error of 14.1% for the uniform initial condition case in Table II was associated with a decrease from 16 vortices to 12 when the grid was coarsened from 32×32 to 16×16 . The reduction in resolution caused the vortex number to cross the H-threshold and produced a 12 vortex configuration. Our exploration of finer grids ensured that we determined an accurate H-threshold, and not one dependent on the grid.

Although we have not yet applied this scheme to other field values of H , the method we have devised to find the equilibrium vortex configurations for a given size and shape of the sample, and different values of the external magnetic field should now be clear.

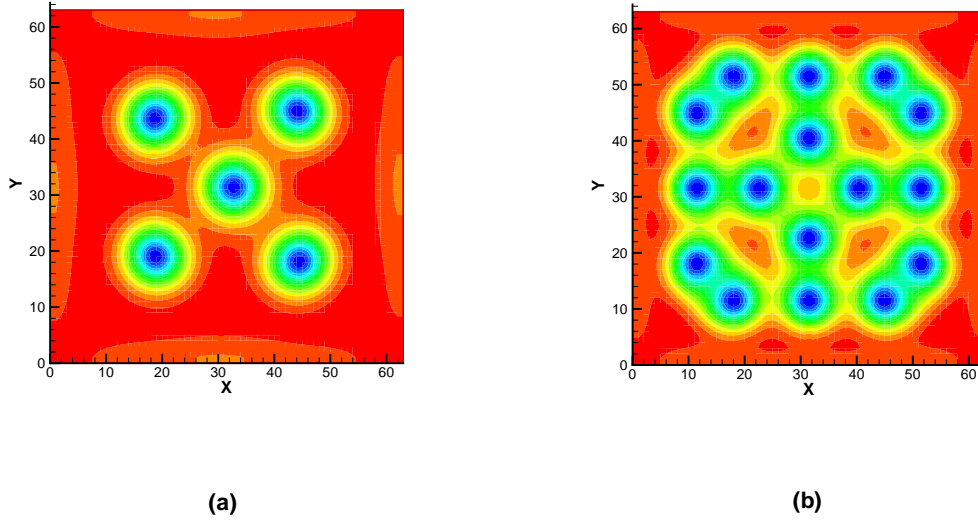


Fig. 11. Examples of the steady-state vortex configurations for larger grid size (64×64). (a) artificial vortex initial condition under $H = 0.84$, and (b) uniformly superconducting initial condition under $H = 1.733$.

Table II. The steady-state total Gibbs free energy \bar{G} and % error in \bar{G} for changing grid size for artificial vortex initial condition ($H = 0.84$) and uniformly superconducting initial condition ($H = 1.733$).

Grid	Artificial IC		Uniform IC	
	\bar{G}	%error	\bar{G}	%error
16×16	-0.3487	0.71	-0.1814	14.1
32×32	-0.3513		-0.2069	
32×32	-0.3513	0.17	-0.2069	0.41
64×64	-0.3519		-0.2078	

CHAPTER IX

INTRODUCTION TO PART II: OPTIMAL PINNING CONFIGURATION TO
TRAP A VORTEX-ANTIVORTEX PAIR IN A SUPERCONDUCTING FILM
UNDER THE NON-UNIFORM MAGNETIC FIELD OF A MAGNETIC DIPOLE

In this part, the parameters for nano-pinning inside a type-II, thin-film superconductor are investigated by numerical experiments. The film is subject to a non-uniform magnetic field from a magnetic dipole above the film, and has pinning centers such as holes (called *antidots*) of various sizes and locations (Figure 12). Since $d_{film} = 0.1\xi \ll \lambda$, the film is virtually transparent to magnetic penetrations in the thickness direction, and “soaked” in the applied magnetic field (Figure 13). In a superconduction film, the induced magnetic fields by the supercurrents incur only negligible change in the applied magnetic field.

The simulation involves two distinctive parts: (i) magnetic flux penetration into a thin film by the external magnetic field from a magnetic dipole, which creates a vortex and antivortex pair; (ii) pinning of the pair of vortex-antivortex at a hole or defect configuration in the film with the external magnetic source is removed. The situation is not as simple as it might look, since there are magnetic interactions in and out of the film, which is not the case in an infinitely long cylinder.

Ferromagnetic particles, fabricated onto a superconductor, have many effects of fundamental interest. Van Bael *et.al.* [62] have considered a ferromagnetic dot array with a magnetic dipole moment parallel to the surface of superconducting substrate. They showed that the flux lattice (FL) is pinned at the ends of the ferromagnetic dots (FD), where a flux quantum of opposite sign is induced by the stray field.

Nozaki *et.al.* [63] investigated the effect of the spatially modulated local field by a ferromagnetic dot array on a Nb film. Since the magnetic field line from the ferro-

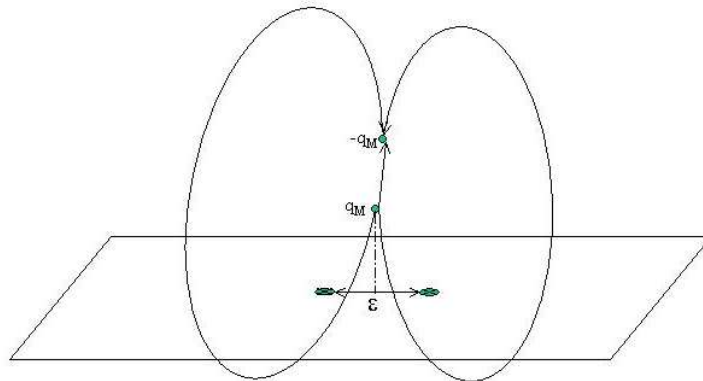


Fig. 12. A superconducting film under a magnetic dipole. Stray field lines penetrating the film creates vortex-antivortex pair(s). They may be pinned at pinning centers such as holes (antidots) made in the film in a proper configuration, shown here in the distance ϵ apart.

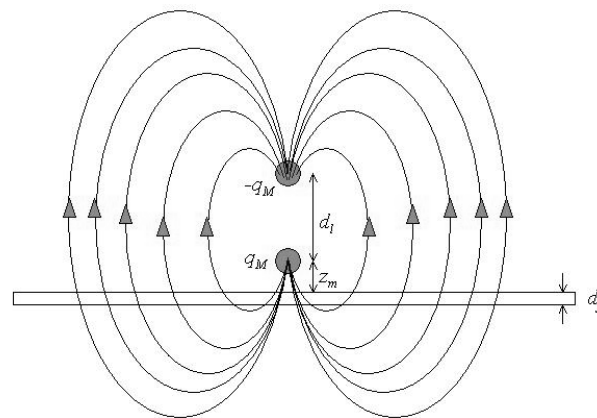


Fig. 13. A superconducting film under a magnetic dipole. Stray field lines penetrating the film creates vortex-antivortex pair(s). Since $d_{film} = 0.1\xi$, the film is virtually transparent to magnetic penetration in the thickness direction, and “soaked” in the applied magnetic field. In the superconducting film, the induced magnetic fields by the supercurrents incur only negligible change in the applied magnetic field.

magnetic dots suppresses superconductivity where it penetrates, these magnetic dipoles (i.e. FD's) can effectively create vortices and antivortices and also have pinning effect on those vortices.

Milošević and Peeters [64] have considered a ferromagnetic disk on top of thin superconducting film. They found that, as the magnetic field lines penetrate and change polarity in the film, vortex-antivortex pairs are created and arrange themselves in a symmetrical pattern. Giant vortex and later multivortices are located under the FD and antivortices locate themselves around the circumference. As the magnetic moment of the dot increases, vorticity increases, and eventually a giant vortex under the ferromagnetic disk splits itself into multivortices.

Here the total flux conservation and the flux quantization condition dictates the creation of vortex-antivortex pairs. The field lines from the magnetic dipole should change its polarity as a function of distance since the total flux through the sample is zero. Since vortices are topological excitations, there should be an equal production of vortices and antivortices.

Priour and Fertig [65] performed a similar Ginzburg-Landau study for the vortex states in a superconducting thin film, subject to the magnetic field of a magnetic dot array, with the dipole moments oriented perpendicular to the film. They found the vortex-antivortex pair density shows broad plateaus as a function of the dipole strength, and many of the plateaus correspond to vortex configurations that break dot lattice symmetries.

Vortex pinning is a mechanism that attracts and holds the vortices in place. It is this pinning mechanism that is responsible for the critical current and hysteresis in the magnetic behavior of the superconductor. [25, 29] Any defects such as magnetic dots above, twin boundaries [45], local spots with lower critical temperature T_c [66], or variable thickness [67] act as pinning centers.

Submicronic holes, called *antidots*, are a well-known, strong pin. The free energy of a system consisting of a vortex and a cavity in a superconductor is obtained analytically by solving the London equation [68, 69]. It has been shown that a small antidot induces a negative potential around its center, which attracts vortices and becomes repulsive after trapping a vortex of a single quantum. Budzin [70] has shown that for large enough antidots, multiple flux quanta can be trapped. Takezawa and Fukushima [71] presented a formulation for the pinning force on a vortex moving around a square antidot, with the distance and the dot size as the key parameters.

Priour and Fertig [72] performed numerical studies of vortices in the presence of arrays of artificial defects for a thin film. They show that when a vortex approaches the vicinity of a defect, the vortex core extends to the defect boundary and simultaneously supercurrents and associated magnetic flux spread out, engulfing the defect. Regarding the GL energy, E_{GL} , as a pinning potential, they considered the gradient of the energy to evaluate the pinning force and observed a phase transition after the vortices pass a critical distance d_c .

Most topics discussed above relate to vortex lines, implying an infinitely long vortex column or vortex line. Columnar defects created by heavy-ion irradiation technique have been known as an efficient pinning centers strongly enhancing the critical current density. [73] Thin film presents a new challenge to the analysis. The vortices inside the film are no longer the Abrikosov type, but become Pearl vortices. Pearl [74] has solved the London equation for vortices moving in a thin film, and showed that the vortices have a longer range interaction force and are harder to pin. This leads to the concept of an *effective* penetration depth $\lambda_{eff} = \lambda^2/d$, which is much longer than λ in thin films. One common method to investigate the pinning characteristics of a superconductor is to perform an electric transport measurement. The critical current J_c can be determined by slowly raising the current density until dissipation

suddenly appears. By balancing the Lorentz force induced by this current with the pinning force, the pinning strength can be determined. Machida and Kaburaki [75] is one example of the work done in this context.

IX.1. Pearl vortex theory

J. Pearl [74, 24] has presented a mathematical analysis for vortex dynamics in an (infinitely) thin superconducting film in the framework of London model. We will numerically solve Ginzburg-Landau equations instead of London's. Yet Pearl's analytical work gives us a good introduction to this problem.¹

In a continuous superconducting film of thickness d and of infinite extent, for $d/\lambda \ll 1$ (λ is the London penetration depth), the current density in the film is essentially uniform across the thickness and can be represented as an infinitesimally thin current sheet as the following (not non-dimensionalized in this section):

$$\mathbf{j}_s = \mathbf{j}_{2D}(x, y) d \delta(z) \quad (9.1)$$

According to the London model $\mathbf{j}_{2D} = -\mathbf{A}(z=0)/\lambda^2$, the Maxwell-London equation can be written as

$$\nabla^2 \mathbf{A} = -\mathbf{j}_{total} = -\mathbf{j}_e - \mathbf{j}_{2D} d \delta(z) = -\mathbf{j}_e + \frac{d}{\lambda^2} \mathbf{A} \delta(z) \quad (9.2)$$

where $\mathbf{H} = \text{curl} \mathbf{A}$ and \mathbf{j}_e is an external current arbitrarily applied parallel to the film. This can be rewritten in Fourier transform

$$\mathbf{A}(\mathbf{k}) = \frac{1}{k^2} [\mathbf{j}_e(\mathbf{k}) + \mathbf{j}_{2D}(\mathbf{k}_{2D})] \quad (9.3)$$

where $\mathbf{k} = k_x \hat{\mathbf{e}}_x + k_y \hat{\mathbf{e}}_y + k_z \hat{\mathbf{e}}_z = \mathbf{k}_{2D} + k_z \hat{\mathbf{e}}_z$ is the wave number vector in the Fourier

¹In this section, MKS unit system is employed according to Pearl's original work. The rest of the dissertation is in Gaussian units.

space.

The supercurrent (9.1) and the London model ($\mathbf{j}_{2D} = -\mathbf{A}(z=0)/\lambda^2$) lead to

$$\mathbf{j}_{2D}(\mathbf{k}_{2D}) = \frac{1}{2\pi\lambda^2} \int \mathbf{A}(\mathbf{k}) dk_z. \quad (9.4)$$

Solving these together we obtain the supercurrents' projection function in \mathbf{k} -space:

$$\mathbf{j}_{2D}(\mathbf{k}_{2D}) = -\frac{1}{1 + 2k_{2D}\lambda^2/d} \mathbf{j}_e(\mathbf{k}_{2D} - ik_{2D}\hat{\mathbf{e}}_z) \quad (9.5)$$

In a situations in which the film supports a finite fluxoid, in an analogy with non-viscous flow, we define supercurrent's potential field Φ . [1] That is, from rewriting the London equation (2.1) as $\nabla \times (\Lambda \mathbf{j}_s + \frac{1}{c} \mathbf{A}) = 0$, we can define the potential field

$$\Phi = \mathbf{A} + \lambda^2 \mathbf{j}_s \quad (9.6)$$

where Φ is the same as \mathbf{A} in normal region and describes a “streamline flow” in superconducting area. Putting this potential field into the Maxwell-London equation,

$$\nabla^2 \mathbf{A} = \frac{d}{\lambda^2} (-\Phi + \mathbf{A}) \delta(z) \quad (9.7)$$

Comparing this expression with eq. (9.2), Φ may be considered to correspond to an externally applied current sheet of strength $(d/\lambda^2)\Phi$ on the film. From Pearl's equation (9.5) above, the supercurrent is related to Φ by

$$\mathbf{j}_{2D}(\mathbf{k}_{2D}) = \frac{d}{\lambda^2} \Phi(\mathbf{k}_{2D}) \left(1 - \frac{1}{1 + 2k_{2D}\lambda^2/d} \right) \quad (9.8)$$

If we put a potential for a vortex carrying a flux quantum $\Phi_0 = ch/2e$ and located at the origin, i.e. $\Phi(r) = \frac{\Phi_0}{2\pi r} \hat{\mathbf{e}}_\phi$ (where $\hat{\mathbf{e}}_\phi$ is a unit vector in the azimuthal direction in the cylindrical coordinates), the Maxwell-London equation becomes

$$\nabla^2 \mathbf{A} = \frac{d}{\lambda^2} \left(-\frac{\Phi_0}{2\pi r} \hat{\mathbf{e}}_\phi + \mathbf{A} \right) \delta(z) \quad (9.9)$$

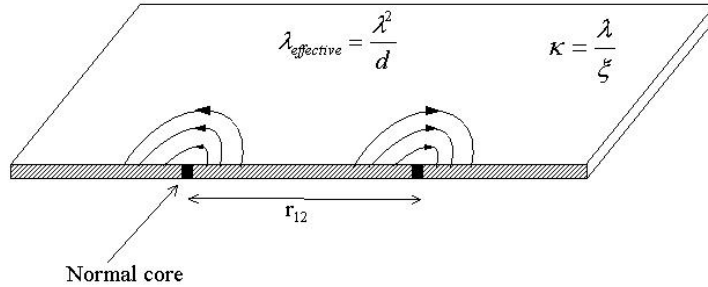


Fig. 14. Superconducting film carrying a pair of vortex-antivortex. There is an attractive interaction force between the vortex and antivortex. The effective penetration depth λ_{eff} increases as the film thickness d decreases. Hence for a thin film ($d \ll 1$) the interaction force between the vortex-antivortex pair has a much longer range than the penetration depth λ .

and solved by Hankel transform, results in

$$\mathbf{j}_{2D}(r) \approx \hat{\mathbf{e}}_\phi \frac{1}{\pi} \Phi_0 \left(\frac{d}{2\lambda^2 r} \right) \quad \text{for } r \ll 2\lambda^2/d \quad (9.10)$$

and

$$\mathbf{j}_{2D}(r) \approx \hat{\mathbf{e}}_\phi \frac{1}{\pi} \Phi_0 \left(\frac{1}{r^2} \right) \quad \text{for } r \gg 2\lambda^2/d \quad (9.11)$$

Using this result, we can calculate the interaction of, e.g. a pair of vortex and antivortex (see Fig.14). That is,

$$\text{curl} \mathbf{\Phi} = \Phi_0 \hat{\mathbf{e}}_z [\delta(x-b) - \delta(x+b)] \delta(y). \quad (9.12)$$

Using the fact that the total energy is $\frac{1}{2} \mu_0 \phi_0$ times the total current flowing between the vortices [1], we get the interaction force between the vortices

$$f_{12} = -\frac{1}{2} \mu_0 \Phi_0 \cdot 2j_{2D}(r_{12}) \approx -\mu_0 \frac{\Phi_0^2}{\pi} \frac{1}{r_{12}^2}, \quad \text{for } r_{12} \gg 2\lambda^2/d \quad (9.13)$$

and

$$f_{12} = -\frac{1}{2}\mu_0\Phi_0 \cdot 2j_{2D}(r_{12}) \approx -\mu_0\frac{\Phi_0^2}{\pi} \left(\frac{d}{2\lambda^2 r_{12}} \right), \quad \text{for } r_{12} \ll 2\lambda^2/d \quad (9.14)$$

Thus the vortices have a long range interaction force in thin films, unlike the short range of interactions in bulk superconductors. Such a long range force would cause the vortices to migrate toward each other and eventually annihilate each other unless there are pins to hold them.

IX.2. Antidots in a bulk superconductor

Mkrtchyan and Shmidt [68] have presented a mathematical analysis for the pinning of a vortex by a cavity in a type-II superconductor.² Solving the generalized London equation for the magnetic field in the superconductor

$$\mathbf{H}(\rho) + \text{curlcurl } \mathbf{H}(\rho) = \frac{2\pi}{\kappa}\delta(\rho - \rho_0) \hat{\mathbf{e}}_z, \quad \mathbf{H}|_S = H_0, \quad (9.15)$$

Here the S is the surface of the cavity of radius R , $\hat{\mathbf{e}}_z$ is a unit vector along the vortex axis, and ρ_0 is the position vector of the vortex.

In the cylindrical coordinate system (ρ, ϕ) with center on the cavity axis, we have the system to solve

$$\begin{aligned} \frac{\partial^2 H}{\partial \rho^2} + \frac{1}{\rho} \frac{\partial H}{\partial \rho} - \frac{1}{\rho^2} \frac{\partial^2 H}{\partial \phi^2} - H &= -\frac{2\pi}{\kappa\rho} \delta(\phi) \delta(\rho - \rho_0), \\ H(R, \phi) &= H_0, \\ H(\infty, \phi) &= 0 \end{aligned} \quad (9.16)$$

²This two-dimensional analysis is presented on the purpose of demonstrating basic physical mechanism in which pins attract vortices. In thin films, the magnetic interaction is three-dimensional through the field lines in and out of the film.

Solving this equation we get

$$H(\rho, \phi) = H_0 \frac{K_0(\rho)}{K_0(r)} + \sum_{k=-\infty}^{\infty} H_k(\rho) e^{ik\phi} \quad (9.17)$$

where

$$H_k(\rho) = \frac{1}{\kappa} \frac{K_k(\rho_0)}{K_k(r)} [I_k(\rho)K_k(r) - I_k(r)K_k(\rho)], \quad r \leq \rho \leq \rho_0 \quad (9.18)$$

and

$$H_k(\rho) = \frac{1}{\kappa} \frac{K_k(\rho)}{K_k(r)} [I_k(\rho_0)K_k(r) - I_k(r)K_k(\rho_0)], \quad \rho_0 \leq \rho < \infty \quad (9.19)$$

where K_k and I_k are defined in Ref. [76].

Here the flux quantization condition plays a pivotal role to determine H_0 . That is, writing current as

$$\text{curl } \mathbf{H} = \frac{1}{\kappa} \nabla \Phi - \mathbf{A} \quad (9.20)$$

where Φ is the phase of the order parameter. Integrating this equation along the circular contour of the cavity of radius r , we have

$$r \int_0^{2\pi} \text{curl}_\phi \mathbf{H} d\phi = \frac{2\pi}{\kappa} n - \pi r^2 H_0 \quad (9.21)$$

after finishing the integral with \mathbf{H} (9.17) derived earlier, we finally have

$$H_0 = \frac{K_0(\rho_0)}{\kappa} + n \frac{K_0(r)}{\kappa}. \quad (9.22)$$

The first term is the field produced in the cavity by the nearby vortex filament. The second term is the field determined by the number n of the magnetic flux quanta captured by the cavity. This quantity is quantized and equals the field remaining in the cavity if the vortex filament is removed to infinity.

With all these information, the free energy of the system

$$\mathcal{F} = \int [H^2 + (\text{curl} \mathbf{H})^2] dV \quad (9.23)$$

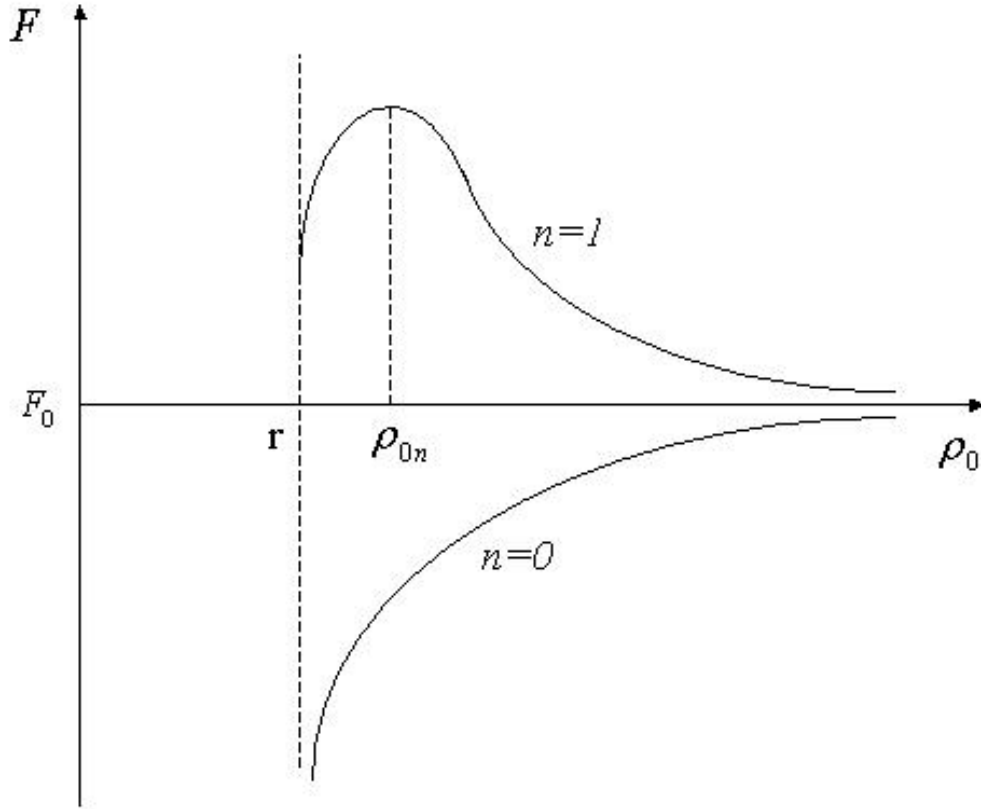


Fig. 15. Free energy of the system F in the direction of the coordinate ρ_0 .

is calculated as

$$\mathcal{F} = \mathcal{F}_0 + \frac{4\pi}{\kappa^2} \left[\frac{1}{2} \ln \left(1 - \frac{r^2}{\rho_0^2} \right) + nK_0(\rho_0) \right], \quad \rho_0 \ll 1 \quad (9.24)$$

and

$$\mathcal{F} = \mathcal{F}_0 + \frac{4\pi}{\kappa^2} nK_0(\rho_0), \quad \rho_0 \gg 1, \quad n \neq 0 \quad (9.25)$$

where

$$\mathcal{F}_0 = \frac{4\pi}{\kappa} \left[H_{c1} + \frac{n}{2\kappa} K_0(r) \right] \quad (9.26)$$

Fig. 15 show the free energy decreases as the vortex gets near to the cavity when

there is no vortex already trapped inside. That is, cavity attracts the vortex. We can find the mechanical force of interaction between the vortex filament and the cavity, i.e. the pinning force from

$$f_p = - \left. \frac{\partial \mathcal{F}}{\partial \rho_0} \right|_{\rho_0=r+1/\kappa} \quad (9.27)$$

We do not expect, however, this theory would apply exactly to our current study. Since they solved a generalized London equation, the vortex core energy is ignored and only electromagnetic contribution to the pinning force is considered. Furthermore, in the thin film geometry we will study, *magnetic flux is not quantized*.³ Thus we cannot fix the H_0 in terms of ρ_0 , r , and κ . nevertheless, this exemplar work by Mkrтчyan and Shmidt gives a vivid account for the interaction and mechanism of how pinning work.

Similar study using a prismatic insulating inclusion and a vortex was done by Takezawa and Fukushima [71] by numerically solving Ginzburg-Landau equations. Major conclusion from their work was that the pinning was strongest for a pin of size of about $\lambda(T)$, the penetration depth, in contrast to the conventional belief for $2\xi(T)$. Again, this result for two-dimensional vortex filaments is not expected to apply exactly to our thin film, but can be a reference point of thinking.

³In any geometry involving thin surfaces such as a cylinder with thickness less than the penetration depth, there exists no closed loop of supercurrents $\mathbf{j} = 0$. Thus the topological condition for flux quantization is not satisfied any more.

CHAPTER X

GINZBURG-LANDAU EQUATION FOR THIN FILM

Starting with the Gibbs free energy given in eq.(6.3), we nondimensionalize it in the following form (omitting primes for convenience):

$$G(\Psi, \mathbf{A}) = \int_{\Omega} \left(-|\Psi|^2 + \frac{1}{2}|\Psi|^4 + |(-i\nabla - \mathbf{A})\Psi|^2 + \kappa^2|\nabla \times \mathbf{A} - \mathbf{H}|^2 \right) d\Omega \quad (10.1)$$

Here the distance is measured in units of the coherence length ξ , the vector potential in $c\hbar/2e\xi$, and the magnetic field in $H_{c2} = c\hbar/2e\xi^2 = \sqrt{2}\kappa H_c$, where $\kappa = \lambda/\xi$ is the Ginzburg-Landau parameter, and λ is the penetration depth. (That is, $x' = \frac{x}{\xi}$, $\mathbf{A}' = \frac{\mathbf{A}}{c\hbar/2e\xi}$, $\mathbf{H}' = \frac{\mathbf{H}}{c\hbar/2e\xi^2}$, $\mathbf{h}' = \frac{\mathbf{h}}{c\hbar/2e\xi^2}$, etc., before omitting the primes.)

The Ginzburg-Landau equations obtained by minimizing this functional are,

$$(-i\nabla - \mathbf{A})^2 \Psi = \Psi (1 - |\Psi|^2), \quad (10.2)$$

$$\mathbf{j} = \kappa^2 \nabla \times \nabla \times \mathbf{A} = \frac{1}{2i} (\Psi^* \nabla \Psi - \Psi \nabla \Psi^*) - |\Psi|^2 \mathbf{A} \quad (10.3)$$

For thin film superconductors ($d < \xi, \lambda$), we can average the GL equations over the film thickness d . [64] Then the first Ginzburg-Landau equation remains the same form except that the gradient term becomes two-dimensional.

$$(-i\nabla_{2D} - \mathbf{A})^2 \Psi = \Psi (1 - |\Psi|^2), \quad (10.4)$$

However, the supercurrent density over the thickness becomes $\mathbf{j} = d_{film} \delta(z) \mathbf{j}_{2D}(x, y)$ where \mathbf{j}_{2D} is the supercurrent density on the film plane. That is, we assume the current is uniform across the thickness. Then applying the identity $\nabla \times \nabla \times \mathbf{A} = \nabla \nabla \cdot \mathbf{A} - \nabla^2 \mathbf{A}$, the second equation becomes

$$-\Delta_{3D} \mathbf{A} = \frac{d}{\kappa^2} \delta(z) \mathbf{j}_{2D}, \quad (10.5)$$

and

$$\mathbf{j}_{2D} = \frac{1}{2i} (\Psi^* \nabla_{2D} \Psi - \Psi \nabla_{2D} \Psi^*) - |\Psi|^2 \mathbf{A} \quad (10.6)$$

Here the London gauge $\nabla \cdot \mathbf{A} = 0$ is employed for the vector potential \mathbf{A} .

Figure 16 shows an arbitrary sample spanned by the lattice vectors \mathbf{b}_1 and \mathbf{b}_2 .

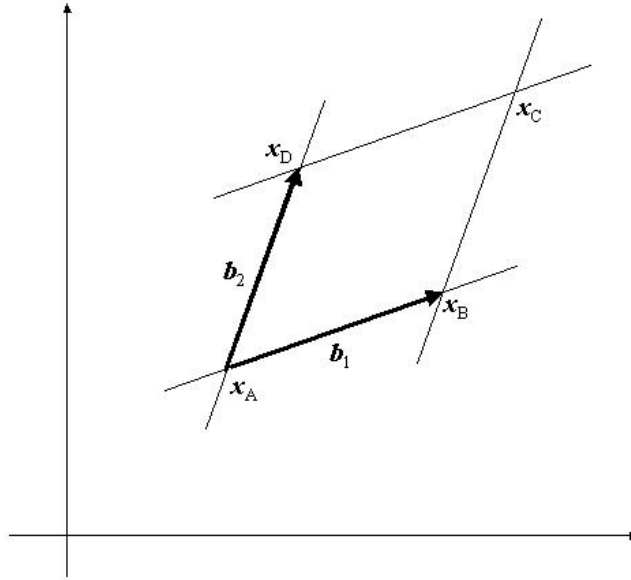


Fig. 16. A periodic sample spanned by the lattice vectors \mathbf{b}_1 and \mathbf{b}_2 .

The periodic boundary conditions for \mathbf{A} and Ψ have the form

$$\mathbf{A}(\mathbf{x} + \mathbf{b}_i) = \mathbf{A}(\mathbf{x}) + \nabla \eta_i(\mathbf{x}) \quad (10.7)$$

$$\Psi(\mathbf{x} + \mathbf{b}_i) = \Psi(\mathbf{x}) \exp(2\pi i \eta_i(\mathbf{x}) / \Phi_0) \quad (10.8)$$

where $b_i, i = 1, 2$ are the lattice vectors, and η_i is the gauge potential which cannot be chosen freely but must preserve the single-valuedness of \mathbf{A} and Ψ . These boundary

conditions mean that a lattice translation amounts to a gauge transformation of \mathbf{A} and Ψ . Physical observables such as the magnetic field, the current, and the Cooper pair density are periodic. It has been shown [77] that the change in the values of gauge potential along the lattice vectors specify the number of flux quanta carried by the system in a unit cell. Here we have $\eta_i = 0$ since the total net flux in the cell is zero.

X.1. Induced magnetic field by supercurrents

The second Ginzburg-Landau equation for the induced magnetic field by supercurrents in the film, can be solved analytically with periodic boundary conditions.

$$-\Delta_{3D}\mathbf{A} = \frac{d}{\kappa^2}\delta(z)\mathbf{j}_{2D} \quad (10.9)$$

decomposed in Cartesian components $\mathbf{A} = (A_x, A_y, A_z)$ and $\mathbf{j}_{2D} = (j_x, j_y)$, becomes

$$\nabla_{3D}^2 A_x = -\frac{d}{\kappa^2}\delta(z)j_x(x, y) \quad (10.10)$$

$$\nabla_{3D}^2 A_y = -\frac{d}{\kappa^2}\delta(z)j_y(x, y) \quad (10.11)$$

$$\nabla_{3D}^2 A_z = 0 \quad (10.12)$$

To solve these PDEs, we apply the well-known Green's function method. [78] A Green function for the given PDE satisfies

$$\nabla_{3D}^2 G(\mathbf{x}, \mathbf{x}') = -4\pi\delta(\mathbf{x} - \mathbf{x}') = -4\pi\delta(x - x')\delta(y - y')\delta(z - z') \quad (10.13)$$

Solving this PDE for G using the method of separation of variables, we get

$$G(\mathbf{x}, \mathbf{x}') = \frac{2\pi}{ab} \sum_{l=-\infty}^{\infty} \sum_{m=-\infty}^{\infty} \frac{1}{\gamma_{lm}} e^{i\frac{2\pi l}{a}(x-x')} e^{i\frac{2\pi m}{b}(y-y')} e^{-\gamma_{lm}|z|} \quad (10.14)$$

where $\gamma_{lm} = 2\pi\sqrt{\frac{l^2}{a^2} + \frac{m^2}{b^2}}$ and a, b are the size of the sample. That is, $a = L_x$ and

$b = L_y$.

The general solutions to the PDE is obtained via Green's theorem

$$\Phi(\mathbf{x}) = \int_V \rho(\mathbf{x}') G(\mathbf{x}, \mathbf{x}') d^3 x' + \frac{1}{4\pi} \oint_S \left[G(\mathbf{x}, \mathbf{x}') \frac{\partial \Phi}{\partial n'}(\mathbf{x}') - \Phi(\mathbf{x}') \frac{\partial G(\mathbf{x}, \mathbf{x}')}{\partial n'}(\mathbf{x}') \right] da' \quad (10.15)$$

To solve for A_x , let $\Phi(\mathbf{x}) = A_x(\mathbf{x})$, and $\rho(\mathbf{x}) = \frac{d}{4\pi\kappa^2} \delta(z) j_x(x, y)$ from eq.(10.10). Then the volume integral in the Green's theorem (10.15) produces

$$A_x = \frac{d}{2ab\kappa^2} \sum_{l=-\infty}^{\infty} \sum_{m=-\infty}^{\infty} \frac{1}{\gamma_{lm}} C_{x,lm} e^{i\frac{2\pi l}{a}x} e^{i\frac{2\pi m}{b}y} e^{-\gamma_{lm}|z|}, \quad (10.16)$$

where l, m cannot be zero at the same time. The surface integral part in the Green's theorem, vanishes due to the periodic boundary condition of both \mathbf{A} and $G(\mathbf{x}, \mathbf{x}')$.

Similarly

$$A_y = \frac{d}{2ab\kappa^2} \sum_{l=-\infty}^{\infty} \sum_{m=-\infty}^{\infty} \frac{1}{\gamma_{lm}} C_{y,lm} e^{i\frac{2\pi l}{a}x} e^{i\frac{2\pi m}{b}y} e^{-\gamma_{lm}|z|}, \quad (10.17)$$

and

$$A_z = 0. \quad (10.18)$$

The Fourier coefficients $C_{x,lm}, C_{y,lm}$ are given by

$$C_{x,lm} = \int_{-\infty}^{\infty} \int_{-\infty}^{\infty} j_x(x, y) e^{-i\frac{2\pi l}{a}x} e^{-i\frac{2\pi m}{b}y} dx dy, \quad (10.19)$$

$$C_{y,lm} = \int_{-\infty}^{\infty} \int_{-\infty}^{\infty} j_y(x, y) e^{-i\frac{2\pi l}{a}x} e^{-i\frac{2\pi m}{b}y} dx dy. \quad (10.20)$$

The Fourier transform of the supercurrents (j_x, j_y) is done numerically by the well-known Fast Fourier Transform (FFT) algorithm discussed in the next chapter. When there are holes or the film is of variable thickness, they should be taken into account in the Fourier transform:

$$C_{x,lm} = \int_{-\infty}^{\infty} \int_{-\infty}^{\infty} d(x, y) j_x(x, y) e^{-i\frac{2\pi l}{a}x} e^{-i\frac{2\pi m}{b}y} dx dy, \quad (10.21)$$

$$C_{y,lm} = \int_{-\infty}^{\infty} \int_{-\infty}^{\infty} d(x, y) j_y(x, y) e^{-i\frac{2\pi l}{a}x} e^{-i\frac{2\pi m}{b}y} dx dy. \quad (10.22)$$

X.2. Magnetic dipole field

We need a mathematical model for an external magnetic source which is to create vortices by magnetic penetration (Fig. 12)

The magnetic field from a magnetic monopole is written as

$$\mathbf{H}_M(\mathbf{r}) = \frac{q_M}{r^2} \hat{\mathbf{e}}_r \quad (10.23)$$

Since $\mathbf{H}_M = \nabla \times \mathbf{A}_M$, we have to solve the differential equation

$$\nabla \times \mathbf{A}_M = \frac{q_M}{r^2} \hat{\mathbf{e}}_r \quad (10.24)$$

In the spherical coordinate system where $\mathbf{A}_M = A_r \hat{\mathbf{e}}_r + A_\theta \hat{\mathbf{e}}_\theta + A_\phi \hat{\mathbf{e}}_\phi$,

$$\nabla \times \mathbf{A}_M = \frac{1}{r^2 \sin \theta} \begin{vmatrix} \hat{\mathbf{e}}_r & r \hat{\mathbf{e}}_\theta & r \sin \theta \hat{\mathbf{e}}_\phi \\ \frac{\partial}{\partial r} & \frac{\partial}{\partial \theta} & \frac{\partial}{\partial \phi} \\ A_r & r A_\theta & r \sin \theta A_\phi \end{vmatrix} \quad (10.25)$$

Expanding the curl of \mathbf{A}_M above decomposes the eq.(10.24) into three equations as

$$\frac{1}{r^2 \sin \theta} \left[\frac{\partial}{\partial \theta} (r \sin \theta A_\phi) - \frac{\partial}{\partial \phi} (r A_\theta) \right] = \frac{q_M}{r^2} \quad (10.26)$$

$$\frac{\partial A_r}{\partial \phi} - \frac{\partial}{\partial r} (r \sin \theta A_\phi) = 0 \quad (10.27)$$

$$\frac{\partial}{\partial r} (r A_\theta) - \frac{\partial A_r}{\partial \theta} = 0 \quad (10.28)$$

The simplest solution for these PDE's is given in the spherical coordinate system as

$$\mathbf{A}_M(\mathbf{x}) = A_\phi(r, \theta) \hat{\mathbf{e}}_\phi = -\frac{q_M \cos \theta}{r \sin \theta} \hat{\mathbf{e}}_\phi \quad (10.29)$$

This expression has a singularity along the z-axis ($\theta = 0, \pi$). Anticipating the q_M be

placed above the film, we remove the singularity on the negative axis ($\theta = \pi$) as

$$A_\phi(r, \theta) = -\frac{q_M(1 + \cos \theta)}{r \sin \theta} \quad (10.30)$$

Thus the singularity on the negative axis below q_M is removed. To convert it to a Cartesian coordinate system, we notice the relationships

$$\hat{\mathbf{e}}_\phi = -\hat{\mathbf{e}}_x \sin \phi + \hat{\mathbf{e}}_y \cos \phi \quad (10.31)$$

and

$$r = \sqrt{(x - x_0)^2 + (y - y_0)^2 + (z - z_0)^2} \quad (10.32)$$

$$\cos \theta = \frac{z - z_0}{\sqrt{(x - x_0)^2 + (y - y_0)^2 + (z - z_0)^2}} \quad (10.33)$$

$$\sin \theta = \frac{\sqrt{(x - x_0)^2 + (y - y_0)^2}}{\sqrt{(x - x_0)^2 + (y - y_0)^2 + (z - z_0)^2}} \quad (10.34)$$

$$\cos \phi = \frac{x - x_0}{\sqrt{(x - x_0)^2 + (y - y_0)^2}} \quad (10.35)$$

$$\sin \phi = \frac{y - y_0}{\sqrt{(x - x_0)^2 + (y - y_0)^2}} \quad (10.36)$$

$$(10.37)$$

with the origin at an arbitrary point (x_0, y_0, z_0) . Thus the gauge is given by

$$\mathbf{A}_M = A_x \hat{\mathbf{e}}_x + A_y \hat{\mathbf{e}}_y \quad (10.38)$$

where

$$A_x(x, y, z) = \frac{q_M \left(\sqrt{(x - x_0)^2 + (y - y_0)^2 + (z - z_0)^2} + z - z_0 \right) (y - y_0)}{\sqrt{(x - x_0)^2 + (y - y_0)^2 + (z - z_0)^2} [(x - x_0)^2 + (y - y_0)^2]} \quad (10.39)$$

$$A_y(x, y, z) = -\frac{q_M \left(\sqrt{(x-x_0)^2 + (y-y_0)^2 + (z-z_0)^2} + z - z_0 \right) (x-x_0)}{\sqrt{(x-x_0)^2 + (y-y_0)^2 + (z-z_0)^2} [(x-x_0)^2 + (y-y_0)^2]} \quad (10.40)$$

This form is more convenient for programming.

The vector potential for the magnetic dipole ($q_M, -q_M$) is the superposition of the two vector potentials of opposite charges which are at a variable distance apart from each other. In our simulation, we use a dipole located along the z-axis normal to the film plane (xy-plane), thus we put a monopole and an antimonopole at (x_0, y_0, z_1) and (x_0, y_0, z_2) , respectively. Then the gauge should be

$$A_x(x, y, z) = \frac{q_M \left(\sqrt{(x-x_0)^2 + (y-y_0)^2 + (z-z_1)^2} + z - z_1 \right) (y-y_0)}{\sqrt{(x-x_0)^2 + (y-y_0)^2 + (z-z_1)^2} [(x-x_0)^2 + (y-y_0)^2]} \quad (10.41)$$

$$-\frac{q_M \left(\sqrt{(x-x_0)^2 + (y-y_0)^2 + (z-z_2)^2} + z - z_2 \right) (y-y_0)}{\sqrt{(x-x_0)^2 + (y-y_0)^2 + (z-z_2)^2} [(x-x_0)^2 + (y-y_0)^2]} \quad (10.42)$$

$$A_y(x, y, z) = -\frac{q_M \left(\sqrt{(x-x_0)^2 + (y-y_0)^2 + (z-z_1)^2} + z - z_1 \right) (x-x_0)}{\sqrt{(x-x_0)^2 + (y-y_0)^2 + (z-z_1)^2} [(x-x_0)^2 + (y-y_0)^2]} \quad (10.43)$$

$$+\frac{q_M \left(\sqrt{(x-x_0)^2 + (y-y_0)^2 + (z-z_2)^2} + z - z_2 \right) (x-x_0)}{\sqrt{(x-x_0)^2 + (y-y_0)^2 + (z-z_2)^2} [(x-x_0)^2 + (y-y_0)^2]} \quad (10.44)$$

Note that the periodic boundary conditions imply the periodicity of not only the superconductor, but also of the magnetic dipole lattice (see Fig.17). The vector potential for this periodic array of dipoles is

$$A_x^P(x, y, z) = \sum_{m=-M}^M \sum_{n=-N}^N A_x(x, y, z; x_m, y_n) \quad (10.45)$$

$$A_y^P(x, y, z) = \sum_{m=-M}^M \sum_{n=-N}^N A_y(x, y, z; x_m, y_n) \quad (10.46)$$

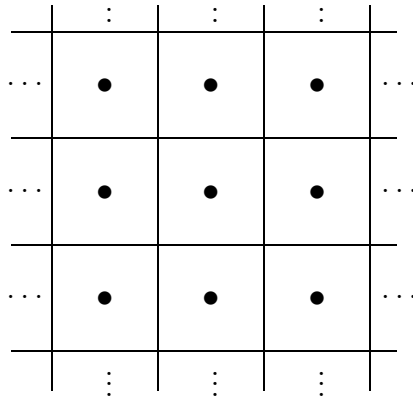


Fig. 17. A periodic array of the systems. In each system, a magnetic dipole is located above the center of each block of the sample, which is in a periodic array by itself.

where

$$A_x(x, y, z; x_m, y_n) = \frac{q_M \left(\sqrt{(x-x_m)^2 + (y-y_n)^2 + (z-z_1)^2} + z - z_1 \right) (y-y_n)}{\sqrt{(x-x_m)^2 + (y-y_n)^2 + (z-z_1)^2} [(x-x_m)^2 + (y-y_n)^2]} \quad (10.47)$$

$$- \frac{q_M \left(\sqrt{(x-x_m)^2 + (y-y_n)^2 + (z-z_2)^2} + z - z_2 \right) (y-y_n)}{\sqrt{(x-x_m)^2 + (y-y_n)^2 + (z-z_2)^2} [(x-x_m)^2 + (y-y_n)^2]} \quad (10.48)$$

$$A_y(x, y, z; x_m, y_n) = - \frac{q_M \left(\sqrt{(x-x_m)^2 + (y-y_n)^2 + (z-z_1)^2} + z - z_1 \right) (x-x_m)}{\sqrt{(x-x_m)^2 + (y-y_n)^2 + (z-z_1)^2} [(x-x_m)^2 + (y-y_n)^2]} \quad (10.49)$$

$$+ \frac{q_M \left(\sqrt{(x-x_m)^2 + (y-y_n)^2 + (z-z_2)^2} + z - z_2 \right) (x-x_m)}{\sqrt{(x-x_m)^2 + (y-y_n)^2 + (z-z_2)^2} [(x-x_m)^2 + (y-y_n)^2]} \quad (10.50)$$

Here $M, N \rightarrow \infty$ for the definition of array, but in practice we should use a finite number of dipoles. We have used $M = N = 24$. So there are 49×49 pieces of the sample in the array, and we solve for the sample at the center.

CHAPTER XI

SOLUTION METHOD

XI.1. Discretization of Ginzburg-Landau equation

To solve the system of equations above, we obtain a time-dependent equation for Ψ for relaxation method as before, *i.e.* $\frac{\partial \Psi}{\partial t} = -\frac{\partial G}{\partial \Psi^*}$, and use the link variable approach. [58]

Following the same procedure as eq.(6.15), the semi-discrete equation is

$$\begin{aligned} \frac{\partial \Psi_P}{\partial t} = & h_x h_y \left[\frac{d_w (e^{\iota A_w h_x} \Psi_W - \Psi_P) + d_e (e^{-\iota A_e h_x} \Psi_E - \Psi_P)}{h_x^2} \right. \\ & \left. + \frac{d_s (e^{\iota B_s h_y} \Psi_S - \Psi_P) + d_n (e^{-\iota B_n h_y} \Psi_N - \Psi_P)}{h_y^2} \right] \\ & + h_x h_y d_p (1 - |\Psi_P|^2) \Psi_P \end{aligned} \quad (11.1)$$

with

$$j_{xe} = \frac{1}{h_x} [(\Phi_P \Theta_E - \Theta_P \Phi_E) \cos(A_e h_x) - (\Phi_P \Phi_E + \Theta_P \Theta_E) \sin(A_e h_x)] \quad (11.2)$$

$$j_{yn} = \frac{1}{h_y} [(\Phi_P \Theta_N - \Theta_P \Phi_N) \cos(B_n h_y) - (\Phi_P \Phi_N + \Theta_P \Theta_N) \sin(B_n h_y)] \quad (11.3)$$

The periodic boundary conditions for Ψ have the form

$$\Psi(x + L_x) = \Psi(x) \quad (11.4)$$

$$\Psi(y + L_y) = \Psi(y) \quad (11.5)$$

For numerical implementation of periodic boundary conditions, see e.g. Roache [79]

The vector potential is obtained from the Fast Fourier transform technique. A 64×64 staggered grid is used with the spatial increments $h_x = h_y = 0.25$ and the time step $\Delta t = 0.05$. In addition, the local thickness $d(i, j) = 0$ at all the nodes (i, j) ,

where the antidots occupy.

XI.2. Discretized solutions for magnetic potential \mathbf{A}

The discretized solution for \mathbf{A} is obtained as

$$A_{xe} = \frac{d}{2ab\kappa^2} \sum_{l=0}^{2l_{max}-1} \sum_{m=0}^{2m_{max}-1} \frac{1}{\gamma_{lm}} C_{xe,lm} e^{i\frac{2\pi l}{a}x} e^{i\frac{2\pi m}{b}y} e^{-\gamma_{lm}|z|}, \quad (11.6)$$

$$A_{yn} = \frac{d}{2ab\kappa^2} \sum_{l=0}^{2l_{max}-1} \sum_{m=0}^{2m_{max}-1} \frac{1}{\gamma_{lm}} C_{yn,lm} e^{i\frac{2\pi l}{a}x} e^{i\frac{2\pi m}{b}y} e^{-\gamma_{lm}|z|}, \quad (11.7)$$

where l, m cannot be zero at the same time, and $2l_{max} - 1 = N_x$ and $2m_{max} - 1 = N_y$. These expressions are still complex, and we take the real part of the final results. The discretized forms of eqs. (10.20, 10.20) are

$$C_{xe,lm} = \sum_{l=0}^{2l_{max}-1} \sum_{m=0}^{2m_{max}-1} j_{xe} e^{-i\frac{2\pi l}{a}x} e^{-i\frac{2\pi m}{b}y}, \quad (11.8)$$

$$C_{yn,lm} = \sum_{l=0}^{2l_{max}-1} \sum_{m=0}^{2m_{max}-1} j_{yn} e^{-i\frac{2\pi l}{a}x} e^{-i\frac{2\pi m}{b}y}. \quad (11.9)$$

XI.3. Two-dimensional fast Fourier transform in parallel computers

To evaluate the Fourier coefficients $C_{xe,lm}$ and $C_{yn,lm}$ above, we use the Fast Fourier Transform (FFT) technique.

For one-dimensional case, the discrete Fourier Transform ¹ is given as

$$H_n \equiv \sum_{k=0}^{N-1} h_k e^{2\pi i k n / N} = \sum_{k=0}^{N-1} h_k W^{nk} \quad (11.11)$$

¹If the set of sampling points is large enough, this discrete Fourier series can approximate the continuous Fourier transform:

$$H(f_n) = \int_{-\infty}^{\infty} h(t) e^{2\pi i f_n t} dt \approx \sum_{k=0}^{N-1} h_k e^{2\pi i k n / N} \Delta t = (\Delta t) \cdot H_n \quad (11.10)$$

with the inverse Fourier Transform

$$h_k = \frac{1}{N} \sum_{n=0}^{N-1} H_n e^{-2\pi i k n / N} \quad (11.12)$$

This series can be rearranged² to results in the efficient algorithm of FFT by observing

$$\begin{aligned} F_k &= \sum_{j=0}^{N-1} e^{2\pi i j k / N} f_j \\ &= \sum_{j=0}^{N/2-1} e^{2\pi i k (2j) / N} f_{2j} + \sum_{j=0}^{N/2-1} e^{2\pi i k (2j+1) / N} f_{2j+1} \\ &= \sum_{j=0}^{N/2-1} e^{2\pi i k j / (N/2)} f_{2j} + W^k \sum_{j=0}^{N/2-1} e^{2\pi i k j / (N/2)} f_{2j+1} \\ &= F_k^e + W^k F_k^o \end{aligned} \quad (11.13)$$

So we have divided the FFT into two FFTs in each the half data sets of the original data. If $N = 2^n$, we can keep doing this process until we subdivide the original data all the way down to transforms of length 1. Note the Fourier transform of this data of length one is just itself. That is, after n recursive subdivision into even and odd intervals, we have a one-point transform that is just one of the input numbers f_n :

$$F_k^{eoeoeo \dots oee} = f_n \quad (11.14)$$

Then we have only two tasks left: (1) Finding the even-odd subdivision sequence ($eoeoeo \dots oee$) for each input data (for each n). This is easily done by expressing the the even-odd subdivision sequence in binary number, as $e = 0$ and $o = 1$. This idea is called *bit reversal*. (2) Multiplying out the W^k having occurred in each stage of the subdivision sequentially. This results in the famous Cooley-Tukey algorithm. If we change the order of the steps (1) and (2), it becomes Sande-Tukey algorithm. [47]

²Sometimes this is called *Danielson-Lanczos Lemma*.

In our study the supercurrents $\mathbf{j}(\mathbf{x}) = (j_x(x, y), j_y(x, y))$ need to be Fourier transformed to obtain the magnetic potential. Here we have two-dimensional Fourier transform in x and y . The two-dimensional Fourier transform can be viewed as two successive one-dimensional transforms. [80] That is,

$$\begin{aligned} H(u, v) &= \int_{-\infty}^{\infty} \int_{-\infty}^{\infty} h(x, y) e^{-j2\pi(ux+vy)} dx dy \\ &= \int_{-\infty}^{\infty} e^{-j2\pi vy} \left[\int_{-\infty}^{\infty} h(x, y) e^{-j2\pi ux} dx \right] dy \\ &= \int_{-\infty}^{\infty} Z(u, y) e^{-j2\pi vy} dy \end{aligned} \quad (11.15)$$

where we have denoted the term in brackets by $Z(u, y)$.

$$\begin{aligned} H(n/NT_x, m/MT_y) &= \sum_{q=0}^{M-1} \left[\sum_{p=0}^{N-1} h(pT_x, qT_y) e^{-j2\pi np/N} \right] e^{-j2\pi mq/M} \\ &= \sum_{q=0}^{M-1} Z(n/NT_x, qT_y) e^{-j2\pi mq/M} \end{aligned} \quad (11.16)$$

Since a two-dimensional FFT is just two one-dimensional FFT, the two-dimensional data array (matrix) needs to be FFT'ed in both of row and column direction. The well-known Cooley-Tukey algorithm is employed for each rowwise FFT. Once FFT is done in every row, the data matrix is transposed and again rowwise FFT is performed. One convenient thing is that the transpose operation is a built-in command in Fortran 90. In this sense, Fortran 90 is a programming language well suited for parallelism. [81]

Due to the still severe amount of computation, a parallel computation is implemented using OpenMP directives [82, 83] in a 128-processor supercomputer in Texas A&M University.

CHAPTER XII

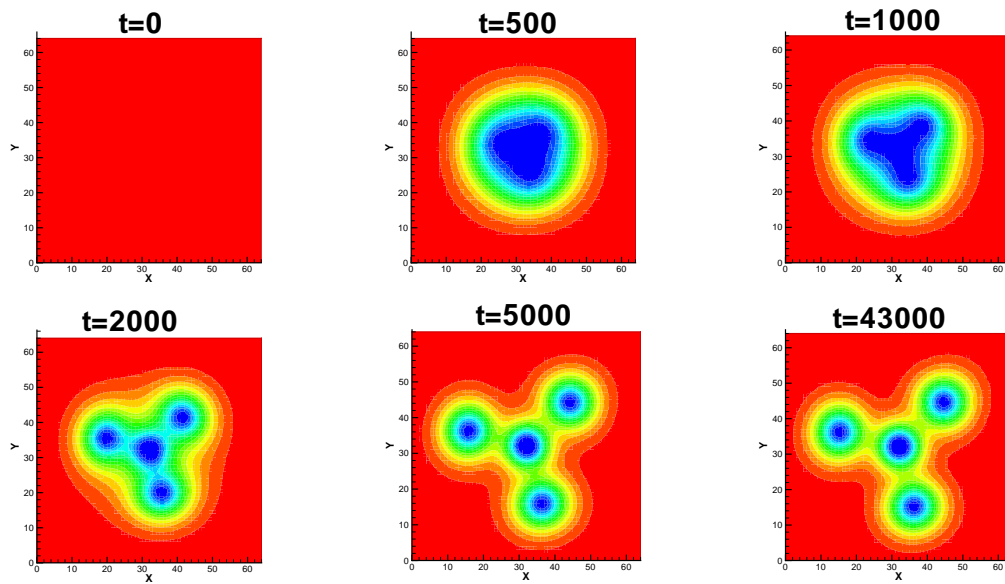
SIMULATION RESULTS

In this chapter, a variety of simulations of magnetic penetrations and relaxations are presented.

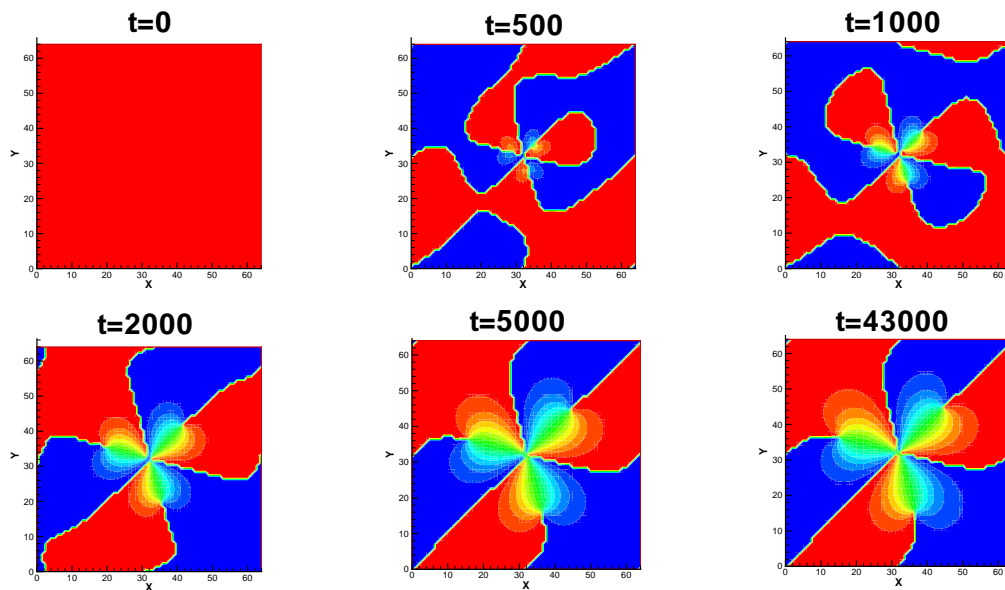
XII.1. Magnetic penetration in a film of constant thickness

In this section we present the simulation of the magnetic penetration process of vortices into the film. When a magnetic tip (dipole) is located above the film, the stray field from the tip passing through the film creates the vortex-antivortex pairs. The magnetic flux $\Phi = \int_{S_{film}} \mathbf{H} \cdot \mathbf{n} d\sigma$, applied onto the film by the dipole, is calculated by numerical integration of the magnetic field passing through the film plane. Since the magnetic field lines change their polarity passing through the film, the total flux penetrating the film is zero. However, by calculating Φ^+ and Φ^- , (in units of $\Phi_0 \equiv hc/2e$) by integrating the positive and negative values of magnetic field (z-component) separately, we can have some idea of how many vortex-antivortex pairs the dipole attempts to create in the sample.

Figure 18 is a demonstration of magnetic penetrations onto the thin film with thickness $d_f = 0.1$, under the external magnetic field imposed by a dipole above, along the axis through the center of the film. The dipole consists of two magnetic charges of opposite sign, i.e. $q_{M_1} = 8$ and $q_{M_2} = -8$, displaced in $d_l = 2.3$, which is slightly larger than penetration depth $\lambda(=2.0)$, since we here assumed $\kappa = 2$ and all lengths are in units of ξ . q_{M_1} is located at $z_M = 0.85$, which is 0.8ξ above the film surface and q_{M_2} is farther away by d_l . The film carries three vortex-antivortex pairs. The antivortices are located together around the center, while vortices spread outward repelling each other. This can be seen more clearly through the plots of the



(a) superelectron density



(b) phase of order parameter

Fig. 18. The magnetic penetration into a film with no pins in it, under the external field from a magnetic dipole. (a) The evolution of the superelectron density. (b) The corresponding evolution of phase of the order parameter. The film size is $L_x \times L_y = 16\xi \times 16\xi$, and thickness $d_f = 0.1\xi$. Here $\Phi^+ = 2.90$ and the film carries three vortex-antivortex pairs in the steady state.

phase of the order parameter. There is a 2π variation of phase around a vortex and so is antivortex, only in the opposite direction. The phase plots show clearly that the vortices and antivortices are paired one by one. The flux sent by the dipole through the sample is calculated $\Phi^+ = 2.90$ and the return flux antivortices $\Phi^- = -2.92$. The error of about 7% between Φ^+ and Φ^- is due to discretization, the fact we cannot make the system perfectly periodic, since a perfectly periodic array of dipole require an infinite number of dipoles. However, in the lower values of Φ^+ the errors fall sharply below 1%. For example, for $\Phi^+ = 1.90$ case which is used in the majority of simulations in the following, the difference between Φ^+ and Φ^- is 0.6%.

Milošević and Peeters [64] suggested that the number of vortex-antivortex pairs increase based on a non-integral increment of magnetic flux $\Delta\Phi = 1.073$ in units of Φ_0 in their simulation of a film with a ferromagnetic dot of finite radius. The ferromagnetic dot is right on top of their film (although insulated with a thin layer of oxide) imposing a dipole magnetic field. In our simulation we use a different kind of dipole, consisting of two magnetic charges. This corresponds to an extremely thin magnetic tip, and produces highly focused magnetic field.

In our simulations, no vortex-antivortex pairs are created in the film for imposed fluxes up to $\Phi^+ = 2.15$ shown in Fig. 19 (a) and (d). A large area on the film becomes non-superconducting, nevertheless no vortex-antivortex pairs are formed. For $\Phi^+ = 2.90$ we have three pairs (Fig. 19 (c) and (f)), and in $2.15 < \Phi^+ < 2.90$ we have two pairs of vortex-antivortex (Fig. 19 (b) and (e)). So it seems that a single pair of vortex-antivortex is not favorable for this square film geometry.

In Fig. 20 two vortex-antivortex pairs are formed at $\Phi^+ = 2.49$. Interestingly, there are created three vortex-antivortex pairs initially. Afterwards a pair of vortex-antivortex annihilate each other and two pairs remain in the steady state. This is more discernable in the phase plots. This “partial annihilation” happens to all two-

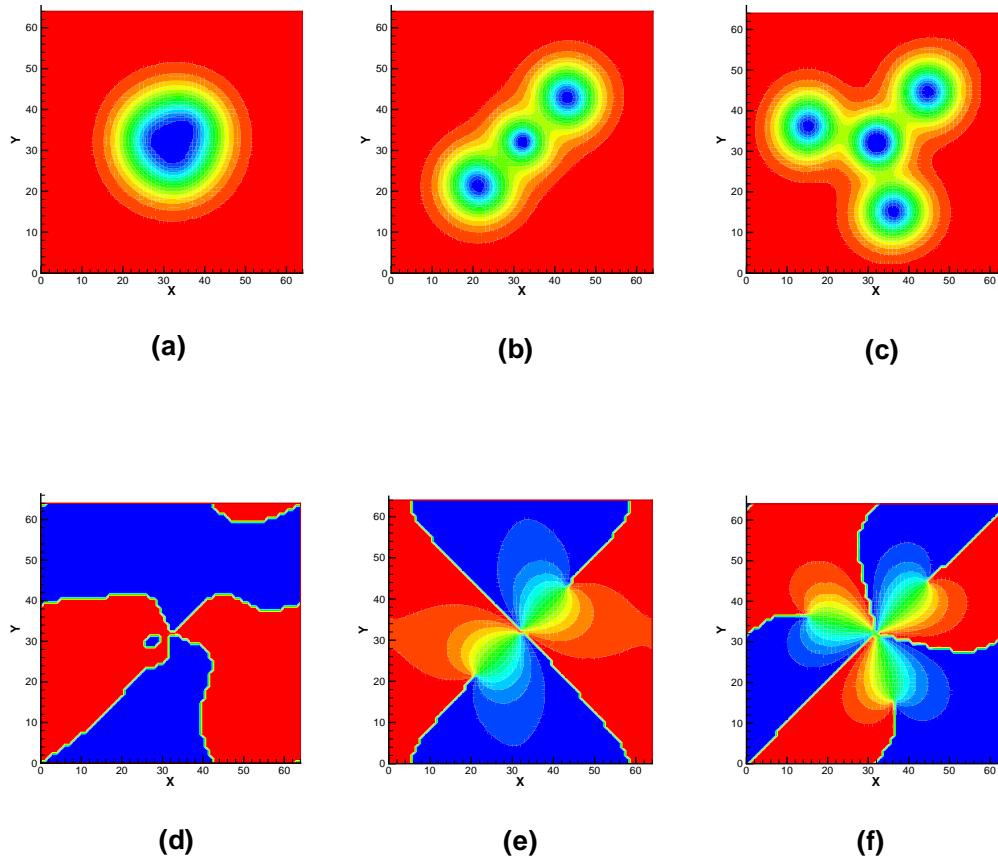
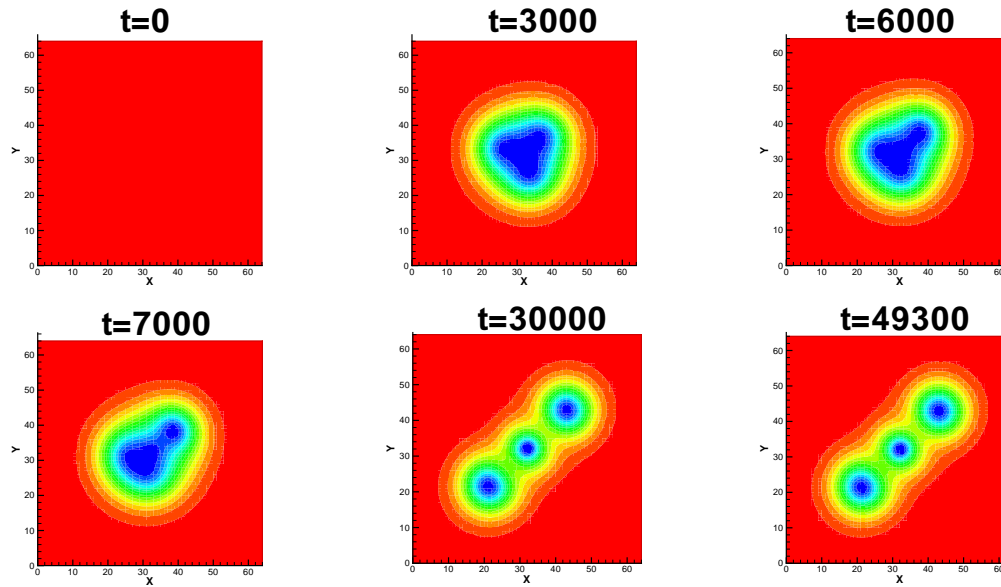
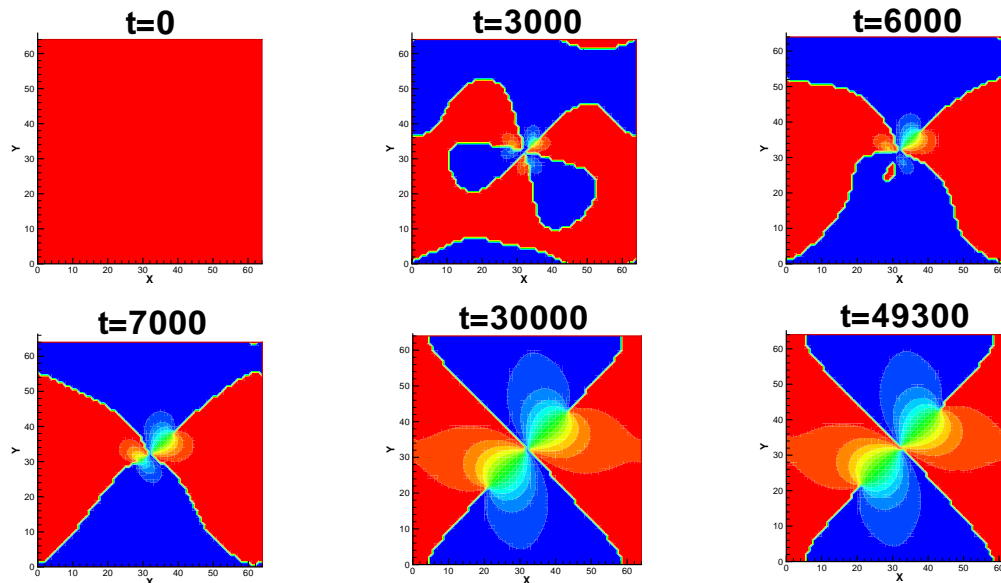


Fig. 19. The steady-states of magnetic penetration into the film with no pins under the external field from a magnetic dipole. Top row is the evolution of the superelectron density, bottom row the corresponding evolution of phase of the order parameter. The film is of the same size and thickness as in Fig. 18. Here $\Phi^+ = 2.15$ for (a) and (d), $\Phi^+ = 2.50$ for (b) and (e), and $\Phi^+ = 2.90$ for (c) and (f). It is found that in the interval $2.15 < \Phi^+ < 2.90$ the film carries two vortex-antivortex pairs in the steady state.



(a) superelectron density



(b) phase of order parameter

Fig. 20. A magnetic penetration into the film with no pins under the external field from a magnetic dipole. (a) The evolution of the superelectron density. (b) The corresponding evolution of the phase of the order parameter. The film is of the same size and thickness as in Fig. 18. Here $\Phi^+ = 2.49$ is in the interval $2.15 < \Phi^+ < 2.90$ discussed in Fig. 19. three vortex-antivortex pairs initially appear in the film early ($t=3000$), then one pair annihilates itself ($t=6000$ and 7000). This process is more discernible in the phase plot. Finally the film carries two vortex-antivortex pairs in the steady state.

pair cases tried, i.e. for $\Phi^+ = 2.49, 2.58, 2.62, 2.65, 2.68, 2.74, 2.80$. Exception is the case for $\Phi^+ = 2.20$. In that case the film carried two pairs all throughout, suggesting that it is on the border between the range in Φ^+ where no vortex is created and the range of Φ^+ for two-pair creation. This 3-pair-to-2-pair transition by “partial annihilation” suggests that the magnetic field adjust itself to obtain equilibrium by controlling vortices, in their movement and annihilation. It seems that here the system is “contemplating” for which one to select from one pair, two pairs, or three vortex-antivortex pairs.

XII.2. Magnetic penetration in a film with pins

In this section we explore the possibility to control the magnetic penetration process in the film. Previous section showed that the film does not carry a single pair of vortex-antivortex. When a pair of antidots (holes) is introduced into the film, a pair of vortex-antivortex can be created and pinned at the holes. Here we use a square pin clipped at its corners, making an octagonal shape. By this we create an approximately round pin, and the “approximate diameter” is measured by the distance between the sides facing each other, not by a vertex-to-vertex distance. In Fig. 21 in the following, a film is initially in the Meissner state but with two holes. The dipole field creates a pair of vortex and antivortex around the center of the film. The figure shows the process a vortex is attracted by the pin while outside, move toward, and get pulled into the hole in the end. While the antivortex stay in the central area, pinned by another antidot closer to the center. Final state has a vortex and an antivortex, each of which is pinned at an antidot. Note the vortex pair was created at $\Phi^+ = 1.90$, in the region where no vortex was created in the film without holes. So here the pins are playing a role of perturbation breaking the geometric symmetry of the system,

enabling the system to seek an equilibrium at the lower energy. We have obtained the vortex-antivortex pair down to $\Phi^+ = 1.3$.

Comparison of the Fig. 21 above with Fig. 22 in the following, shows the vortices are pulled into bigger holes faster. So the bigger holes attract the vortices with stronger force.

Figure 23 shows that the external field is controlling the position of vortices. In (a) and (b) there are two antidots of an approximate diameter 2ξ , centered at the nodes $(i_{p_1}, j_{p_1}) = (28, 28)$ and $(i_{p_2}, j_{p_2}) = (45, 45)$ each, while in (c) and (d) the antidots of the same size are at the nodes $(i_{p_1}, j_{p_1}) = (29, 29)$ and $(i_{p_2}, j_{p_2}) = (46, 46)$. Note that the distance between the pins in these two cases is the same. That is, for the spatial increments $h_x = h_y = 0.25\xi$ on the grid,

$$d(p_1, p_2) = \sqrt{(i_{p_1} - i_{p_2})^2 h_x^2 + (j_{p_1} - j_{p_2})^2 h_y^2} \simeq 6\xi \quad (12.1)$$

for both cases. In the steady state, in (a),(b) the antivortex stays on the edge of the pin at (28,28) without being pulled further. On the other hand in (c) and (d) both vortices are fully pulled into the pins. In (e) and (f), the pins of bigger size (approximate diameter 2.5ξ) are located at (28,28) and (44,44). It is clear the antivortex is not fully pulled into the pin at (28,28).

The above results suggest that the curvature of the dipole field is strongly influencing the positions of vortices. This is already clear from Fig. 13. The film is soaked in the magnetic field from the dipole and the vortices created should stay in the field. There exists the locations and distances of vortices that the external field “prefer.” Thus there should exist an optimal configuration of pin locations for the best pinning of vortices. For $\Phi^+ = 1.90$ we believe (29,29) and (44,44) is the pin location that vortices are fully pulled into the pin. However, as will be seen below, this optimal configuration of pins is not enough for pinning without an aiding external magnetic

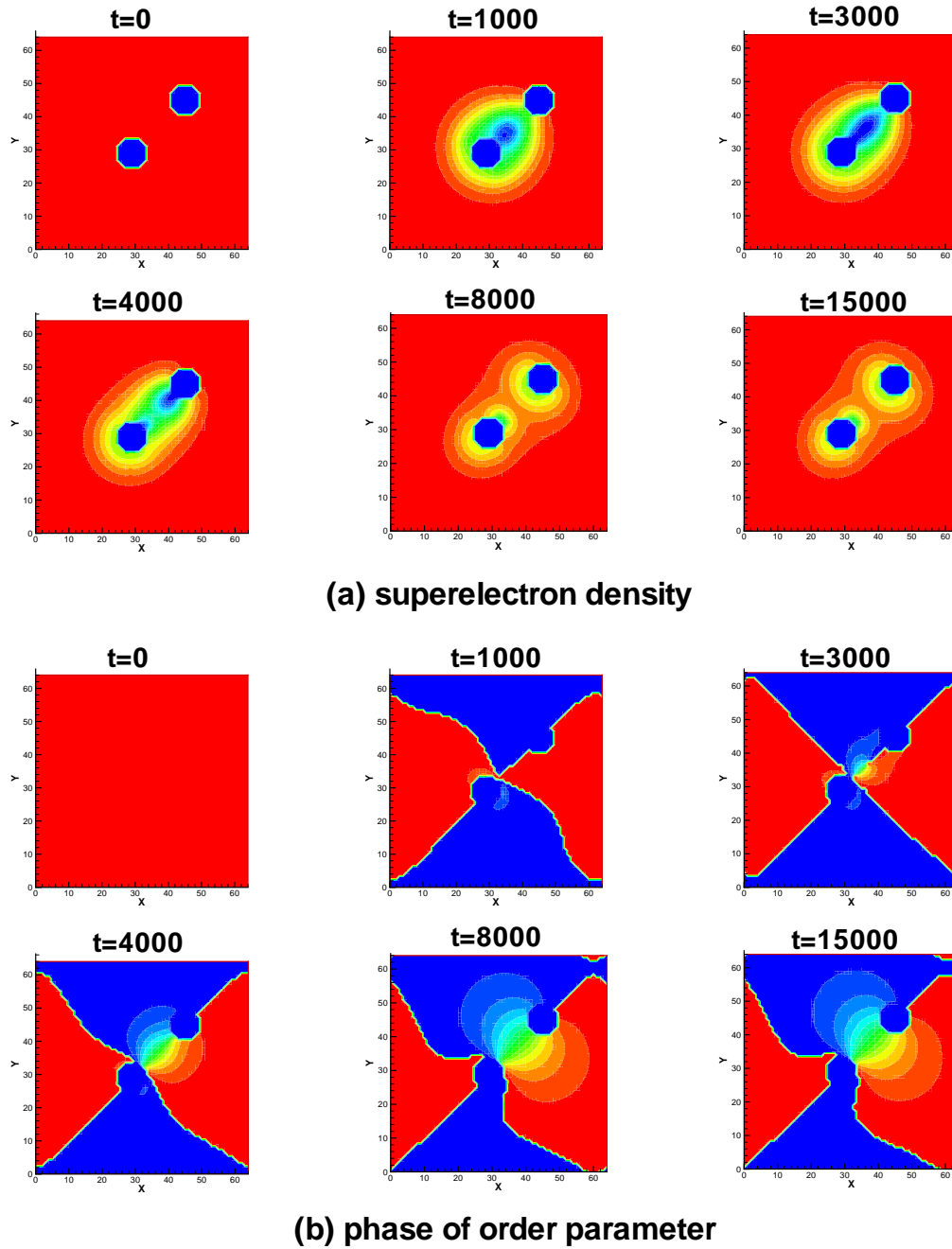


Fig. 21. The magnetic penetration into the film with two pins under the external field from a magnetic dipole. The dipole provides the magnetic flux $\Phi^+ = 1.90$. (a) The evolution of the superelectron density. (b) The corresponding evolution of the phase of the order parameter. The film is of the same size and thickness as in Fig. 18. The film center is at the node $(32,32)$. There are two antidots of an approximate diameter 2ξ , centered at the nodes $(29,29)$ and $(45,45)$ respectively. In the steady state there is a pair of vortex-antivortex caught at the pins.

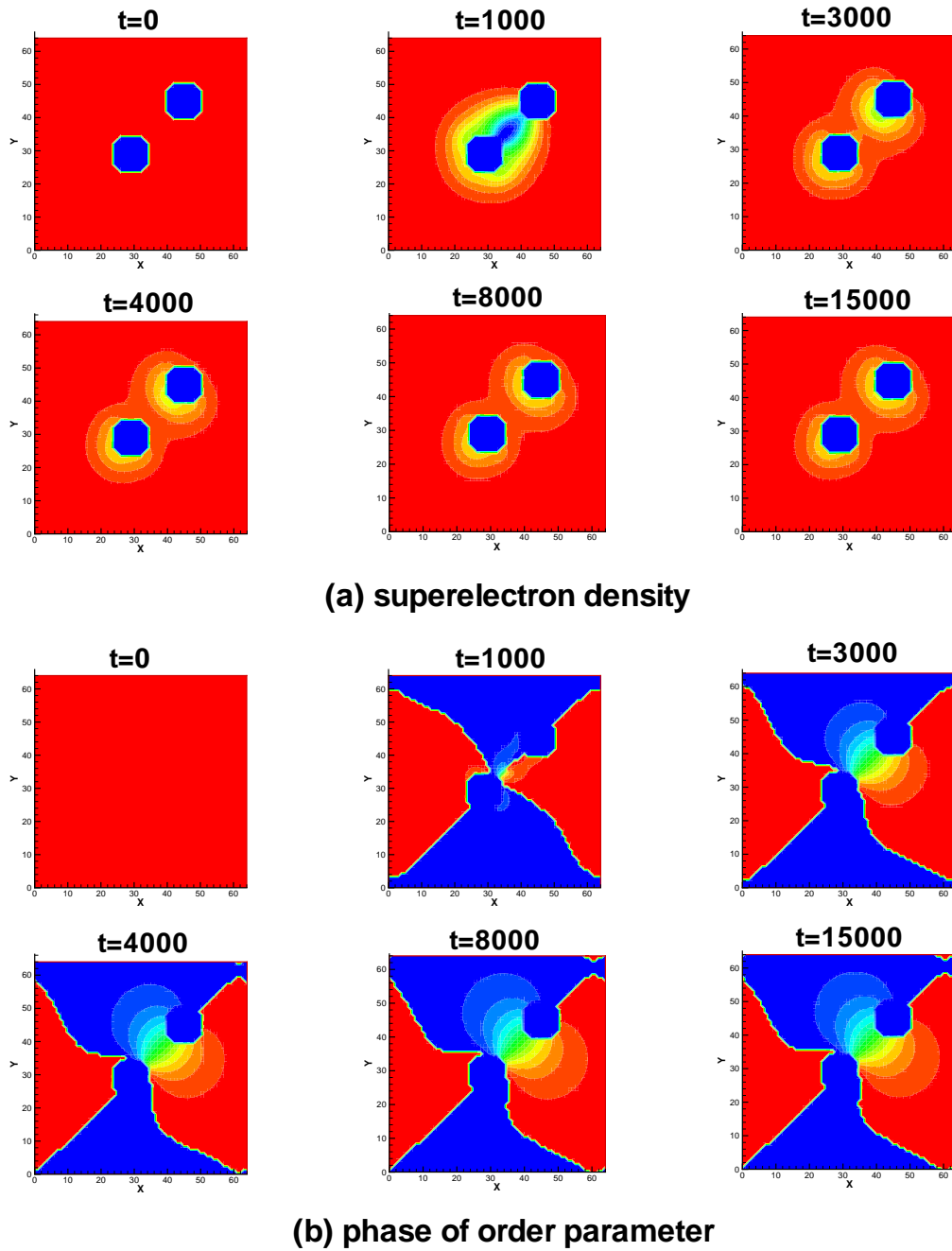


Fig. 22. The magnetic penetration into the film with two larger pins under the external field from a magnetic dipole. (a) The evolution of the superelectron density. (b) The corresponding evolution of the phase of the order parameter. The two antidots have an approximate diameter 2.5ξ and the other parameters are the same as Fig. 21. In the steady state there is a pair of vortex-antivortex caught at the pins.

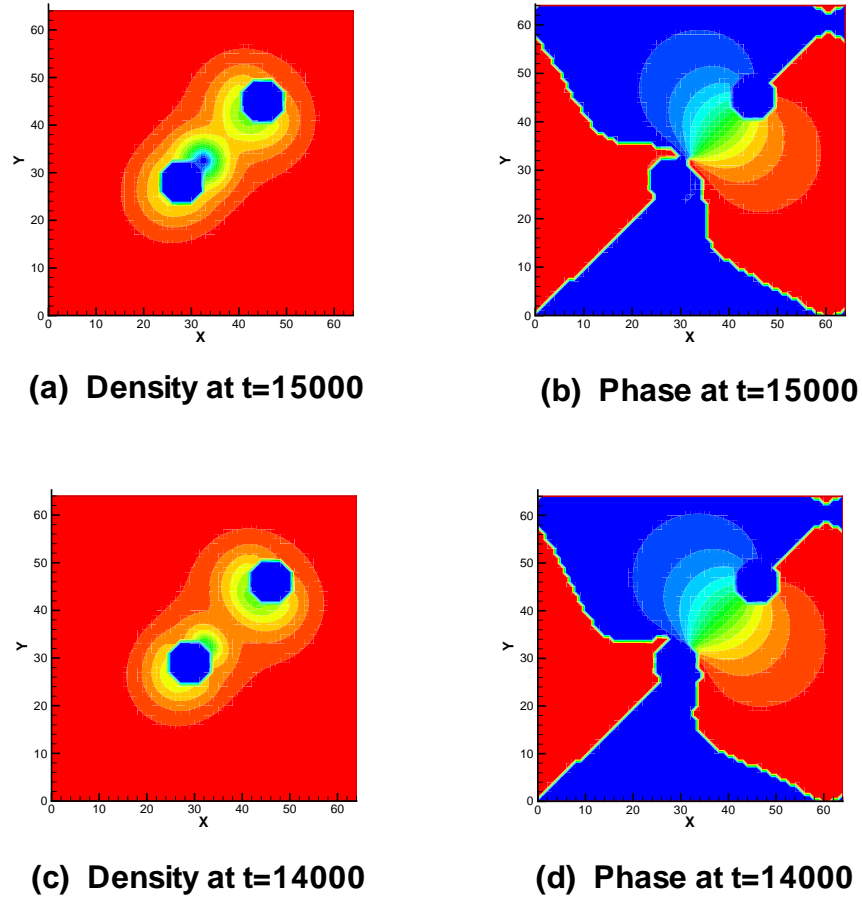
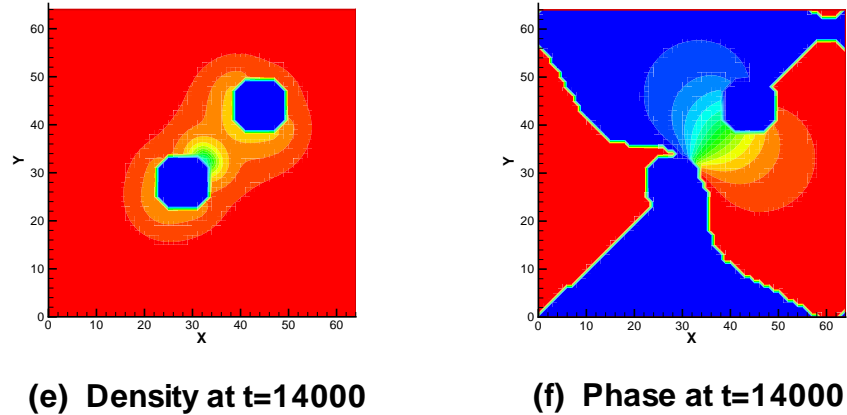


Fig. 23. The steady-states of magnetic penetrations into the film with two pins, under the external field from a magnetic dipole. The film is of the same size and thickness as Fig.21. Here again $\Phi^+ = 1.90$. In (a) and (b) there are two antidots of an approximate diameter 2ξ , centered at the nodes (28,28) and (45,45). In the steady state the antivortex stays on the edge of the pin at (28,28) without being pulled further into the pin. In (c) and (d), where the antidots are at nodes (29,29) and (46,46), both vortices are pulled well into the pins. In (e) and (f), pins of bigger size (approximate diameter 2.5ξ) are located at (28,28) and (44,44). It is clear the antivortex is not fully pulled into the pin at (28,28).

Fig. 23 (*cont.*)

field.

From the strong influence of the external magnetic field, it is not surprising the pinning is greatly weakened when the external magnetic field is removed. Figure 24 shows a magnetic relaxation process *with the external magnetic field removed (turned off)*, starting from an initial vortex state with a pair of vortex-antivortex pinned found previously for $\Phi^+ = 1.90$. There are two antidots of an approximate diameter 2.5ξ , centered at the nodes (29,29) and (45,45). The vortex and antivortex are found to come out of the pins and annihilate each other quickly.

XII.2.1. The effect of artificial vortex method

In Fig. 25 is presented the time sequences of two magnetic penetrations into a film with two antidots of an approximate diameter 2.5ξ , centered at nodes (29,29) and (44,44) each, with $\Phi^+ = 1.90$. In (a), the magnetic penetration starting with the Meissner state results in a steady state with a pair of vortex-antivortex caught at the pins. In (b) The magnetic penetration starts with a pair of artificial vortex and antivortex instead of the Meissner state as in (a). The result is the same steady state

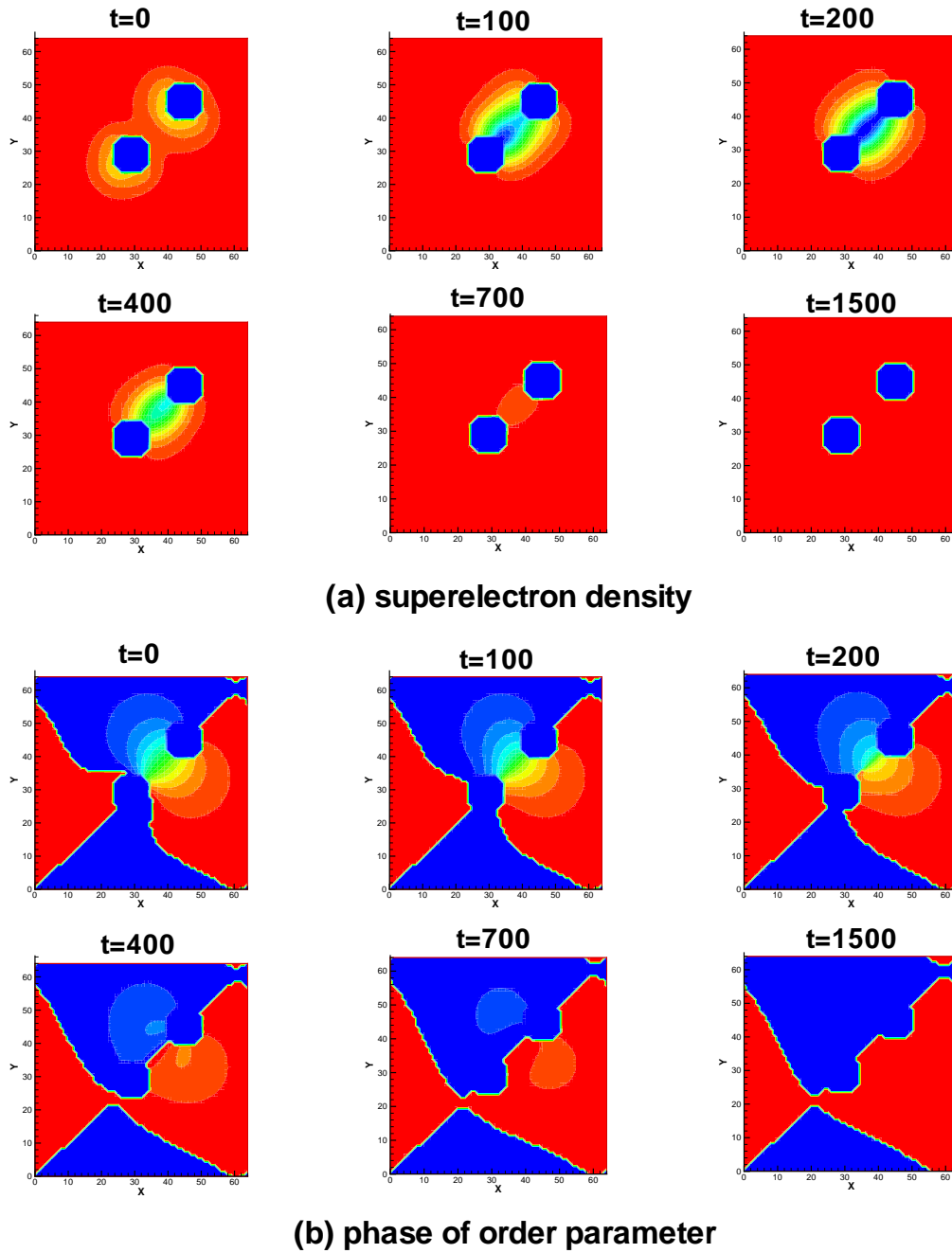


Fig. 24. A magnetic relaxation process *with the external magnetic field removed (turned off)* from an initial vortex state with a pair of vortex-antivortex inside the pins. The film thickness is $d_f = 0.1$. There are two antidots of an approximate diameter 2.5ξ , centered at nodes $(29,29)$ and $(45,45)$. The vortex and antivortex are found to come out of the pins and annihilate each other quickly.

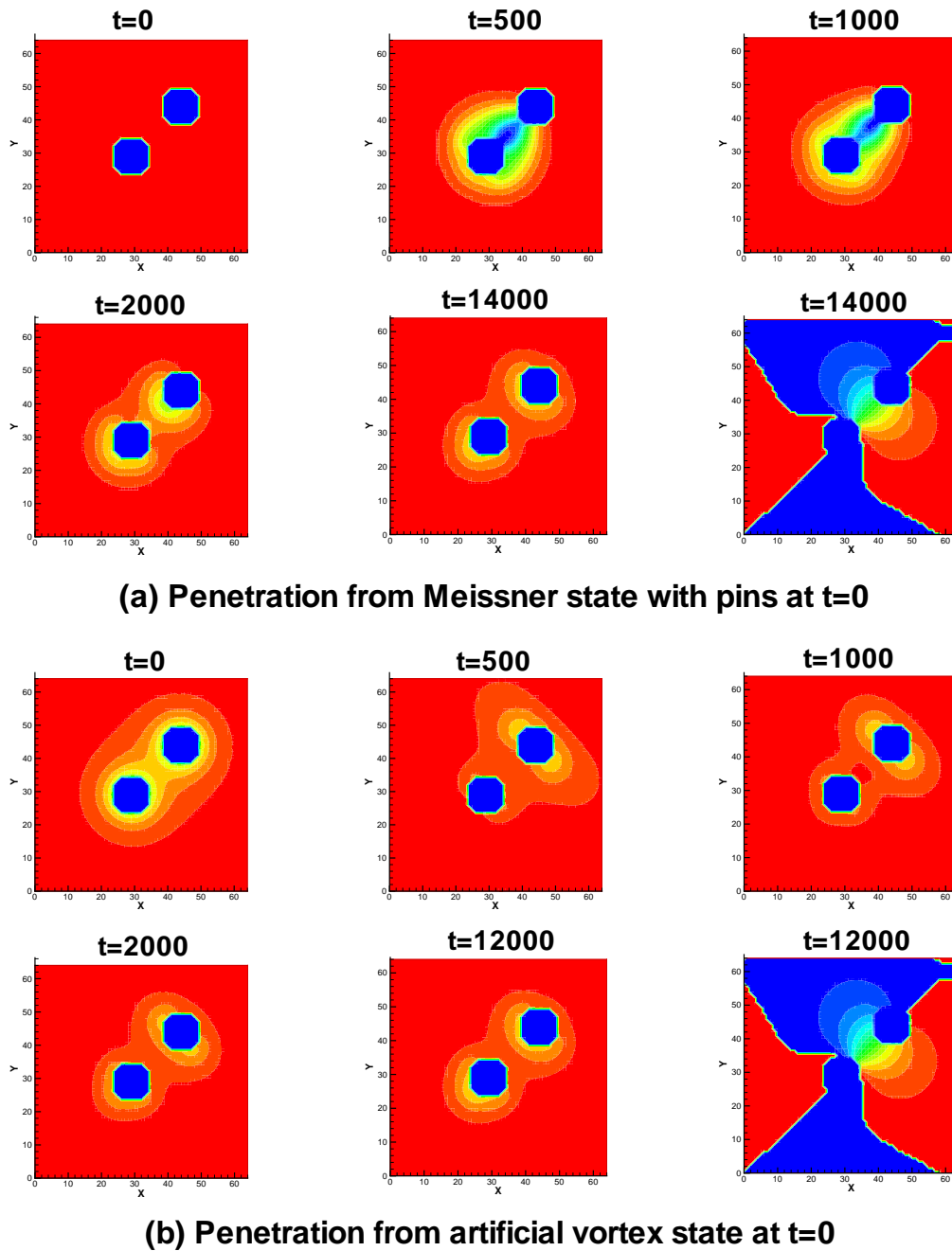


Fig. 25. Pseudo-time sequences of two cases of magnetic penetration into a film with thickness $d_f = 0.1$ with two antidots of an approximate diameter 2.5ξ , centered at nodes $(29, 29)$ and $(44, 44)$, and $\Phi^+ = 1.90$. (a) The magnetic penetration starting with the Meissner state results in a steady state with a pair of vortex-antivortex caught at the pins. (b) The magnetic penetration starts with a pair of artificial vortex and antivortex inside the pins instead of the Meissner state as in (a). The result is the same steady state with a pair of vortex-antivortex caught at the pins, which is achieved in a faster time.

with a pair of vortex-antivortex caught at the pins, which is achieved in a faster time. In several cases we randomly picked, the initial conditions with artificial vortex pair always lead to the identical final state as would be expected for a thermodynamic equilibrium state, in a shorter time.

XII.3. Magnetic relaxation in a film with pins

After some trials and errors such as shown in Fig. 24, it emerged that the pinning force is not strong enough to hold the vortices against the attractive force between vortex and antivortex. Since it was found that the external magnetic field restricts the pin distance, an approach to magnetic relaxation using artificial vortices was devised to allow us to study longer pin separations. Figure 26 is a demonstration. To create an energy barrier big enough to hinder the vortices from moving, it was given the maximum distance possible in the periodic sample between pins (and vortices). That is, The pins at $(i_{p_1}, j_{p_1}) = (16, 16)$ and $(i_{p_2}, j_{p_2}) = (48, 48)$ has the longest separation from each other in the 64×64 grid of the sample in a *periodic array* of identical samples. The vortex and antivortex, located at (i_{p_1}, j_{p_1}) and (i_{p_2}, j_{p_2}) initially, move out of the pins and annihilate each other eventually.

We repeat this simulation with decreasing pin distance $d(p_1, p_2)$ from this maximum distance to the closest possible. In Fig. 27 the pins are located at $(i_{p_1}, j_{p_1}) = (16, 16), (17, 17), \dots, (28, 28)$ and $(i_{p_2}, j_{p_2}) = (48, 48), (47, 47), \dots, (36, 36)$, getting closer to each other by one node at each pin. At $t=0$, the artificial vortex-antivortex pair are located two nodes outward from the center of the pins.

The time until the vortices come out of the pins and annihilate is plotted in Fig. 28 below. Figure 28 is indicative of the fact that the vortices get harder to annihilate as they get farther. However, this is not a rigorous measure since the distance in which

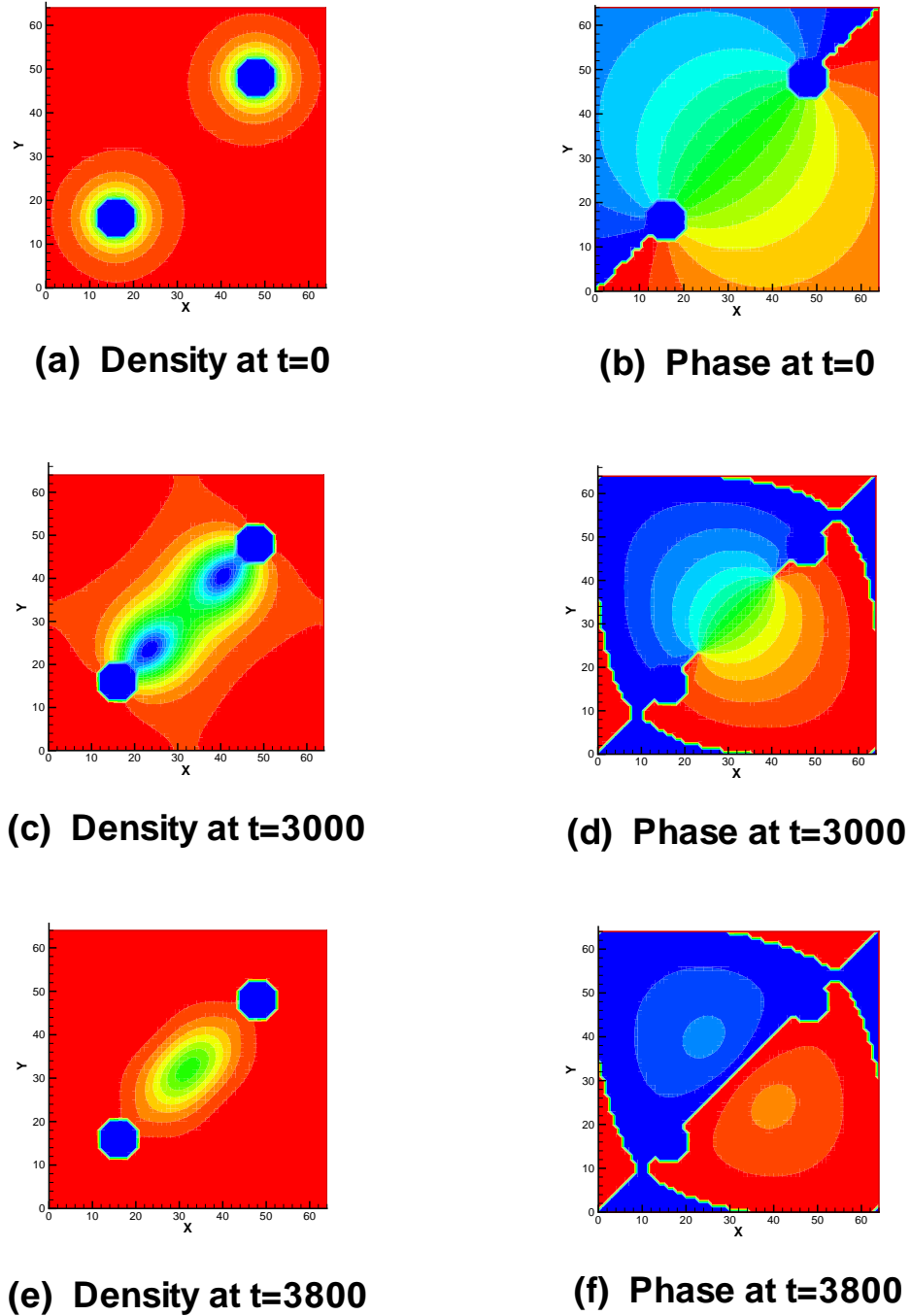


Fig. 26. Steady-states of a magnetic relaxation in a film with thickness $d_f = 0.1$. There are two antidots of an approximate diameter of 2ξ , centered at nodes $(16,16)$ and $(48,48)$ each. Here a pair of artificial vortex and antivortex attract each other under no external magnetic field. They eventually move out of the pins and annihilate each other.

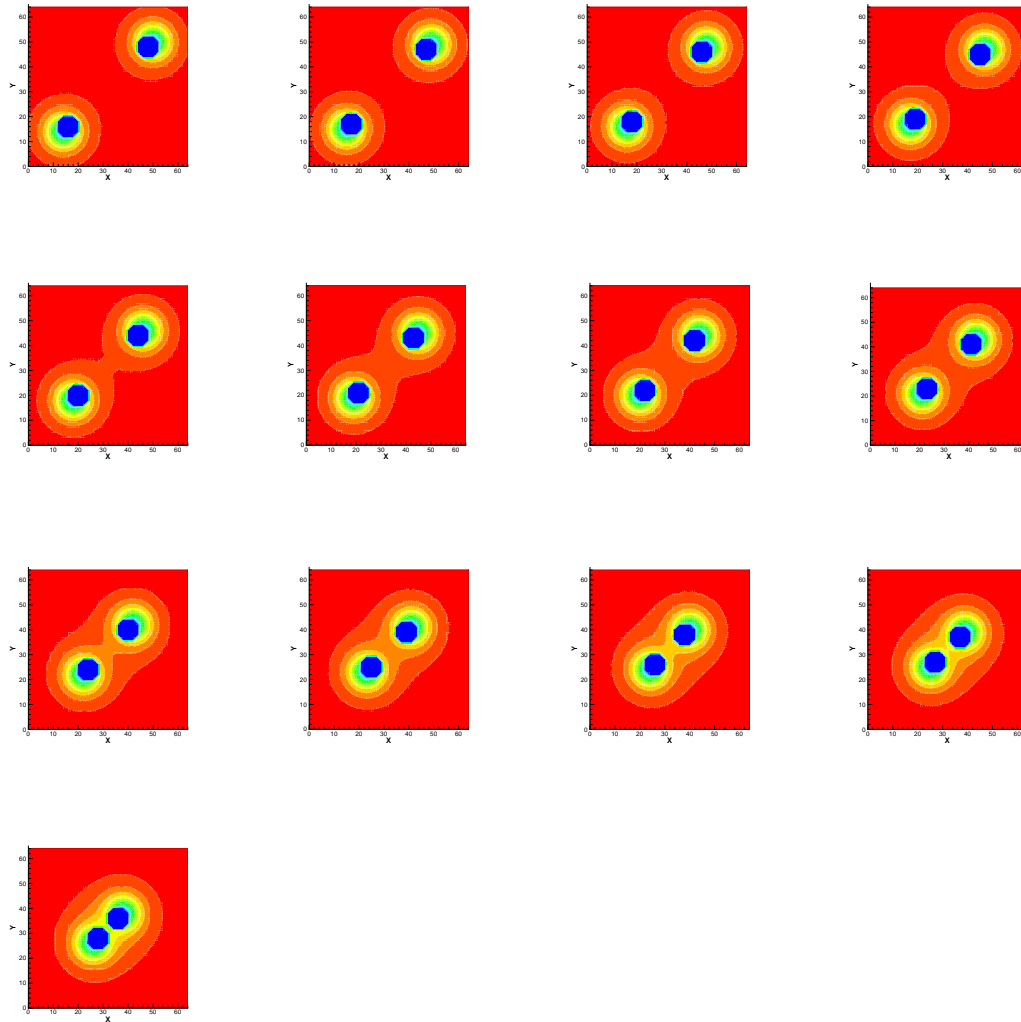


Fig. 27. The initial pin and vortex-antivortex arrangements of the simulation cases in which a pair of vortex and antivortex evolve with the external magnetic field removed. In the first case (shown in the upper left corner) the pins are located at $(i_{p_1}, j_{p_1}) = (16, 16)$ and $(i_{p_2}, j_{p_2}) = (48, 48)$. In the next case (to the right of the first sample), $(i_{p_1}, j_{p_1}) = (17, 17)$ and $(i_{p_2}, j_{p_2}) = (47, 47)$. In this way, the pins are put closer to each other by one node for the cases we consider one after another. In the last case, $(i_{p_1}, j_{p_1}) = (28, 28)$ and $(i_{p_2}, j_{p_2}) = (36, 36)$. At $t=0$, the artificial vortex-antivortex pair is located further outward by two nodes than the center of the pins. This is intended to prevent that any initial “overshoot” of the numerical simulation, instead of the actual attraction force, drives the vortices out of the pins.

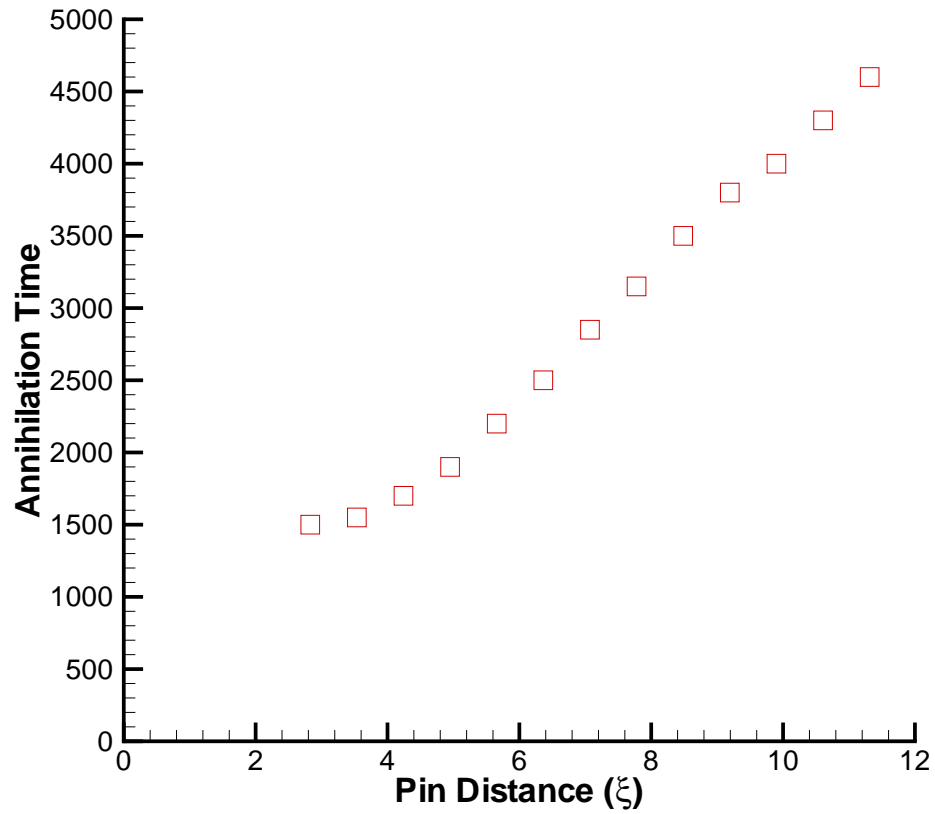


Fig. 28. Total time for the process where a pair of artificial vortex and antivortex attract, move out of the pins, and annihilate each other. It is a magnetic relaxation in a film with thickness $d_f = 0.1$ under no external dipole magnetic field. The abscissa is the distance in which the centers of the antidots of an approximate diameter of 2ξ are separated.

the vortices travel to annihilate each other is not a constant. We want to measure the time it takes for a vortex to escape from the pin. However, since the vortices are distorted and elongated while escaping from the pins (see, for example, Fig.26), it is hard to determine the position of the core. (If the pins are close enough to each other, the vortex and antivortex merge even before the complete escape, forming a “trough” of normal conducting region.) Thus, we pick an *ad hoc* density level $|\Psi|^2 = 0.3$ (Note that $|\Psi|^2 = 0$ in the core of a vortex) and measure the time this level of density contour “coming out” of the pin. This is illustrated in the Fig. 29 below.

In between the adjacent outputs at $t=1550$ and 1600 , a contour level 0.308114 comes out (small triangular contour in (d)). This time can give a time scale for the vortex core to come out of the pin. The plot for this “escape time” results from the the visual measurement of the density levels. Note this measurement cannot be too accurate since the data files are output from the code for $t = n\Delta t = 0, 100, 200, \dots$, not for each time step Δt , due to the limited storage. However, this can always be made more accurate if necessary. The resulting curve is given in the Fig. 30, which fits as $y = 1480 \ln(x) - 1806$ well. Note that $t_{esc} < 1800$ in this sample.

In Fig. 31 the density levels in a sample of the size $32\xi \times 32\xi$ are shown. Note this sample is 4 times bigger than the $16\xi \times 16\xi$ sample studied so far. At $t=16300$ the contour of the level 0.312317 is at the edge of the pin. At $t=16400$ this contour has come out of the pin, which can be seen as the little triangular contour near the upper right corner. The escape time is determined to be $t=15900$.

The pin distance is $16\sqrt{2}\xi = 22.6\xi$ in this sample. The curve-fit formula from the small sample produces far less $t_{esc} = 1480 \ln(22.6) - 1806 \simeq 2808.5$ than the escape time $t_{esc} = 15900$ determined above. This may imply the the attraction force between the vortex and the antivortex is weaker than the trend of the force that the curve-fit of the escape time in the small sample may suggests. Recalling Pearl’s theory,

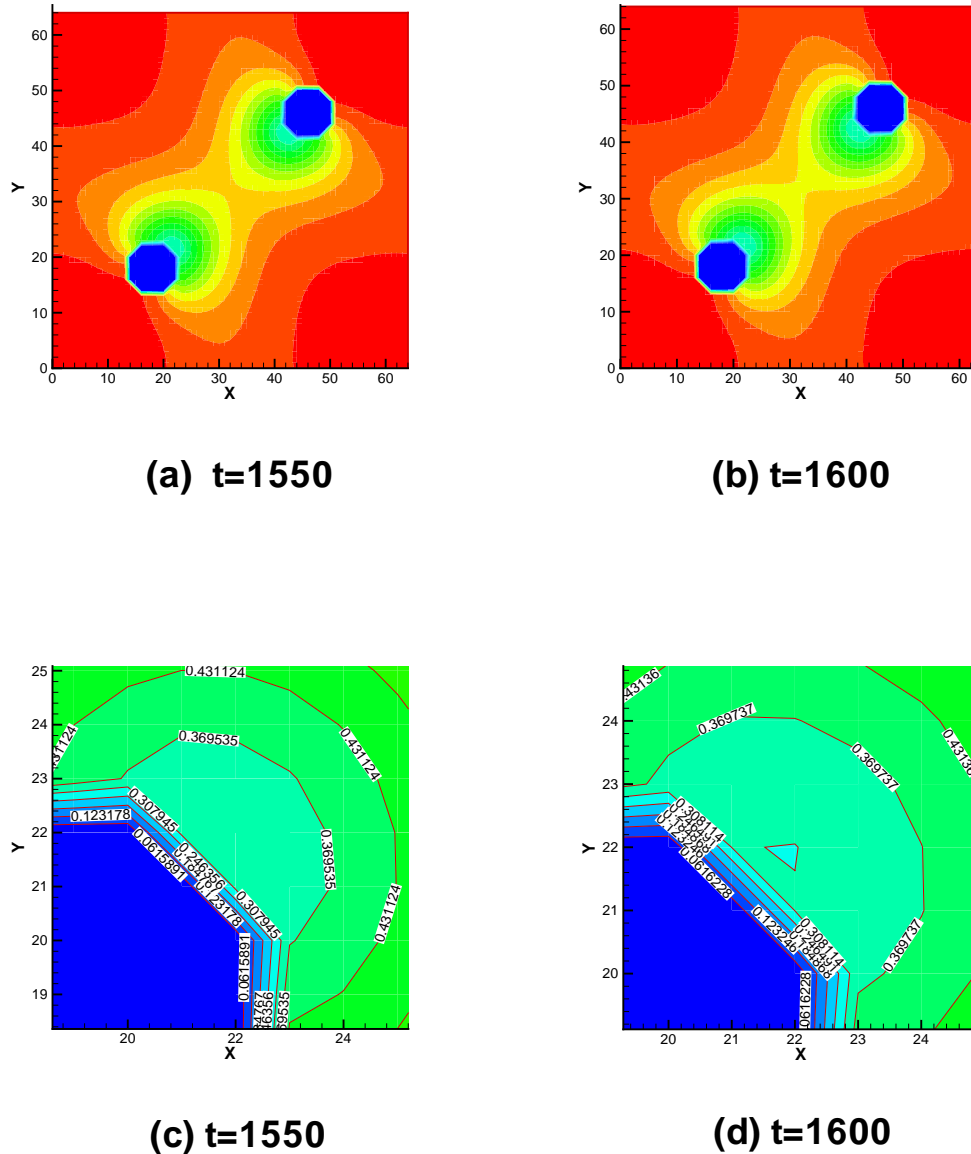


Fig. 29. Defining the “escape time” of the vortex-antivortex pair for the $16\xi \times 16\xi$ sample. (a) and (b) are the density plots produced in a given time interval. (c) and (d) give the enlarged view of the lower left pin. At $t=1550$ the $|\Psi|^2 = 0.3$ contour lies inside the pin surface. At $t=1600$ there is a small triangular contour of $|\Psi|^2 = 0.3$ having just emerged outside the pin. Thus $|\Psi|^2 = 0.3$ contour “escaped” from the pin between $t=1550$ and 1600 . We set $t=1550$ the “escape time”

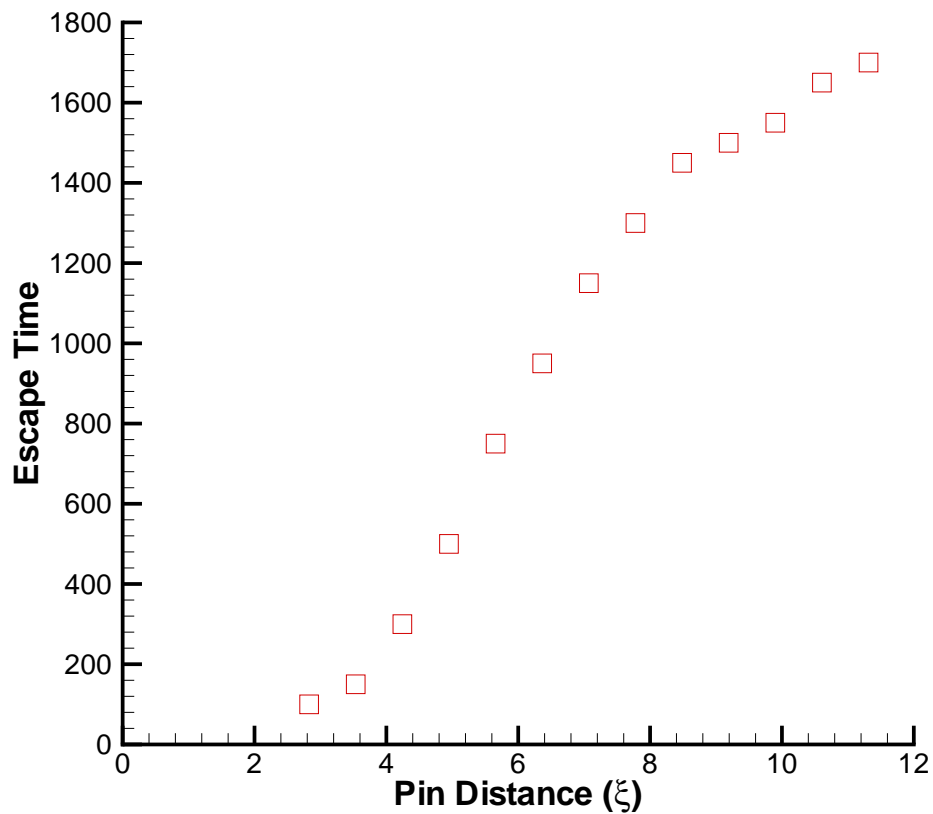


Fig. 30. Pseudo-time measure for how long a vortex would take to escape from the pins as defined in Fig. 29. It is chosen as the time the density contour of level 0.3 emerges from the pin. This “time” can give a time scale for the vortex core to emerge from the pin. The states are obtained in magnetic relaxations in a film with thickness $d_f = 0.1$ under no external dipole magnetic field. The abscissa is the distance in which the centers of the antidots of an approximate diameter of 2ξ are separated.

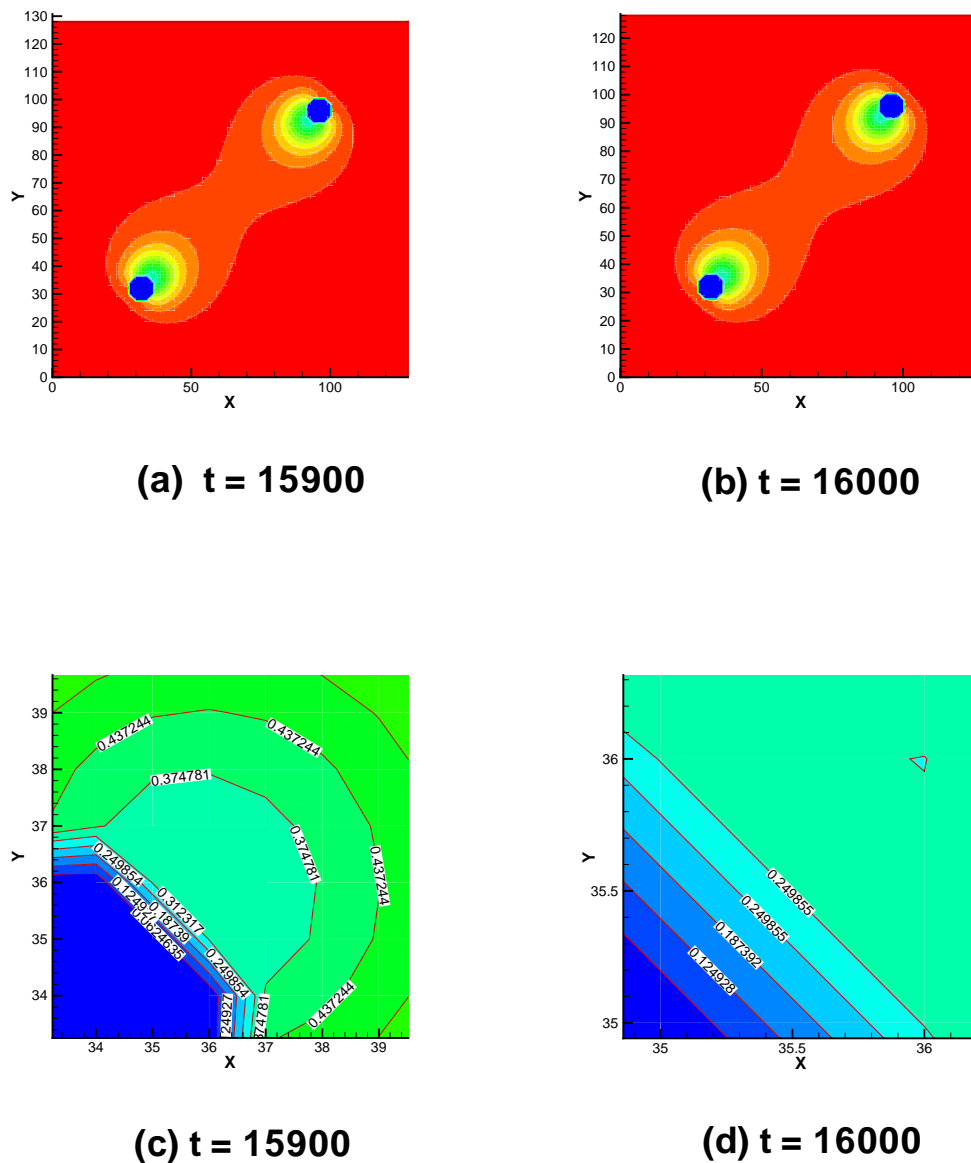


Fig. 31. Defining the “escape time” of the vortex-antivortex pair for the $32\xi \times 32\xi$ sample. (a) and (b) are the density plots produced in a given time interval. (c) and (d) give the enlarged view of the lower left pin. At $t=15900$ the $|\Psi|^2 = 0.3$ contour lies inside the pin surface. At $t=16000$ there is a small triangular contour of $|\Psi|^2 = 0.3$ having just emerged outside the pin. Thus $|\Psi|^2 = 0.3$ contour “escaped” from the pin between $t=15900$ and 16000 . We set $t=15900$ the “escape time”

the attractive force between a vortex and an antivortex has a rather slow variation depending on $\frac{1}{r}$ for their separation $r \ll \lambda_{eff}$. For the small sample the maximum pin distance possible is $11.4\xi = 0.285\lambda_{eff}$, which is still small in comparison with $\lambda_{eff} = 40\xi$. When the pin centers are 2.8ξ apart from each other, the attraction force is very strong, leading to a quick annihilation. This dominance of the attraction force over the constant pinning force continues due to the slow decrease of the attraction force. Since the pin distance 22.6ξ is not so small when compared with the effective penetration depth λ_{eff} , we expect the change in the variation of the force toward the other asymptotic behavior of $\frac{1}{r^2}$. This is reflected in the fact that we have $t_{esc} > 12600$ for the pin distance of 17ξ . About 50% increase from the maximum pin distance 11.4ξ of the small sample leads to over 700% increase in the escape time. So the attraction force should decrease faster than $\frac{1}{r}$ -dependence in the range of pin distances larger than 11.4ξ .

In the small sample, the vortices actually escaped from the pins soon after reaching the escape time. Thus the estimated escape time is close to the real escape time. However, in the bigger sample, the vortices have reached steady-state without appreciable movement from the pins after $t \sim 25000$. So the estimated escape time $t=15900$ for the larger sample is not really an escape time, since the vortices do not escape. Nevertheless they are still useful for comparison with the small sample. Figure 32 shows virtually no change between $t=25200$ and $t=42400$. Even after the escape time $t=15900$ there have been only minor shifts in the contours of the higher density level. The $|\Psi|^2 = 0.3$ core shows little movement.

The vortex and antivortex are attempting to come out of the pins and annihilate each other, but they have eventually failed to come out. So the pin distance 22.6ξ must be very close to the critical distance to pin the vortex and the antivortex at the pinning spots permanently. This simulation has taken 26 days in wall clock time

to reach $t=42400$. It is not feasible to do simulation with this size of sample in the current facility, but this sample could be a starting point of another long, extensive study. It takes about 35 hours in wall clock time to reach $t=25200$ in the small sample in our current facility. Comparison with 14 days to reach the same t in the large sample shows the difficulty we are facing.

If the vortex-antivortex pair can be pinned by the pins without the creating dipole field, then they could represent 1 in non-volatile data storage. Since the last studied case looks close to pinning, we can use it as an “optimum” case for the data storage. Then the density is of vortices will be $(1 \text{ vortex-antivortex pair})/(32\xi)^2 \sim 3.8 \times 10^{14}$ vortex-antivortex-pairs/ $m^2 \cong 4.7GB/cm^2$, assuming $\xi = 16 \text{ \AA}$ for high temperature cuprate superconductors.

CHAPTER XIII

CONCLUSIONS

In this dissertation, the numerical simulations on the steady-state vortex configurations in type-II superconductors have been performed. We have considered a mesoscopic square cylinder with free boundary conditions in part I and a thin square film with periodic boundary conditions in part II. Part I presents an efficient numerical scheme to find the equilibrium vortex configuration inside the superconductor under a given external magnetic field. Part II presents the systematic numerical experiment to find an optimal vortex pinning configuration. Each part is summarized in the following sections.

XIII.1. Summary and conclusion to Part I

A numerical scheme to study the mixed states in a mesoscopic type-II superconducting square cylinder in a longitudinal external magnetic field H has been developed. It is based on solving a set of simplified time-dependent Ginzburg-Landau equations.

We have first applied this scheme to the case of field penetration into a zero-field cooled sample. Case studies for various values of the external magnetic field were presented. Contour plots of the Cooper pair density, and the induced magnetic field inside the sample, display the magnetic vortex solution first discovered by Abrikosov, but in a small sample the vortex arrangement is not simply triangular.

Giant vortices and anti-vortices are not found in this study, unlike previous studies of type-I mesoscopic thin films. (But at sufficiently high magnetic field we still expect the system to favor a single giant vortex at the center as it goes into a surface superconducting state, but only if the sample is not too small.)

Since we start the solution with a uniformly superconducting initial condition,

and the sample has perfect square symmetry, both the number of vortices and their steady-state configurations are governed by the square sample geometry. Changes in the configuration and the number of vortices occur as H is varied through first-order configurational phase transitions, similar to those found earlier, but different in detail. This phase transition characteristic is confirmed by the contour plots, and jumps in the values of the induced magnetic field B at certain discrete H values.

A time sequence shows that the system passes through intermediate configurations, and remains in some of them for a long time. Eventually the system settles down to the steady-state configuration, which corresponds to the lowest-Gibbs-energy configuration consistent with the symmetry constraints to the vortex number and configuration.

True equilibrium states would appear in actual samples when there are symmetry-breaking surface defects forming vortex-nucleation centers, or when thermal fluctuations are sufficiently strong to move the system out of metastable states, but not too strong to melt the vortex lattice. We could have determined these true equilibrium states by adding additional terms in the equations to simulate thermal fluctuations, but here we have devised a different approach which we believe is more efficient. We introduce a way to generate analytic initial states of prescribed numbers of vortices, but allow their positions to be random. They evolve to steady-state vortex arrangements of all possible vortex numbers near the equilibrium number, from which we can compare total Gibbs energy to determine the equilibrium vortex number and configuration. In this way, we avoid the problem of surface and bulk energy barriers, which can trap the system in non-equilibrium vortex numbers and configurations — an undesirable situation which usually happens if one chooses the initial state randomly without controlling the vorticity quantum number L .

XIII.2. Conclusion to Part II

1. A numerical study of the magnetization process in a thin type-II superconducting film has been performed. The film is subject to a non-uniform magnetic field created by a dipole above the film. The dipole axis passes through the center of the film in the normal direction to the film plane. The magnetic flux Φ^+ sent by the dipole through the film is estimated by numerically integrating only the region where $H_z > 0$.

2. For a film with constant thickness and with no pin, it has been found that the film carries two pairs of vortex-antivortex in the steady state in the range of $2.15 < \Phi^+ < 2.90$. The 3-pair-to-2-pair transitions, in which a pair of vortex-antivortex annihilates, have been observed. For $\Phi^+ \leq 2.15$ no vortex-antivortex pair has been created in the film.

3. Two antidots (holes) have been used to create a perturbation in the film, and vortex-antivortex pair has been created for lower magnetic fluxes down to $\Phi^+ = 1.3$.

4. It is observed that the magnetic field is controlling the situation, deciding the optimal locations of vortex and antivortex. Therefore the pin locations are necessarily fixed by the magnetic field, too. For the present study this restricts the numerical experiment with variable pin locations, so we have divided the study into two separate stages, (1) the magnetic penetration with antidots discussed so far, and (2) the magnetic relaxation of a vortex-antivortex pair with the external magnetic field removed (turned off), which will be discussed later.

4. Aligning the dipole axis in the direction parallel to the film surface may remedy this restriction, giving an extra degree of freedom to control the curvature of magnetic field lines by changing the location of the magnetic charges. Reducing the curvature of the field lines penetrating the film will create more widely separated vortex-antivortex pair.

5. In the sample of size $16\xi \times 16\xi$, the attraction force between the vortex and antivortex always dominates over the pinning force, so that they eventually come out of pins, move toward each other, and annihilate each other.

6. The annihilation rate, measured with time taken for the annihilation, is reduced noticeably as the distance between the vortex and antivortex increases. An increase in pinning force is also observed that as the pins get bigger. Therefore, it is concluded that we will have vortex-antivortex pair pinned as we increase the sizes of sample and pins.

6. In order to pursue the merit of engineering (to create high-density data storage), the use a new kind of pins which has stronger pinning force such as paramagnetic dots is recommended, so that the increase in the distance between the vortex-antivortex pair (hence the increase in sample size) can be minimized.

7. A simulation of the magnetic simulation in the sample of size $32\xi \times 32\xi$ suggests we are likely to achieve pinning of the vortex-antivortex pair with the sample size around this. Using this sample as a template, the maximum density of pinned vortices achievable is calculated to be about 3.8×10^{14} vortex-antivortex-pairs / m^2 , or about $4.7GB/cm^2$.

REFERENCES

- [1] F. London, *Superfluids* (John Wiley & Sons, Inc., New York, 1950).
- [2] G. Bednorz and K. A. Müller, *Z. Phys. B* **64**, 189 (1986).
- [3] S. Kim, C.-R. Hu, and M. J. Andrews, *Phys. Rev. B*, **69**, 094521 (2004).
- [4] F. London and H. London, *Physica* **2** 341 (1935); F. London, *Act. Sci. et Ind.*, No. 458 (1937), Paris.
- [5] J. I. Gersten and F. W. Smith, *The Physics and Chemistry of Materials* (John Wiley & Sons, Inc., New York, 2001).
- [6] W. Meissner and R. Ochsenfeld, *Naturwissenschaften*, **21**, 787 (1933).
- [7] V. L. Ginzburg and L. D. Landau, *Zh. Eksperim. i. Teor. Fiz.* **20** 1064 (1950).
- [8] J. Bardeen, L. N. Cooper, and J. R. Schrieffer, *Phys. Rev.*, **108** 1175 (1957).
- [9] A. A. Abrikosov, *Sov. Phys. JETP* **5** 1174 (1957) [*Zh. Eksp. Teor. Fiz.* **32** 1442 (1957)].
- [10] The Nobel Prize in Physics 2003,
<http://nobelprize.org/physics/laureates/2003/index.html>.
- [11] The Nobel Prize in Physics 2003 - information for the public,
<http://nobelprize.org/physics/laureates/2003/public.html>.
- [12] D. Saint-James and P. G. Gennes, *Physics Letters*, **7** 306 (1963).
- [13] D. Saint-James, *Physics Letters*, **15** 13 (1965).
- [14] H. J. Fink and L. J. Barnes, *Phys. Rev. Lett.*, **15** 792 (1965).

- [15] L. J. Barnes and H. J. Fink, *Phys. Rev.*, **149** 186 (1966).
- [16] H. J. Fink and L. J. Barnes, *Phys. Rev.*, **151** 219 (1966).
- [17] H. J. Fink and L. J. Barnes, *Phys. Rev.*, **168** 399 (1968).
- [18] F. de la Cruz, H. J. Fink and J. Luzuriaga, *Phys. Rev. B*, **20** 1947 (1979).
- [19] B. J. Baelus and F. M. Peeters, *Phys. Rev. B* **65** 104515, (2002).
- [20] E. M. Lifshitz and L. P. Pitaevskii, *Statistical Physics*, Part2 (Reed Educational and Professional Publishing Ltd., Oxford, UK 1980).
- [21] L. D. Landau and E. M. Lifshitz, *Quantum Mechanics* (A. Wheaton & Co. Ltd., Exeter, UK 1977).
- [22] L. D. Landau and E. M. Lifshitz, *Fluid Mechanics* (Pergamon Books Ltd., Oxford, UK 1989).
- [23] A. A. Abrikosov, L. P. Gor'kov and I. Dzyaloshinskii, *Quantum Field Theoretical Methods in Statistical Physics* (Pergamon Press Ltd., Oxford, UK 1965).
- [24] P. G. de Gennes, *Superconductivity in Metals and Alloys* (W. A. Benjamin Inc., New York, 1966. Reprinted by Addison-Wesley, Reading, MA 1989).
- [25] M. Tinkham, *Introduction to Superconductivity* (McGraw-Hill Inc., New York, 1996).
- [26] L. N. Cooper, *Phys. Rev.*, **104** 1189 (1956).
- [27] H. B. Callen, *Thermodynamics and An Introduction to Thermostatistics* (John Wiley & Sons, Inc., New York, 1985).

- [28] L. D. Landau and E. M. Lifshitz, *Statistical Physics*, Part1 (Reed Educational and Professional Publishing Ltd., Oxford, UK 1980).
- [29] D. Saint-James, E. J. Thomas, and G. Sarma, *Type II Superconductivity* (Pergamon Press Ltd., Oxford, UK 1969).
- [30] J. Smit, *Introduction to Quantum Fields on a Lattice* (Cambridge University Press, Cambridge, UK 2002).
- [31] W. Ludwig and C. Falter, *Symmetries in Physics* (Springer-Verlag, Berlin, Germany 1996).
- [32] V. Icke, *The Force of Symmetry* (Cambridge University Press, Cambridge, UK 1995).
- [33] K. J. M. Moriarty, E. Myers and C. Rebbi, *Computer Physics Communications* **54** 273 (1989).
- [34] L. P. Gor'kov, *Sov. Phys. JETP* **9** 1364 (1959) [*Zh. Eksp. Teor. Fiz.* **36** 1918 (1959)].
- [35] L. P. Gor'kov, *Sov. Phys. JETP* **10** 998 (1960) [*Zh. Eksp. Teor. Fiz.* **37** 1407 (1959)].
- [36] A. Schmid, *Phys. kondens. Materie* **5** 302 (1966).
- [37] L. P. Gor'kov and G. M. Eliashberg, *Sov. Phys. JETP* **27** 328 (1968) [*Zh. Eksp. Teor. Fiz.* **54** 612 (1968)].
- [38] V. A. Schweigert and F. M. Peeters, *Phys. Rev. B* **57** 13817 (1998).
- [39] V. A. Schweigert, F. M. Peeters, and P. Singha Deo, *Phys. Rev. Lett.* **81** 2783 (1998).

- [40] P. Singha Deo, V. A. Schweigert, F. M. Peeters, and A. K. Geim, *Phys. Rev. Lett.* **79** 4653 (1997).
- [41] J. Bonca and V. V. Kabanov, *Phys. Rev. B* **65** 012509 (2001).
- [42] V. R. Misko, V. M. Fomin, J. T. Devreese, and V. V. Moshchalkov, *Physica C* **369**, 361 (2002).
- [43] K. Geim, S. V. Dubonos, J. J. Palacios, I. V. Grigorieva, M. Henini, and J. J. Schermer, *Phys. Rev. Lett.* **85**, 1528 (2000).
- [44] V. R. Misko, V. M. Fomin, J. T. Devreese, and V. V. Moshchalkov, *Phys. Rev. Lett.* **90**, 147003 (2003).
- [45] G. W. Crabtree, D. G. Gunter, H. G., Kaper, A. E. Koshelev, G. K. Leaf, and V. M. Vinokur, *Phys. Rev. B* **61**, 1446 (2000).
- [46] H. G. Kaper and M. K. Kwong, *J. Comp. Phys.* **119** 120 (1995).
- [47] W. H. Press, B. P. Flannery, S. A. Teukolsky, and W. T. Vetterling, *Numerical Recipes* (Cambridge University Press, New York 1986).
- [48] M. M. Doria, J. E. Gubernatis, D. Rainer, *Phys. Rev. B* **41** 6335 (1990).
- [49] Q. Du, M. D. Gunzburger, J. S. Peterson, *SIAM Review* **34** 54 (1992).
- [50] R. S. Varga, *Matrix Iterative Analysis* (Springer-Verlag, Berlin, 2000).
- [51] E. Coskun and M. K. Kwong, *Nonlinearity* **10** 579 (1997).
- [52] S. L. Adler and T. Piran, *Rev. Mod. Phys.* **56** 1 (1984).
- [53] Z. D. Wang and C. R. Hu, *Phys. Rev. B* **44** 11918 (1991).

- [54] E. Coskun, *Numerical Analysis of Ginzburg-Landau Models for Superconductivity*, Ph.D. dissertation, Department of Mathematical Sciences, Northern Illinois University, Dekalb (1994).
- [55] R. D. Richtmyer and K. W. Morton, *Difference Methods for Initial-Value Problems* (John Wiley & Sons, Inc., New York, 1967).
- [56] G. Strang, *Linear Algebra and its Applications* (Harcourt Brace Jovanovich, Inc., Orlando, FL 1988).
- [57] J. C. Tannehill, D. A. Anderson, and R. H. Pletcher, *Computational Fluid Mechanics and Heat Transfer* (Taylor & Francis, Washington, D.C., 1997).
- [58] R. Kato, Y. Enomoto, S. Maekawa, Phys. Rev. B **47** 8016 (1993).
- [59] F. M. Peeters, personal communication, Department Natuurkunde, Universiteit Antwerpen (UIA), B-2610 Antwerpen, Belgium.
- [60] C.-R. Hu and R. S. Thompson, Phys. Rev. B **6** 110 (1972).
- [61] J. R. Clem, J. Low Temp. Phys. **18** 427 (1975).
- [62] M. J. Van Bael, J. Bekaert, K. Temst, L. Van Look, V. V. Moshchalkov, Y. Bruynseraede, G. D. Howells, A. N. Grigorenko, S. J. Bending, and G. Borghs, Phys. Rev. Lett. **86** 155, (2000).
- [63] Y. Nozaki, Y. Otani, K. Runge, H. Miyajima, B. Pannetier, J. P. Nozières and G. Fillion, J. Appl. Phys. **79** (11) 8571, (1996).
- [64] M. V. Milošević and F. M. Peeters, J. Low Temp. Phys. **130** 311, (2003).
- [65] D. J. Priour, Jr. and H. A. Fertig, Phys. Rev. Lett. **93** 057003 (2004).

- [66] R. Kato, Y. Enomoto, S. Maekawa, *Physica C* **227** 387 (1994).
- [67] E. Coskun, *Applied Mathematics and Computation*, **106** 31, (1999).
- [68] G. Mkrtchyan and V. Shmidt, *Sov. Phys. JETP* **34** 195, (1972).
- [69] I. Khalfin and B. Shapiro, *Physica C* **207** 359, (1993).
- [70] A. Budzin, *Phys. Rev. B* **47** 11416, (1993).
- [71] N. Takezawa and K. Fukushima, *Physica C* **290** 31, (1997).
- [72] D. J. Priour, Jr. and H. A. Fertig, *Phys. Rev. B* **67** 054504 (2003).
- [73] L. Civale, A. Marwick, T. Worthington, M. Kirk, J. Thompson, L. Krusin-Elbaum, Y. Sun, J. Clem, and F. Holtzberg, *Phys. Rev. Lett.* **67** 648, (1991).
- [74] J. Pearl, *Appl. Phys. Lett.* **5** 65, (1964).
- [75] M. Machida and H. Kaburaki, *Phys. Rev. B* **50** 1286, (1994).
- [76] M. Abramowitz and I. Stegun, *Handbook of Mathematical Functions* (Dover Publications, Inc., New York, 1964).
- [77] M. Doria, J. Gubernatis, and D. Rainer, *Phys. Rev. B* **39** 9573, (1989).
- [78] J. D. Jackson, *Classical Electrodynamics* (John Wiley & Sons, Inc., New York, 1975).
- [79] P. J. Roache, *Elliptic Marching Methods and Domain Decomposition* (CRC Press, Inc., Boca Raton, FL 1995).
- [80] E. O. Brigham, *The Fast Fourier Transform and its Applications* (Prentice-Hall, Inc., Upper Saddle River, NJ 1988).

- [81] W. H. Press, S. A. Teukolsky, W. T. Vetterling, and B. P. Flannery, *Numerical Recipes in Fortran 90* (Cambridge University Press, New York, 1996).
- [82] OpenMP programming tutorial, <http://www.openmp.org>
- [83] A. Grama, A. Gupta, G. Karypis, and V. Kumar, *Introduction to Parallel Computing* (Addison-Wesley, New York 2003).
- [84] S. J. Chapman, *Z. angew. Math. Phys.* **47** 410 (1996).
- [85] Q. Du, M. D. Gunzburger, J. S. Peterson, *Phys. Rev. B* **46** 9027 (1992).

APPENDIX A

VORTEX CONFIGURATION IN A TWO-DIMENSIONAL PERIODIC DOMAIN

Figure 33 shows an arbitrary sample spanned by the lattice vectors \mathbf{t}_1 and \mathbf{t}_2 . For simplicity \mathbf{t}_1 is aligned parallel to the x axis.

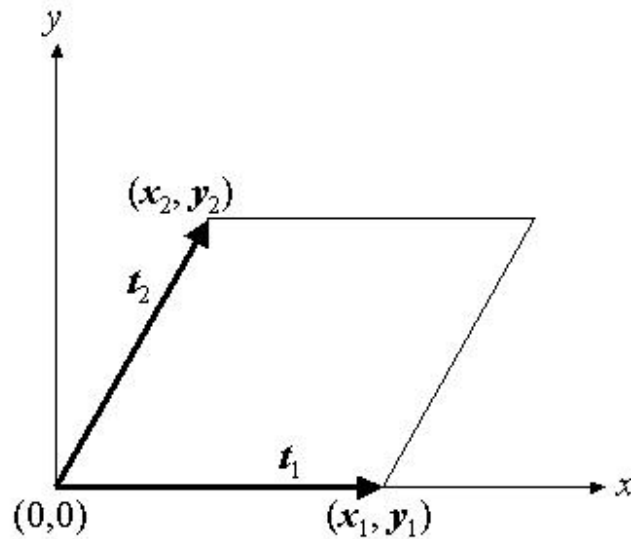


Fig. 33. A periodic sample spanned by the lattice vectors \mathbf{t}_1 and \mathbf{t}_2 .

The periodic boundary conditions discussed in chapter 10 are written as ¹

$$\mathbf{A}(\mathbf{x} + \mathbf{t}_i) = \mathbf{A}(\mathbf{x}) + \nabla g_i, \quad i = 1, 2, \quad (\text{A.1})$$

¹Here the variables are nondimensionalized as in part I: $x' = \frac{x}{\lambda}$, $\mathbf{H}' = \frac{\mathbf{H}}{\sqrt{2}H_c}$, $\mathbf{h}' = \frac{\mathbf{h}}{\sqrt{2}H_c}$, $\mathbf{j}' = \frac{2\sqrt{2}\pi\lambda}{cH_c}\mathbf{j}$, $\mathbf{A}' = \frac{\mathbf{A}}{\sqrt{2}H_c\lambda}$, $\Psi' = \frac{\Psi}{\Psi_0}$. Primes are omitted for convenience.

$$\Psi(\mathbf{x} + \mathbf{t}_i) = \Psi(\mathbf{x}) e^{i\kappa g_i} \quad i = 1, 2, \quad (\text{A.2})$$

where $g_k(\mathbf{x}; \mathbf{t}_i)$, $i = 1, 2$, is given by [49]

$$g_k = -\frac{1}{2} (\mathbf{t}_i \times \bar{B} \hat{\mathbf{e}}_z) \cdot \mathbf{x}, \quad (\text{A.3})$$

Along the boundaries of the cell depicted in Fig. 33, the periodic boundary conditions become

$$\mathbf{A}(x + x_2, y_2) = \mathbf{A}(x, 0) + \frac{1}{2} \bar{B} (x_2 \hat{\mathbf{e}}_y - y_2 \hat{\mathbf{e}}_x) \quad \text{for } 0 < x < x_1, \quad (\text{A.4})$$

$$\mathbf{A}\left(x_1 + \frac{x_2}{y_2} y, y\right) = \mathbf{A}\left(\frac{x_2}{y_2} y, y\right) + \frac{1}{2} \bar{B} x_1 \hat{\mathbf{e}}_y \quad \text{for } 0 < y < y_2, \quad (\text{A.5})$$

$$\Psi(x + x_2, y_2) = \Psi(x, 0) \exp\left(-i \frac{1}{2} \kappa \bar{B} y_2 x\right) \quad \text{for } 0 < x < x_1, \quad (\text{A.6})$$

$$\Psi\left(x_1 + \frac{x_2}{y_2} y, y\right) = \Psi\left(\frac{x_2}{y_2} y, y\right) \exp\left(i \frac{1}{2} \kappa \bar{B} x_1 y\right) \quad \text{for } 0 < y < y_2, \quad (\text{A.7})$$

where the average magnetic field \bar{B} , the number of flux quanta n and the lattice cell area $|\Omega| = |\mathbf{t}_1 \times \mathbf{t}_2|$ are related by

$$|\Omega| = \frac{2\pi n}{\kappa \bar{B}}. \quad (\text{A.8})$$

We apply the periodic boundary conditions given by Du et al. [49] to a two-dimensional, periodic system of square cells (i.e. $x_2 = 0, y_1 = 0$) carrying n flux quanta. An example for $n = 9$ is given below.

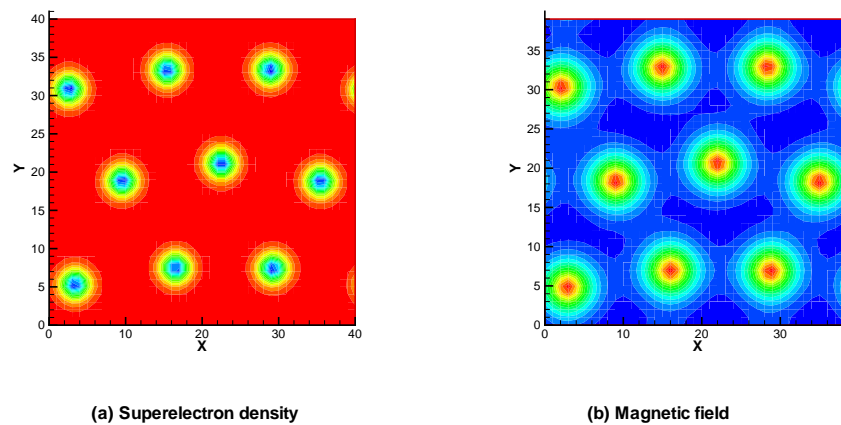


Fig. 34. Triangular-ish lattice of vortices in a square superconducting cylinder with periodic boundary conditions carrying 9 flux quanta.

APPENDIX B

VORTEX PINNING IN A FILM WITH VARIABLE THICKNESS

Chapman [84] has derived a mathematical model for superconductivity in thin films with variable thickness. Through an averaging process across the thickness, he has derived a Ginzburg-Landau model where the variations in thickness appear as spatially varying coefficients in the differential equations. This model has been used by several authors to study the characteristics of superconducting thin-films under a uniform magnetic field. It has been found that even type-I bulk superconductors behave as type-II when their thickness is made sufficiently thin by an asymptotic analysis and numerical simulations. [84, 85] Numerical simulations show that the thinner spots in the variable thickness film attract vortices. [84, 67]

Here is an example of pinning by variable thickness using Chapman's model. This work has been done using the relaxations equations with free boundary conditions from Part I. In the same nondimensionalized variables, an external magnetic field $H = 1$ was applied to a superconductor of the size 15×15 and thickness $d_f = 1$. The Ginzburg-Landau parameter $\kappa = 4$. On the 60×60 grid, the pin thickness $d_{pin} = 0.001$ are assigned at the nodes (i, j) where $i, j = 10, 20, 30, 40, 50$ along each x, y direction. Thus we have 25 pins. The four neighborhood points adjacent the pin, $(i + 1, j)$, $(i - 1, j)$, $(i, j + 1)$, and $(i, j - 1)$, are given $d_{neighbor} = 0.005$. The spatial increments $h_x = h_y = 0.25$, and the time step $\Delta t = 0.05$. In the figure 35 the system is full of vortices at $t=20000$. Then the magnetic field is turned off. At $t=50000$ the system is in the steady state, with vortices pinned at the thin sites in the film. Note that there are some vortices trapped between these pinning sites.

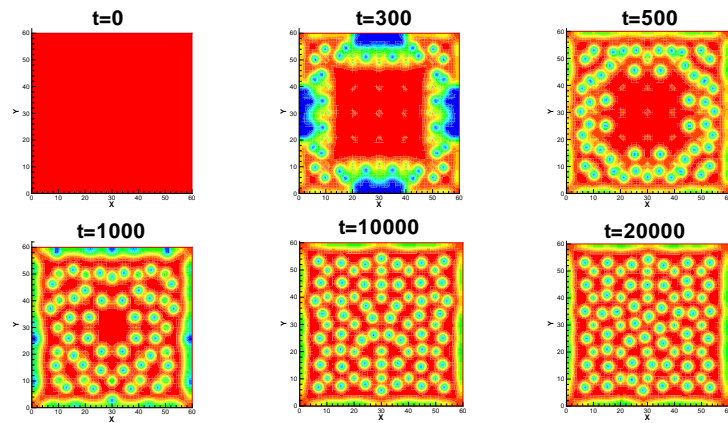
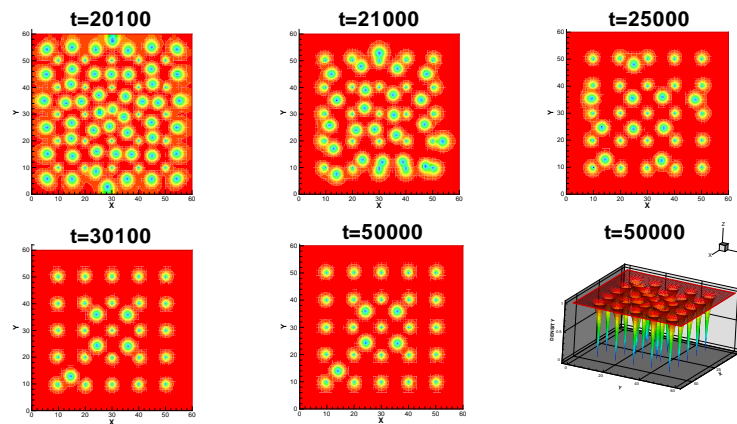
(a) Magnetic penetration process ($H = 1$)(b) Magnetic relaxation process ($H = 0$)

Fig. 35. Vortex pinning and flux trapping in a film of variable thickness by a regular array of thin regions (pins). $H = 1$; $\kappa = 4$; film thickness = 1; pin thickness = 0.001; and pin neighbor thickness = 0.005.

APPENDIX C

FLOW OF VORTICES UNDER A LINEARLY VARYING MAGNETIC FIELD

Figure 36 presents a simulation of the movement of vortices across the sample driven by a linearly varying magnetic field. This work has been done using the relaxations equations with free boundary conditions (with the linearly varying magnetic field) from Part I. The external magnetic field is $H_0 = 1.2$ on Ω_L while zero on Ω_R . Along the boundaries on top and bottom, the external magnetic field varies as $H(x) = H_0(1 - x/L)$. The spatial increments $h_x = h_y = 0.25$ on 80×40 grid points, and the time step $\Delta t = 0.05$.

From a physical point of view, this corresponds to a situation that a superconductor is located near the medium creating strong magnetic field such as power sources. The magnetic field from the medium is assumed to decrease linearly. The simulation shows that the vortices will be created and move away from the source of the external magnetic field. [54]

Due to the Lorentz force density $\mathbf{F} = \mathbf{j} \times \frac{\mathbf{B}}{c}$ between the current \mathbf{j} and the magnetic induction \mathbf{B} , each flux line (vortex) is subject to the force density

$$\mathbf{f} = \mathbf{j} \times \frac{\Phi_0}{c}, \quad (\text{C.1})$$

where \mathbf{j} is the total current density in the superconductor and Φ_0 the flux density (vector) threading through it. When there are no pins to hold the flux lines, they move transverse to the current. Moving with velocity \mathbf{v} , they induce an electric field

$$\mathbf{E} = \mathbf{B} \times \frac{\mathbf{v}}{c} \quad (\text{C.2})$$

Since \mathbf{E} is in the parallel direction to \mathbf{j} , it impedes the current. The resulting power dissipation can lead to heating, and loss of superconductivity, eventually. [25]

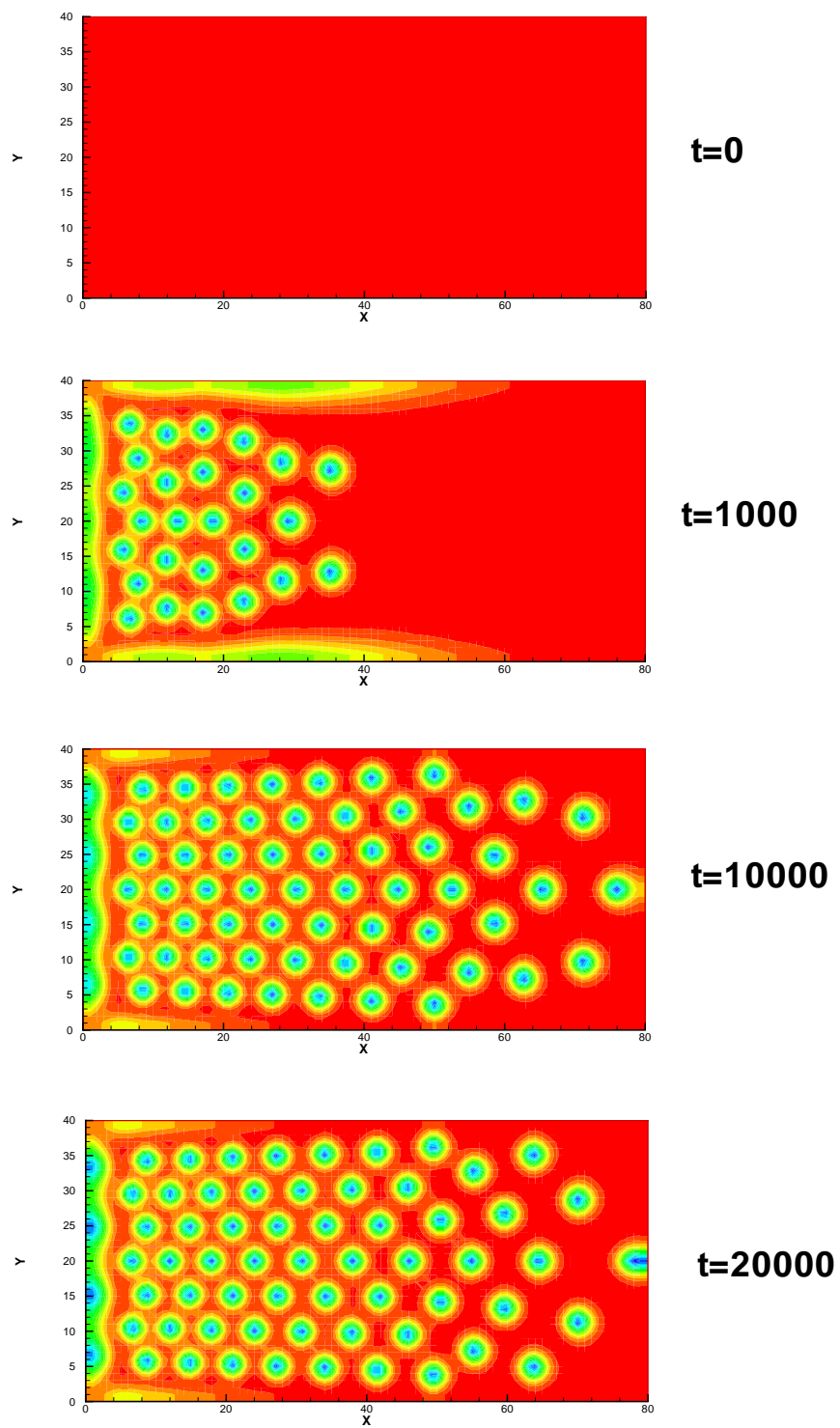


Fig. 36. Flow of vortices driven by the linearly varying magnetic field.

VITA

Sangbum Kim was born in Seoul, Korea in February 16, 1968. Sangbum graduated from the Pohang University of Science and Technology (POSTECH) with B.S. in mechanical engineering in 1991. He earned the M.S. in mechanical engineering from POSTECH in 1993.

Sangbum earned M.S.E. degree in mechanical engineering at the University of Texas at Austin in 2000. In 2004 he graduated from the Texas A&M University with the Ph.D. in the materials science and engineering.

Sangbum's permanent address:

17-616 TAESUNG BLDG. #BOA
BULGWANG-DONG, EUNPYONG-GU
SEOUL, 122-041
KOREA.